Title

Electrocorticography on the Micron Scale: Single Units and Enhanced Neural State Estimation

Author

Hermiz, John

Publication Date

2018

UNIVERSITY OF CALIFORNIA SAN DIEGO

Electrocorticography on the Micron Scale: Single Units and Enhanced Neural State Estimation

A Dissertation submitted in partial satisfaction
of the requirements of the degree
Doctor of Philosophy

in

Electrical Engineering (Medical Devices and Systems)

by

John Hermiz

Committee in charge:

Professor Vikash Gilja, Chair
Professor Shadi A. Dayeh
Professor Anna Devor
Professor Eric Halgren
Professor Piya Pal

2018

The Dissertation of John Hermiz is approved, and it is acceptable in quality and form for publication on microfilm and electronically:

Chair

University of California San Diego

2018

DEDICATION

This dissertation is dedicated to all my educators from Head Start to Graduate school especially the following individuals:

Mrs. Tienda, 5th grade

Ms. Venier, 6th grade Science

Mr. Yowchuang, High school Track & Field, Cross Country Coach

Mr. Cierpial, 12th grade English

The late Mr. Daida, Freshman year, Introduction to Engineering

EPIGRAPH

“There’s Plenty of Room at the Bottom”

-Richard Feynman

TABLE OF CONTENTS

LIST OF FIGURES

LIST OF TABLES

ACKNOWLEDGEMENTS

I would like to acknowledge Dr. Vikash Gilja for his support, guidance, and trust. Out of the countless PhD programs that I applied to, Vikash was the only one who gave me the opportunity to pursue a doctoral degree – sincerely, thank you. Thank you for instilling confidence in me as an early scientist and giving me the latitude to explore my broad interests.

I would like to acknowledge my committee members for their guidance and advice. I would especially like to thank Dr. Shadi Dayeh and Dr. Eric Halgren for their close mentorship.

I would like to acknowledge my current and past lab-mates, Nicholas Rogers, Paolo Gabriel, Tejaswy Pailla, Daril Brown, Wahab Al-asfoor, Kenny Chen, Akin Omigbodun, Venkatesth Elango, Aashish Patel, Francis Beak, Werner Jiang, Kevin Moses, Hannah Chou, Yuchen Wang, and last but not least, Anthony Au. I would also like to acknowledge my mentees, particularly, Alfredo Lucas, Aichen (Claire) Sun, Yevgeniy (Eugene) Arabadzhi, and Stephen Estrin. I hope you have learned a great deal from me, because I certainly learned a great deal from each one of you.

I would like to acknowledge my undergraduate researcher advisor Dr. Wei Lu at the University of Michigan, Ann Arbor for planting the seed of research within me. I am especially grateful for showing me what it means to be passionate about one’s work.

Finally, I would like to acknowledge my wife, Molly, mother, Evan, brothers, Simon and James, close family and friends and of course Diego for helping along my journey. I would be lost without you all.

Chapter 2, in part, has been adapted from material as it appears in the Proceedings of the 2016 IEEE Engineering in Medicine and Biology Conference (EMBC), "A Clinic Compatible, Open Source Electrophysiology System" Hermiz J, Rogers N, Kaestner E, Ganji M, Cleary D, Snider J, Barba D, Dayeh S, Halgren E, Gilja V. The dissertation author was the primary investigator and author of this paper. Chapter 2, in part, also contains material that is in preparation for submission titled "An Open Source Suite of Tools for Clinical Electrophysiology Research", Hermiz J, Ganji M, Paulk A, Rogers N, Lee SH, Hossain L, Kaestner E, Nowacki R, Yang J, Lee JW, Cleary D, Freerksen I, Barba D, Carter D, Carter B, Cosgrove GR, Shih J, Ben-Haim S, Cash S, Dayeh S, Halgren E and Gilja V. The dissertation author was the primary investigator and author of this paper.

Chapter 3, in part, has been adapted from material as it appears in Advanced Functional Materials 2017, "Development and Translation of PEDOT:PSS Microelectrodes for Intraoperative Monitoring" Ganji M*, Kaestner E*, Hermiz J*, Rogers N, Tanaka A, Cleary D, Lee SH, Snider J, Halgren M, Cosgrove GR, Carter B, Barba D, Uguz I, Malliaras G, Cash S, Gilja V, Halgren E, Dayeh S. The dissertation author was the co-primary investigator along with the other starred authors. Chapter 3, in part, has been adapted from material that is in preparation for submission titled "Stimulus Drive Single Unit Activity from Micro-ECoG" Hermiz J*, Hossain L*, Arneodo Z*, Ganji M, Rogers N, Vahidi N, Halgren E, Gentner T, Gilja V, Dayeh S. The dissertation author was the co-primary investigator along with the other starred authors.

Chapter 4 is reprint of material as it appears in NeuroImage 2018, "Sub-millimeter ECoG pitch in human enables higher fidelity cognitive neural state estimation" Hermiz J, Rogers N, Kaestner E, Ganji M, Cleary D, Carter B, Barba D, Dayeh S, Halgren E, Gilja V. The dissertation author was the primary investigator and author of this paper.

VITA

2010-2012	Undergraduate Research Assistant, University of Michigan, Ann Arbor
2012	Bachelor of Science and Engineering, University of Michigan, Ann Arbor
2012-2013	Intern, HRL Laboratories
2014-2018	Graduate Student Researcher, University of California San Diego
2015	Masters of Science, University of California San Diego
2018	Doctor of Philosophy, University of California San Diego

PUBLICATIONS

Hermiz, J., Rogers, N., Kaestner, E., Ganji, M., Cleary, D.R., Carter, B., Barba, D., Dayeh, S., Halgren, E., Gilja, V., 2018. Sub-millimeter ECoG pitch in human enables higher fidelity cognitive neural state estimation. Neuroimage. doi:10.1016/J.NEUROIMAGE.2018.04.027

Ganji, M., Kaestner, E., Hermiz, J., Rogers, N., Tanaka, A., Cleary, D., Lee, S.H., Snider, J., Halgren, M., Cosgrove, G.R., Carter, B.S., Barba, D., Uguz, I., Malliaras, G.G., Cash, S.S., Gilja, V., Halgren, E., Dayeh, S.A., 2017. Development and Translation of PEDOT:PSS Microelectrodes for Intraoperative Monitoring. Adv. Funct. Mater. 1700232. doi:10.1002/adfm.201700232

Hermiz, J., Rogers, N., Kaestner, E., Ganji, M., Cleary, D., Snider, J., Barba, D., Dayeh, S., Halgren, E., Gilja, V., 2016. A clinic compatible, open source electrophysiology system. Eng. Med. Biol. Soc. (EMBC), 2016 IEEE 38th Annu. Int. Conf. 2016–Octob, 4511–4514. doi:10.1109/EMBC.2016.7591730

Wheeler, D., Alvarado-Rodriguez, I., Elliott, K., Kally, J., Hermiz, J., Hunt, H., Hussain, T., Srinivasa, N., 2014. Fabrication and characterization of tungsten-oxide-based memristors for neuromorphic circuits. Int. Work. Cell. Nanoscale Networks their Appl. doi:10.1109/CNNA.2014.6888611

Hermiz, J., Chang, T., Du, C., Lu, W., 2013. Interference and memory capacity effects in memristive systems. Appl. Phys. Lett. 102, 1–6. doi:10.1063/1.4794024

ABSTRACT OF THE DISSERTATION

Electrocorticography on the Micron Scale:

Single Units and Enhanced Neural State Estimation

by

John Hermiz

Doctor of Philosophy in Electrical Engineering (Medical Devices and Systems)

University of California San Diego, 2018

Professor Vikash Gilja, Chair

Electrocorticography on the micron scale (micro-ECoG) is an emerging neural sensing modality that provides a high-resolution view of the brain. Micron scale electrodes measure electrical potential propagated to the brain surface from local and distant current sources. Moreover, electrodes spatially sample the surface of the brain at the micron scale over potentially large regions providing both high resolution and large coverage. Micro-ECoG can be likened to HD monitors, whereas classical ECoG grids are more like Hex LED displays.

In this dissertation, I demonstrate the value of micro-ECoG both in animal model and in humans. I developed a suite of neural acquisition tools (NACQ), which was used to record from human subjects intraoperatively and in the epilepsy monitoring unit for research purposes. These tools provide an affordable alternative to commercial systems and a safer alternative to existing open source systems. I demonstrate that micro-ECoG electrode can sense physiologically relevant features, including single unit activity in songbird. These physiological features measured from micro-ECoG are compared to gold standard probes including penetrating laminar silicon shanks in songbird and clinical ECoG strips in human. Finally, I explored theoretical and empirical instances in which a high density grid of electrodes outperforms sub-sampled lower density grids in discrete neural state estimation. Empirically, I show that when controlling for area and selecting task informative sub-regions of the complete grid, we observed a consistent increase in mean binary classification accuracy with higher grid density; in particular, 400 μm pitch grids outperforming spatially sub-sampled lower density grids up to 23%.

Micro-ECoG is a promising neural sensing modality that may lead to new neuroscientific discoveries and neuroengineering achievements. For example, it may uncover novel neural dynamics from cortical columns or intricate cortical wave patterns important from neural information processing. Micro-ECoG may lead to the development of a high-bandwidth brain machine interface that not only restores abilities of disabled individuals, but augments and enhances abilities of able-bodied people. Neuroscientists and neurotechnologists are poised to make major advances in neuroscience and neuroengineering with the advent of micro-ECoG.

Chapter 1.

Introduction

Neuroscience is in a technology revolution. Catalyzed by the Brain Initiative started in 2013, researchers, now more than ever, are interrogating the brain with exponentially more sensors and stimulators. One recent example, is the Neuropixels silicon probe which has the ability of measuring 384 channels chosen from 960 electrodes (Jun et al., 2017). Stringer and Pachitariu et al reported the ability to record from more than 2998 isolated units from eight probes, making the work a demonstration of the largest number of neurons recorded simultaneously to date (Stringer et al., 2018). While impressive, this number pales in comparison to the number of neurons in the human brain 100 billon (Herculano-Houzel, 2009). Extrapolating out the Moore's law for neurons (Figure 1-1), which is that it takes about 7 years to double the number of neurons recorded from (Stevenson and Kording, 2011), it will take 154 years to record from 10% of the neurons in the human brain.

Fortunately, scientists and engineers appear poised to outperform this trend. Given the significant investment from governments and the private sector for dramatically improving neurotechnology, we should expect to see probes with 10,000s of electrodes by 2020. One promising high channel count technology is a device made by start-up Paradromics. Using an innovative system architecture, they leverage high speed CMOS imaging circuits to capture electrical activity from 10,000 microwires. While significant work remains in order to translate high channel count system towards animals, it seem inevitable that researchers will soon be capable of recording from orders of magnitude more electrodes.

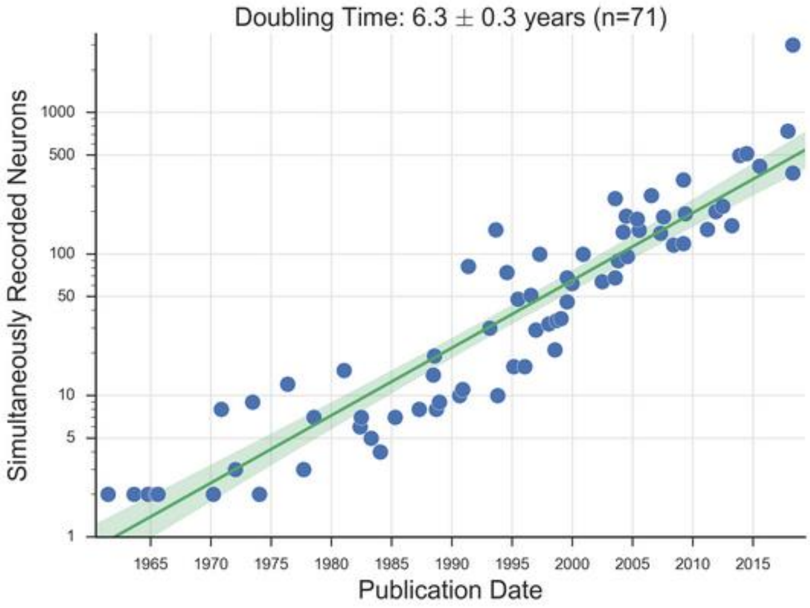

Figure 1-1: Moore’s law of Neuroscience: The logarithm of simultaneously recorded neurons vs publication date. Using line of best fit, the time it takes to double the number of neurons recorded from is 6.3 years. (source: Stevenson Lab, University of Connecticut[1]).

The proliferation of high channel count devices will likely bring about new neuroscience discoveries and enable new brain machine interfaces (BMI) applications. One prominent example that demonstrates the capability of state of the art BMI technology is research from the Neural Prosthetics Translational Laboratory (NPTL) led by Stanford researchers Krishna Shenoy and Jaimie Henderson (Gilja et al., 2015, 2012; Kao et al., 2017; Pandarinath et al., 2017). In this work, researchers used so called Utah arrays to record from cortical neurons in motor regions to drive a cursor on a screen (Figure 1-2). The Utah array is a silicon-based electrode technology which contains 100 electrodes (96 recording) arranged in a square grid spanning approximately 3.6 x 3.6 mm^2. The electrodes are penetrating needles that are 1-3 mm long. With one or two Utah arrays implanted chronically in 3 subjects each, participants were able to type between 13 to 40 correct characters per minute or approximately 3 to 8 words per minute (wpm) (Pandarinath et al., 2017).

---

[1] https://stevenson.lab.uconn.edu/scaling/

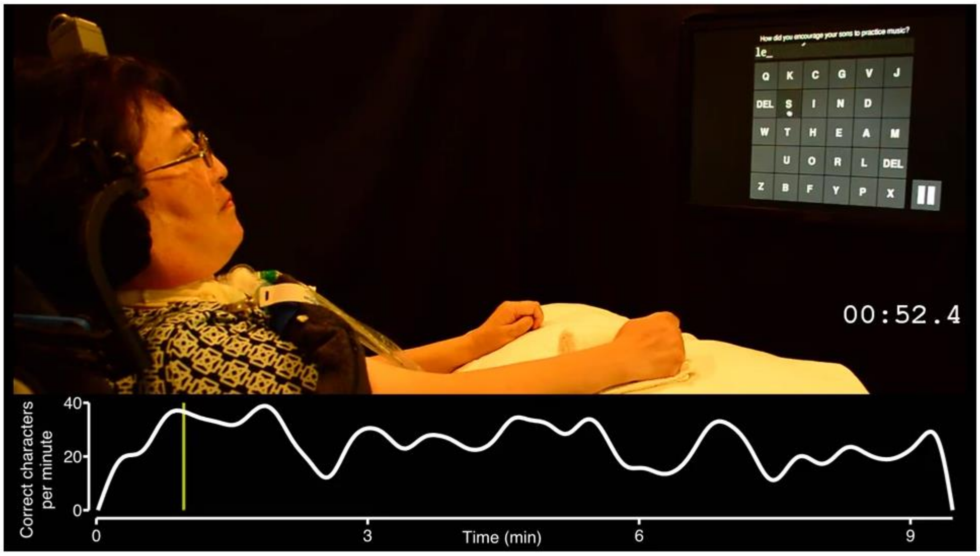

Figure 1-2: State of the art BMI: A quadriplegic uses her brain to drive cursor to point and click letters on a keyboard. On average she is able to type 31.6 correct characters per minutes (or 6.3 words per minutes). Overall this BMI has the highest bitrate of any BMI published (source: eLife Pandarinath, Nuyujukian, et al 2017).

For comparison, communication rates for able-bodied people using smartphones is 12-19 wpm (Hoggan et al., 2008; MacKenzie et al., 2009). This represents the highest performance BMI to date and is reaching a level where disabled individuals would practically benefit from this technology.

Despite the impressive progress that has been made, there is a clear gap in performance between state of the art BMIs and what able bodied individuals can achieve. The brain is able to communicate with the body at a much higher rate than it can with today's machines. Speaking has been estimated to have a communicate rate of 90 to 170 spoken wpm with notable examples outperforming this range (eg. Eminem who spits about 260 wpm in his 2013 hit "Rap God"). Speaking serves as an existence proof that much higher bandwidth BMIs are possible, so the question becomes, how do we improve the bandwidth of BMIs?

The neural interface is an intuitive sub-system to investigate how to increase the bandwidth of BMIs. Current neural interfaces vary in resolution and coverage (Figure 1-3). The popular Utah

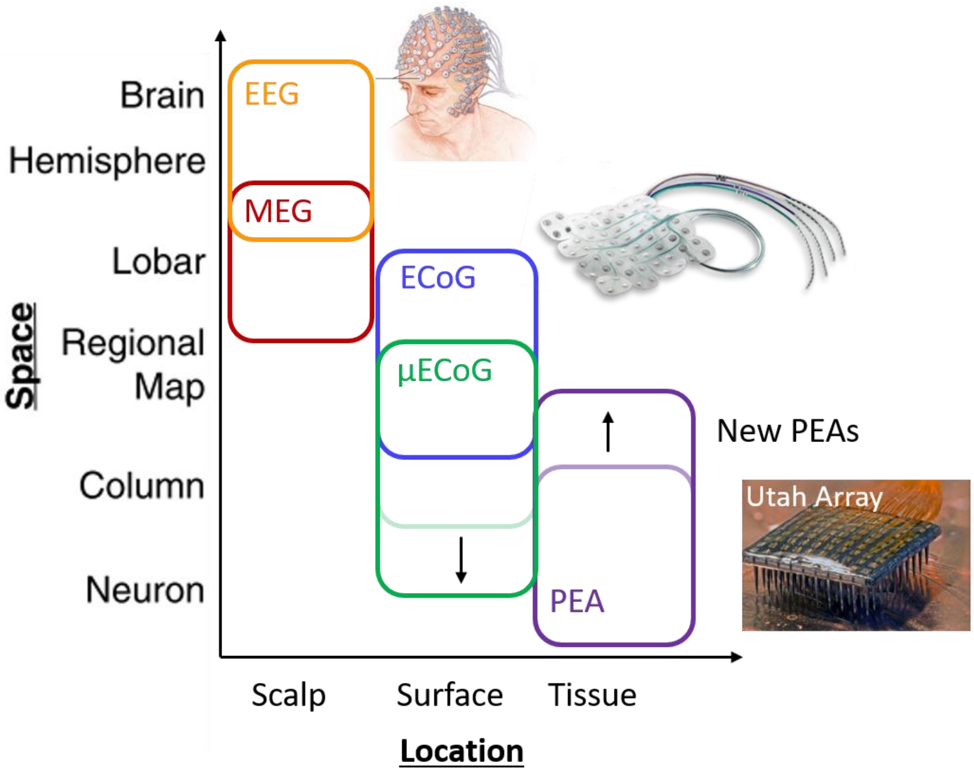

Figure 1-3: Neural Interfaces: Diagram showing the coverage/resolution vs location of various neural interface technologies. micro-ECoG encompasses the best of worlds as it has high resolution and board coverage. While new penetrating electrode arrays (PEA) are pushing the boundary on coverage, micro-ECoG is pushing the boundary on resolution, which is demonstrated in this dissertation. (source: coverage diagram adapted from Nature Neuroscience, Sejnowski et al 2014)

array, the neural interface used in the state of the art BMI discussed previously, has great resolution as it is able to sense single unit activity from cortical neurons, but this comes at the expense of coverage.

The coverage is limited to 3.6 x 3.6 mm^2 in part because the 100 stiff penetrating needles on a ridge substrate needs to be inserted with significant force intracortically (Rousche and Normann, 1992). Increasing the coverage would result in increasing the force of insertion, which increases risk and the larger coverage also increases the probability of hitting blood vessels and causing a stroke. Neuropixels another penetrating probe has several advantages compared to the Utah array. One obvious advantage is that is can record from 384 electrodes chosen from 920

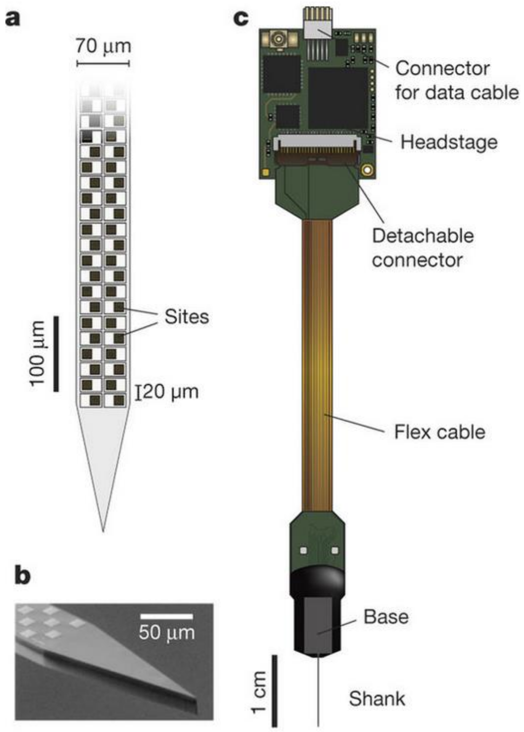

Figure 1-4: Neuropixels probe. a) Electrode spacing and geometry b) Scanning electron microscope image of probe tip c) The probe is monolithically fabricated with silicon circuits for A/D conversion that occurs close to the electrodes (Base). The electrodes and electronics are connected to a flex cable that connects to additional electronics for transmission to a controller. (source: Nature Jun, Steinmetz, Siegle, Denman, Bauza, Lee, et al 2017)

electrodes (Figure 1-4). Furthermore, it has a large span of 10mm and insertion force is likely less of an issue because only one shank needs to displace tissue, but this comes at the expense of coverage, which is limited to only 10 x 0.07 $mm^2 = 0.7$ mm^2. Although the probe has the ability to simultaneously record from deep brain structures such as the hippocampus and the cortex, it is difficult to record over wide swatches of cortex. On the other hand, ECoG arrays have great cortical coverage spanning roughly 80 x 80 mm^2, but is limited in resolution because the electrode diameter is 3 mm and electrode spacing is 10 mm. The large electrode contact ensures that there is a good connection to the brain (low impedance), but has poorer resolution compared to Utah and Neuropixel electrodes. The larger the contact size is the, the larger the effective integration volume of electrical activity surrounding that electrode.

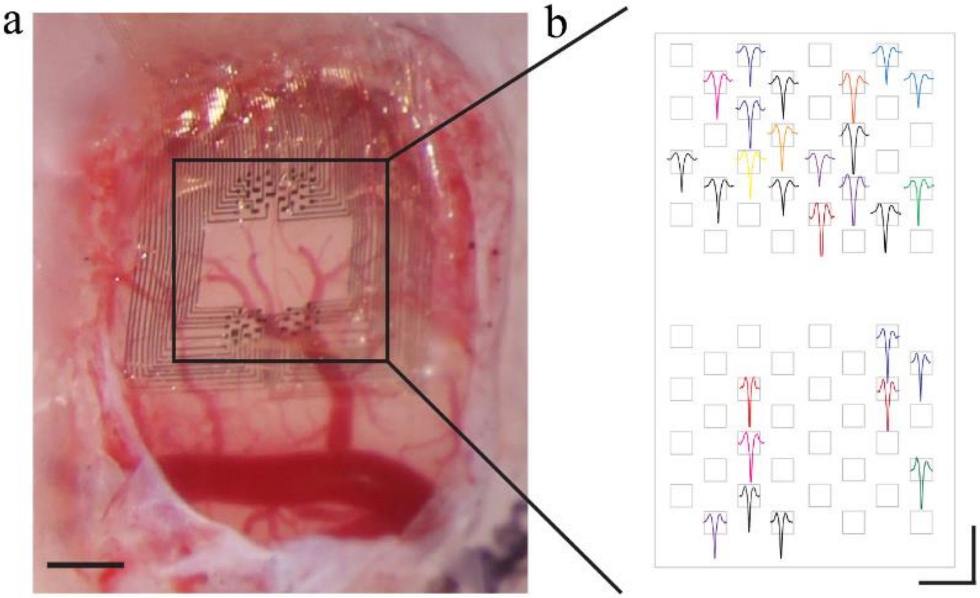

Figure 1-5: Neurogrid, a thin flexible, high density micro-ECoG device is implanted in rat where single units are measured. Electrodes where there are no single units is attributed to the blood vessels. (source: Nature Neuroscience Khodagholy et al 2014)

ECoG electrodes can sense population level activity such as so called high-gamma activity, which has been implicated in sensory processing in multiple regions of cortex (Nathan E Crone et al., 1998; Miller et al., 2007). However, it is unclear how many neurons or synapses contribute to this population level activity. Shrinking the electrode contact size, shrinks the effective integration volume and hence the more localized the measurements are. Furthermore, by shrinking the electrode size, more electrodes can be packed within a given area. Taken together, this modality has higher resolution that ECoG, but has the same great coverage as ECoG. This measurement modality is known as micro-ECoG when the features of device (electrode diameter or electrode spacing) are on the micron scale.

One challenge with shrinking the dimensions of the contact size is a higher probability that the contact will not make contact with tissue (Cunningham, 2017) and higher impedance due to the reduced electrode area (Ganji et al., 2017a). Furthermore, previous methods for manufacturing ECoG arrays relied on manual labor and discrete wires, which is not scalable in terms of drastically increasing channel counts. In the past decade or so, researchers have been pursuing an approach where they utilize micro and nano-fabrication techniques to produce devices with feature sizes as small as 10um and channel counts in the 100s. In one seminal example in 2014, Dion Khodagholy et al presented a device called Neurogrid, which has 256 electrodes, each with an electrode area of 10 x 10 um^2 and an electrode spacing of 30 um (Khodagholy et al., 2014). To overcome the challenges of poor connection to tissue, they fabricated their micro-ECoG device using 2 um thin Parylene C, which is highly conformable so that it can have intimate contact with the brain. Furthermore, they coated their electrodes with PEDOT:PSS, an organic, biocompatible material that reduces their impedance magnitude by roughly 10x compared to gold electrodes (Khodagholy et al., 2014) and recent work has shown a 5x reduction compared to platinum electrodes (Ganji et al., 2017a). They discovered for the first time the ability to record single unit activity from the surface of rodent and human brain (Figure 1-5). This result showed the remarkable resolution of micro-ECoG and has catalyzed the field. In fact, a significant portion of the work presented in this dissertation was motivated by the Neurogrid work!

This dissertation explores the capabilities of micro-ECoG. While there are many types of micro-ECoG devices made of different substrates and electrode materials, the micro-ECoG device I studied was fabricated with a thin sheet of Parylene C to ensure conformality and the electrodes were coated with PEDOT:PSS is reduce impedance akin to the Neurogrid device. These devices were fabricated by collaborators in the Integrated Electronics and Biointerfaces Laboratory led by Prof. Shadi Dayeh. A key aspect of this work was the translation of this micro-ECoG device from laboratory to clinic. I developed a neural acquisition system (NACQ) that records from up to 256 channels and was designed to be compatible for clinical research. This system is described in detail in Chapter 2 along with several other electronics that I built for clinical electrophysiology research. In Chapter 3, I present physiologically relevant signals measured in both songbirds and in human subjects. This includes low frequency oscillations such as alpha wave, high frequency activity also known as high gamma activity and single unit activity. These signals are compared against gold standard electrodes in their respective settings. In the clinic, micro-ECoG is compared against ECoG and in the songbird model, micro-ECoG is compared against intracortical recordings using a laminar probe. In Chapter 4, the value of high density grids is explored by sub-sampling high density grids producing “virtual” lower density grids and comparing their relative performance in estimating discrete neural states. This approach was performed using a modeling framework that relates spatial properties including signal fall off and correlation to a decoding metric and empirically from data acquired in two human subjects. Finally, Chapter 5, summarizes this body of work, discusses future directions and neuroethical considerations.

Chapter 2.

Data Acquisition

In Chapter 2, I describe neural data acquisition tools that were used to record from human subjects in the clinic. This suite of tools have been open-sourced for other researchers to use and provide an affordable alternative to commercial systems and a safer option than currently available open source systems.

2.1. Introduction

Current methods for acquiring clinical ephys are limited in terms of either functionality, transparency, or accessibility. Clinical data acquisition systems have several limitations including limited access by researchers or knowledge of data acquisition parameters, and in some cases sub-optimal specifications. One example where these limitations are evident is recording single unit activity from microelectrodes. Typical clinical systems are not designed to measure these types of signals are therefore often do not sample quickly enough. Even a new system such as the Natus Quantum from Natus Medical Incorporated (Pleasanton, CA) has a maximum sample rate of 16.4kHz, which is sub-optimal for spike sorting. Furthermore, recording at such high sampling rates is not typical in clinical practice and may be limited by clinical information technology resources or regulations.

Deploying an independent commercial research system such as Blackrock Microsystems (Salt Lake City, UT) and Tucker-Davis Technologies (Alachua, FL) overcomes many of these challenges. These systems are designed for many research applications and the data acquisition parameters can be defined by researchers. However, these systems can be cost prohibitive for many

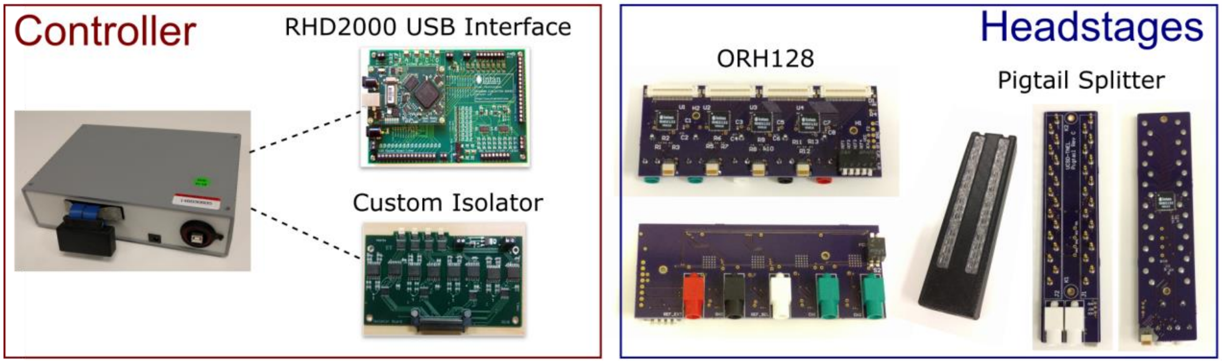

Figure 2-1: Suite of clinical electrophysiology tools. The left red box shows the controller and its main components: RHD2000 USB Interface from Intan Technologies and a custom built power and digital isolator, which are housed in a water resistant enclosure. The controller accepts up to 4 SPI lines from Intan Technologies digital acquisiton amplifiers, which translates to a maximum of 256 channels for recording when using RHD2164 amplifiers. The right blue box shows custom headstages designed for clinical use: ORH128 and Pigtail Splitter. The ORH128 is a single, compact PCB that can amplify 124 channels of biosignals. The Pigtail splitter allows users to tap into existing clincial ECoG data acquistion pipelines, which incorporate commonly used Cabrillo^{TM} compliant connectors.

research groups. Furthermore, propriety systems tend to be opaque with respect to technical details, which limits control and flexibility.

An alternative to commercial systems are open source technologies such as Open Ephys and Open BCI, which are transparent and at least 10x cheaper per channel than commercial systems (Ghomashchi et al., 2014; Insanally et al., 2016; Kinney et al., 2015; Newman et al., 2012; OpenBCI, 2013; Siegle et al., 2015; Trumpis et al., 2017a, 2017b; Woods et al., 2015). Although efforts have been made towards introducing open source tools towards human recording, particularly EEG (Black et al., 2017; OpenBCI, 2013), there has been a lack of tools developed specifically for intracranial research. Here, we present our suite of clinical ephys research tools that are based on Intan Technologies (Los Angeles, CA) (Hermiz et al., 2016). We present 3 main components: (1) neural acquisition controller; (2) 128-channel headstage; (3) and a 32-channel headstage that splits signals from typical intracranial data acquisition pipelines to an independent research system. These tools were validated by conducting 3 separate clinical experiments from 3 different subjects – one for each tool. The organization of the manuscript is as follows: in the Methods section, we describe each tool and the corresponding experiment; in the Results section, we present the experiment recordings and data analysis; in the Discussion section, we describe the significance and limitations of the suite; and finally, in the Conclusion section, we summarize features that make our system attractive for users.

Table 2-1: List of various commonly used ephys systems. Grey rows are commercial systems and white rows are open source systems. Highlighted in bold is the presented system.

System	***Ch #***	***Fs***	***Bit-Depth***	***Isolated***
BlackRock-Cerebus	128	30 KHz	16	Y
TDT-PZ2	256	50 KHz	18	Y
Open Ephys	**256**	**30 KHz**	**16**	**N**
NeuroRighter	64	1 MHz	16	N
Nspike	127	30 KHz	16	N
UCSD	256	30 KHz	16	Y
Willow	1024	30 KHz	16	N

2.2. Methods

This section is organized into 3 parts for each component: Neural Acquisition Controller, ORH128 and Pigtail Splitter (Figure 2-1). A table of neural acquisition tools for easy referencing is provided (Table 2-2). Each subsection is divided into two parts: “Component Description” and “Experiment” which describes the component and experimental details for each tool. Detailed

Table 2-2: Overview of clinical neural acquisition tools

Component Name	**Chan. #**	**Description**
Neural Acq. Controller	256	Drives Intan amplifiers
ORH128	128	Headstage
Pigtail Splitter	32	Headstage and splitter
Flex Adapter	64	Passive electrode adapter

documentation and design files of these components, as well as additional resources not presented here such as 3D printable case designs can be found on Github and CircuitMaker[2]. Three human subjects from UC San Diego La Jolla Medical Campus (La Jolla, CA) and Brigham and Women's Hospital (Boston, MA) were recruited and provided informed consent in compliance with Institute Review Board (IRB) approved protocols. The IRB protocols for UC San Diego and Brigham and Women's Hospital was approved by UC San Diego Human Research Protections Program and The Partners Human Research Committee, respectively.

---

[2] https://github.com/TNEL-UCSD/nacq and https://circuitmaker.com/User/Details/John-Hermiz-2

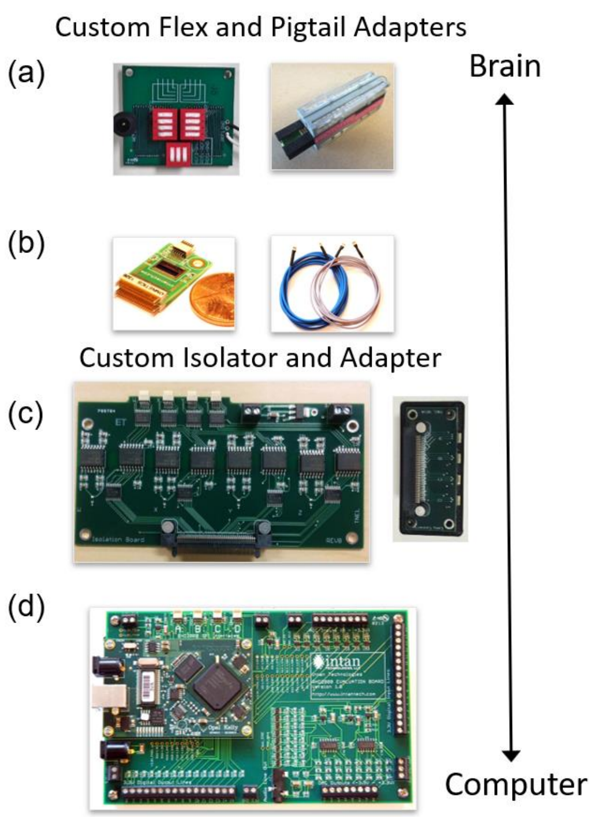

Figure 2-2: Component breakdown of system: (a) Electrode adapters: (left) connects to flat flexible cables (FFC) of 32 or 64 channels with 0.5 mm pitch and features switches that allows the user to short various electrodes to reference; (right) can connect up to four 16 channel standard pig tail connectors. Both adapters mate to Intan RHD2164 or RHD 2132 headstages using an Omnetics connector (part #: A79032-001). (b) (left) Intan RHD2164 headstage and (right) Intan SPI cable (c) (left) Custom power isolator that can handle 4 RHD2164 headstages or up to 256 channels and (right) accompanying adapter. (d) Intan RHD2000 acquisition board.

2.2.1. Neural Acquisition Controller

2.2.1.1. Component Description

The neural acquisition controller, or simply controller, acquires data from Intan Technologies amplifiers. It consists of two main modules, the RHD2000 USB Interface Board and a custom power and digital isolator (Figure 2-1). The controller can accept input from 4 separate amplifiers (or strictly speaking 4 MISO lines), which translates to a maximum of 256 recording channels when using the RHD2164 (64-channel) amplifiers. It can also sample up to 30kHz[3], which is higher than the 20kHz we previously reported (Hermiz et al., 2016). The controller also features 8 analog inputs (0 – 3.3 V) via BNC bulkhead connectors. These channels can be used to supply event triggers, synchronization pulses, or other experimental signals that need to be recorded alongside the neural recordings. The controller is housed in a 25 x 18 x 6.5 cm water-resistant case and features several bulkhead connections to prevent liquids from damaging the electronics. This is a particularly important consideration when obtaining recordings in potentially wet environments such as the operating room (OR).

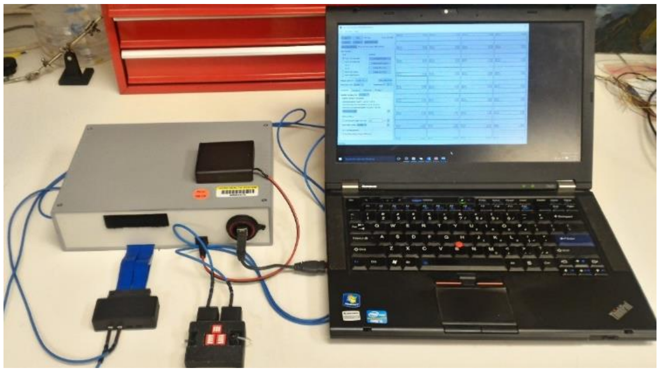

Figure 2-3: Ephys system connected and running using a modified version of the Intan's compiled software. The power isolator and RHD 2000 Board are housed in grey enclosure. Two RHD2164 headstages are connected to the system to the electrode adapter housed in 3D printed cases.

---

[3] Sometimes the controller is unable to recognize the RHD2164 at 30kHz because of a general software issue related to the SPI delay finding algorithm implemented in the RHD2000 software. This issue only affects RHD2164 because it uses a double data rate (DDR) SPI protocol as noted in the software and has since been optimized by Intan Technologies.

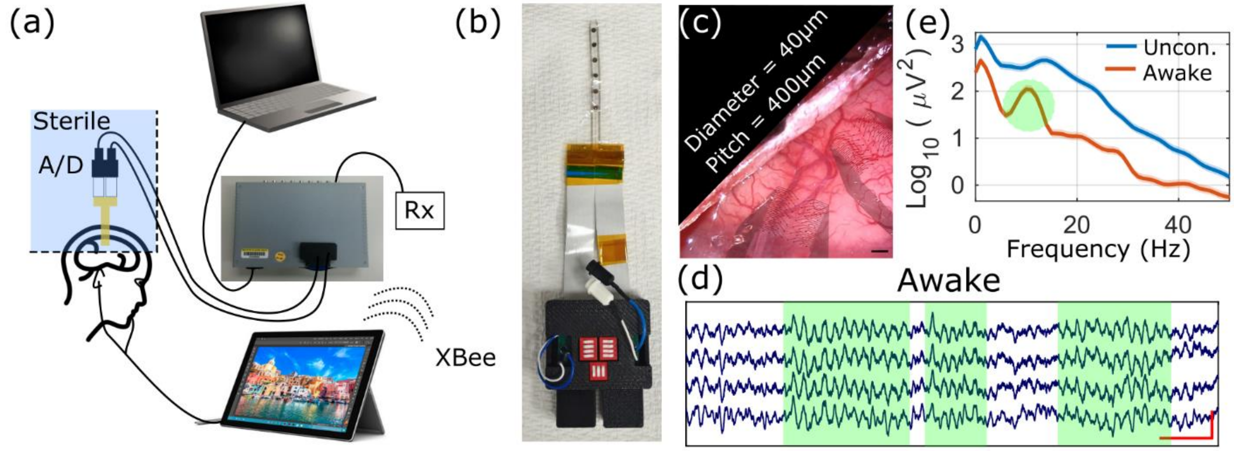

Figure 2-4: Controller experiment and validation. (a) Overview of experimental setup featuring the neural acquisition controller (grey box). The controller drives the amplifier + digitization electronics (A/D headstage), which is placed in the sterile field. The controller also has 8 analog input lines (0 – 3.3V) to capture experimentally relevant signals such as external triggers simultaneously with the neural recordings. In this schematic, the controller receives a signal from a small controller that communicates to a Microsoft surface over Zigbee (XBee) wireless protocol. (b) Picture of µECoG device which also consists of 6 macro-electrodes. (c) Picture of 2 µECoG devices placed on the brain of S1. (d) Sample recordings acquired intraoperatively while the subject was awake. Transient increases in alpha oscillations are highlighted by green shading. Horizontal and vertical scale bars are 0.5sec and 100µV, respectively. (e) Power spectrum from two epochs: awake (red) and unconscious (blue), which illustrate the neurophysiological differences from these two states.

The isolator board consists of two main isolator chips: ADUM6000 for power isolator and ADUM4401 for digital isolation. These components use inductive iCoupler technology from Analog Devices (Norwood, MA). They provide protection from 5kV rms for 1-minute and comply with the following medical safety rating standards: UL-1577 and IEC-60601. The isolator is placed between the amplifier and the RHD2000 USB board to provide protection from possible malfunctions from the RHD2000 USB board, computer, and other electronics as well as power surges from the wall outlet.

2.2.1.2. *Experiment*

We used the controller to record signals from a µECoG (micro electrocorticography) electrode array acutely implanted during an awake craniotomy case at the UC San Diego Thornton

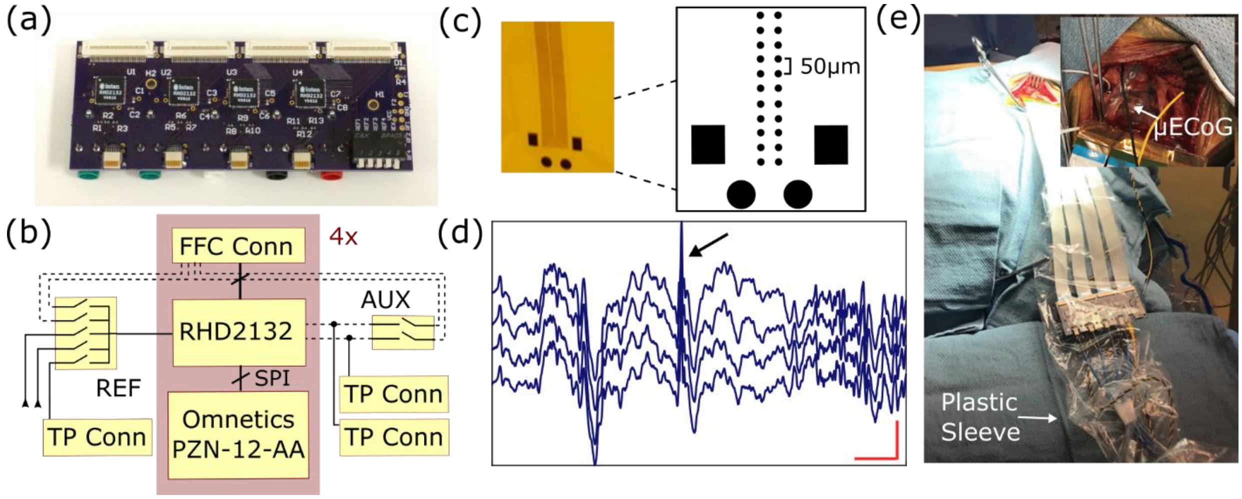

Figure 2-5: ORH128 headstage (a) Picture of ORH128 board (b) High-level schematic of ORH128 circuit (c) Picture of 128 channel μECoG grid and zoom-in showing electrode layout. There are 4 macro-electrodes, 2 rectangles and 2 circles, and a 64 x 2 matrix of micro-electrodes spaced 50μm apart. (d) 5 second sample recording from 4 μECoG channels showing an interictal epileptiform discharge, which is indicated by the arrow. The red horizontal and vertical scales are 0.5 sec and 200 μV, respectively. (e) Picture of surgical field showing craniotomy, electrode cables and ORH128 board covered with a plastic sleeve. Inset shows the μECoG grid and a clinical strip placed on the brain of S2.

Hospital Operating Room. The subject (S1) was a 35-year-old male with left mesial temporal lobe epilepsy refractory to medical therapy. μECoG was recorded while the patient was awake and performing an audio task. The device used to record μECoG consisted of a 7x8 grid of microelectrodes coated with PEDOT:PSS and the electrodes had a diameter of 50μm and a spacing of 400μm (Figure 2-4B-C). Additionally, the device had 6 electrodes with diameter (3mm) and spacing (1cm) similar to clinical ECoG. Despite the small geometry of the microelectrodes, the PEDOT coating facilitated electrode impedances that were typically below 30kΩ (at 1kHz) as has been reported previously (Ganji et al., 2017a). The device was fabricated at UC San Diego Calit2 nano3 cleanroom as described in (Ganji et al., 2017b).

Prior to surgery, the μECoG device and parts of our recording system that were in the sterile field were sterilized (Figure 2-4). The μECoG device was sterilized with steam sterilization

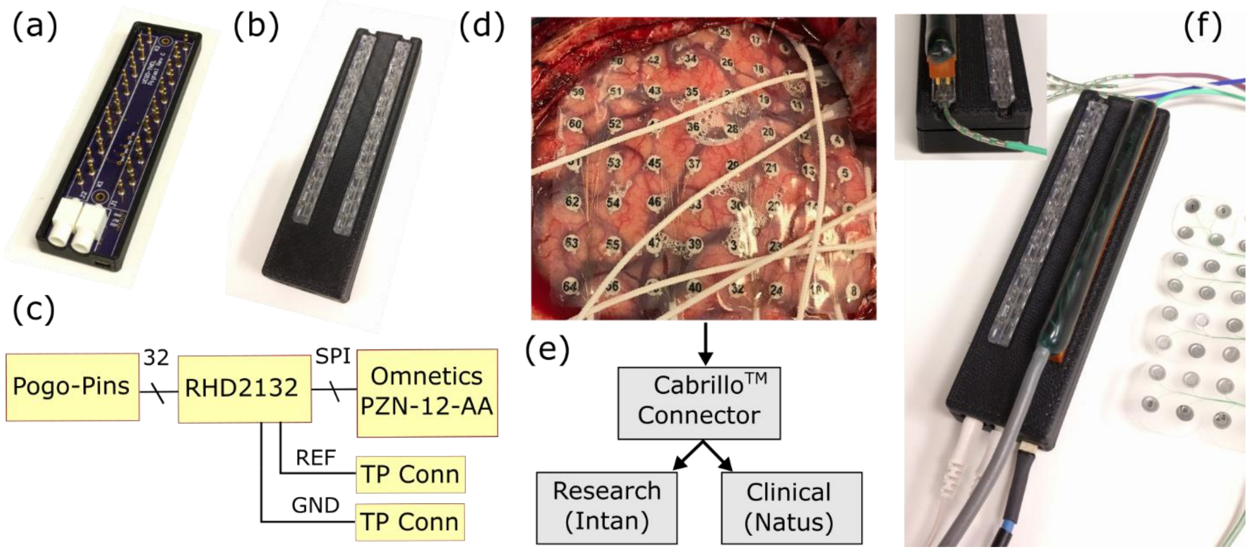

Figure 2-6: Pigtail splitter headstage. (a) Picture of Pigtail splitter with top case deattached showing the PCB. (b) Picture of Pigtail splitter fully assembled. (c) High-level schematic of Pigtail splitter board. (d) Picture of craintomy with a 8x8 ECoG grid and several strips placed on the brain of S3. (e) Block diagram showing that the ECoG signals will be split and go to 2 recording system: research (this work) and clinical (Natus). (f) Picture of Pigtail splitter fully connected. The cable that connects into the Pigtail splitter is part of the clinical data acquistion system and is used to clamp the pigtail cable placed within the Pigtail connector (inset).

at 132 ^{o}C for 10 minutes, a procedure that does not affect the performance of the electrodes (Uguz et al., 2016). The electronics, including the electrode adapter, amplifiers (RHD2164), and cables, were sterilized using an electronics compatible, low temperature process called STERRAD® (Advanced Sterilization Products (ASP), a Division of Cilag GmbH International, a Johnson & Johnson company) at 50 ^{o}C for 45 minutes. STERRAD® uses a combination of hydrogen peroxide vapor and low temperature gas plasma to eliminate toxic residue. We packaged the adapter and amplifier in 3D printed cases made of PLA plastic to reduce the risk of damage during handling and sterilization (Figure 2-4B). After the first 3-5 iterations, we found no visible deficits in the electronics and they were fully functional; however, in subsequent iterations, we noticed that the solder mask on the PCBs started to delaminate, rendering it unusable in the clinic. Delamination may be possible to prevent by coating the PCBs with a protective layer such as Parylene C or Liquid Crystal Polymer (LCP); however, we have not tested this approach.

Before placing the μECoG device on the brain, we tested the device in the operating room using a saline bath. A small bucket was filled with saline and a separate needle electrode was used for ground. A subset of the macroelectrodes on the μECoG device were connected to reference using switches on the electrode adapter (Figure 2-4B). Then impedance tests were run to ensure functionality of a majority of the electrodes. Afterwards, the μECoG device was placed on top of arachnoid mater and a separate needle electrode was placed near the craniotomy. The location of the implant was left posterior superior temporal gyrus. Approximately 20 minutes total of baseline activity, task activity and anesthetized activity were recorded. The subject was tasked to monitor a stream of spoken and noise-vocoded bi-phoneme phrases (e.g. taw, koo), which were presented via a Microsoft Surface tablet (Figure 2-4A). Trial onset times were relayed to the controller by sending pulses wirelessly over Zigbee to an Arduino based controller (Rx), which was connected to an analog input of the controller as illustrated in (Figure 2-4A). Recordings were sampled at 20kHz and then downsampled offline to 2kHz for analysis.

2.3. ORH128 Headstage

2.3.1.1. Component Description

The ORH128 headstage is a single board (9.75 x 4.00 cm) that can amplify 124 channels (Figure 2-5A). It consists of 4 RHD2132 amplifier chips and is intended to be more convenient than using separate Intan demo boards, which have only 1 chip integrated per board. This is particularly useful in the OR where handling multiple components in a strict sterile environment can be challenging. We chose to use RHD2132 instead of RHD2164 amplifiers at the time of design because they were conveniently packaged in a QFN (quad flat no-leads) which allows them to be surface mounted on a PCB. However, Intan now offers the RHD2164 in a BGA (ball grid array) package allowing easy assembly on to a PCB. A future redesign with the RHD2164 would facilitate reducing the cost and potentially size of the board. The current board features two banks of switches for configuring reference and for supplying auxiliary signals such as scalp EEG, EKG, or EMG. The user has the option of connecting any one of the four designated electrode channels to reference or using a separate reference electrode, which can be connected to the board via standard clinical touch proof connectors. Similarly, up to two external signals can be supplied to the ORH128 (Figure 2-5B). Finally, the board uses Flat Flexible Connectors (FFC) as opposed to Omnetics connectors as the electrode connector because FFC are less expensive ($2 vs $50 each) and are more readily available[4].

2.3.1.2. Experiment

To demonstrate the utility of the ORH128 headstage, we used it to record μECoG intraoperatively at Brigham and Women's Hospital. S2 was a 33 year-old man with medication-refractory epilepsy secondary to a low-grade lesion in the left temporal lobe. Pre-operative investigations revealed that electroclinical seizures started from the left anterior and middle temporal areas. Pathology ultimately revealed low grade neuroepithelial tumor. S2 was unconscious throughout the procedure and periods of epileptiform activity were induced by administration of methohexital (Brevital) for the purposes of seizure foci mapping. The geometry

---

[4] Typical lead times for FFC connectors are 3-5 days vs Omnetics connectors which has a lead time of 6 weeks.

of the μECoG differed from that described in *Neural Acquisition Controller*, but the methods used to fabricate it were the same. The device consisted of 2x64 microelectrodes with a diameter of 30μm and spacing of 50μm. There were also 4 macroelectrodes that can be used for reference (Figure 2-5C); however, in this experiment we chose to use separate needle electrodes from Medtronic (Minneapolis, MN) placed near the craniotomy for reference and ground.

The same sterilization procedures for the μECoG device were used as *Neural Acquisition Controller*. However, to avoid degradation issues with the electronics, we decided not to sterilize them and instead placed them in a sterile plastic sleeve (Figure 2-5E). Clinicians found that extending the length of the ribbon cable from 4 inches (length used in prior experiment *Neural Acquisition Controller*) to 10 inches allowed for easier handling. Although increased cable length has the potential for degrading signal quality, we decided that the additional clinical flexibility outweighed the potential benefit of shorter cables. The same testing procedures were used to ensure μECoG device functionally as described in *Neural Acquisition Controller* and the device was placed on the left anterior superior temporal gyrus. Recordings were sampled at 30kHz and then downsampled to 1kHz for offline analysis.

2.4. Pigtail Splitter

2.4.1.1. Component Description

The Pigtail Splitter, or splitter for short, is a 32-channel headstage (Figure 2-6A,B,F) that is intended to acquire data from typical clinical neural acquisition pipelines without compromising the clinical system workflow or recordings. The splitter achieves this by utilizing commonly used Cabrillo^{TM} compliant connectors, which connect pigtail cables from clinic ECoG devices (eg. strip and grid electrodes) to clinical amplifiers (Figure 2-6D,E). Typically, the pigtail cable is threaded through the Cabrillo^{TM} compliant connector and the amplifier cabling plugs into the connector, which clamps the pigtail cable (Figure 2-6F). Holes were drilled on the back side of the Cabrillo^{TM} compliant connector to allow pogo-pins to make electrical contact with the plug. Pogo-pins were soldered onto a board that also contained a RHD2132 for data acquisition (Figure 2-6A-C). Additionally, the splitter features touch proof connectors for ground and reference electrodes. Finally, it is compact (11 x 2.8 x 1.5 cm) enough to be included in a headwrap. The splitter allows researchers to use their own recording system, giving them additional control and flexibility in data acquisition than if they were to use a clinical data acquisition system.

2.4.1.2. Experiment

We validated the Pigtail splitter by using it during a semi-chronic ECoG case at UC San Diego Jacobs Medical Center. S3 was 67 year-old female with idiopathic complex partial seizures. S3 was implanted with subdural ECoG electrodes for several days to localize seizure foci.

Prior to surgery, we sterilized the Pigtail splitter using STERRAD® as described in *Neural Acquisition Controller*. Sterilizing the Pigtail splitter was not necessary since it was handled after the craniotomy was complete when sterility is no longer observed. However, surgical and clinical workflows may vary by institution and clinician, which ultimately dictate the sterilization protocol. Two out of 4 pigtail cables from an 8x8 clinical ECoG grid from Ad-tech Medical were threaded into the splitter. The ECoG electrodes had a diameter of 3mm and a spacing of 1 cm. Clinical acquisition cables were then plugged into the splitter. The ECoG grid was placed over left frontal, parietal and temporal lobes. Two different sets of electrodes from a 4-electrode strip were used for reference and ground for the clinical and research system. Separate electrodes were used for reference and ground for both systems.

The following day, recordings from both the clinical and research system were acquired. The clinical data acquisition was the Natus Quantum. The Quantum is capable of recording from 256 channels at up to 16.4kHz; however, data was collected at 1024Hz as this sampling rate is standard clinical practice for intracranial implants at UC San Diego. We used the pigtail splitter and controller to collected data alongside the Quantum for an hour at 1kHz, but it is important to note that our system can sample up to 30kHz. A random sequence of pulses were supplied to the optical trigger input of the Quantum and an analog input of the controller, so as to time align the recordings across the two systems post-hoc. Neural recordings were collected while the subject was resting.

For data analysis, we performed the following preprocessing steps in order to compare the recordings between the clinical and research system. We time aligned the signals by computing the cross-correlation of the random pulse sequence. Then we arbitrary selected a 100 sec window of data. We found that clinical and research recordings had the opposite polarity so we flipped the clinical signals. Then we re-sampled clinical recordings down to 1kHz. Finally, since the DC filters were substantially different, we high pass filtered both sets of signals at 2Hz using a 6th order forward-backward Butterworth filter. All data analysis was performed using MATLAB (Natick, MA).

2.5. Results

To demonstrate functionality of the neural acquisition controller, we demonstrate that the controller captures clinically relevant signals (Figure 2-4D,E). Broadband time-series across several channels and seconds show transient alpha (10Hz) oscillations while S1 was awake and performing the audio task intraoperatively (Figure 2-4D). These alpha oscillations are also

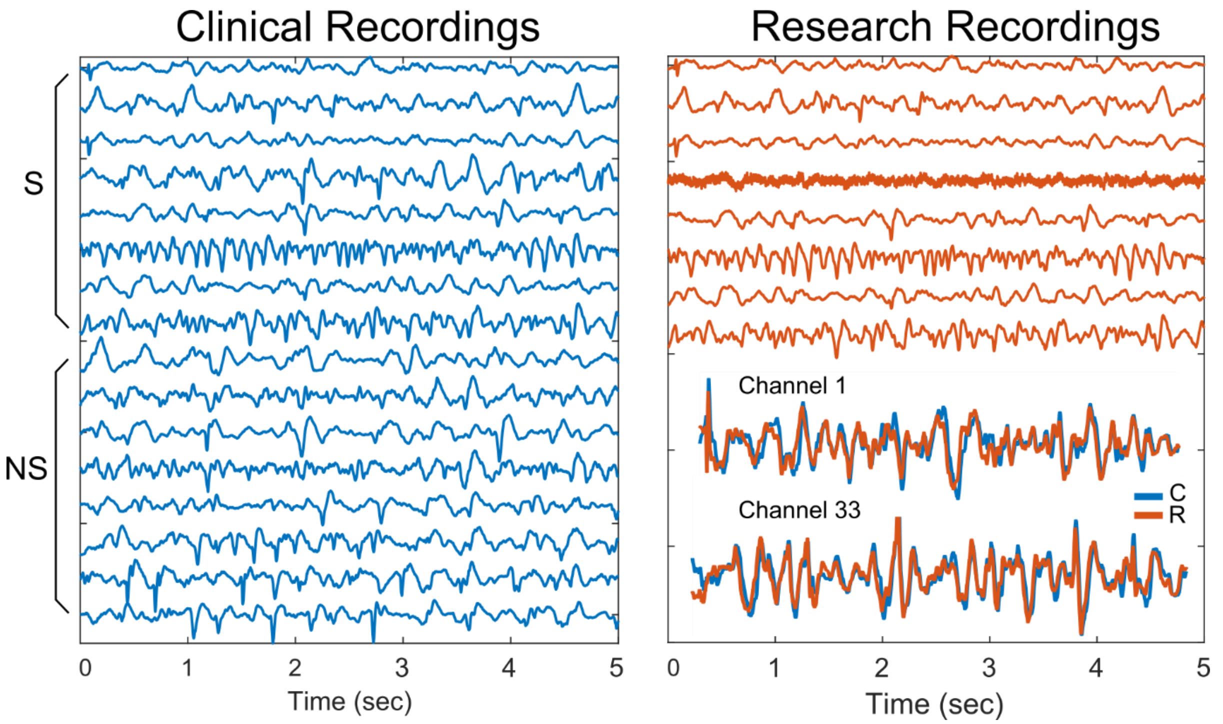

Figure 2-7: Concurrent time series from clinical and research system. (a) A 16 channel sub-set of recordings acquired by the clinical system. The top half of recordings are from channels that were split and also went to the research system. The bottom half of the recordings are from channels that were not split. (b) An 8 channel sub-set of recording acquired by the research system, which are connected to the same electrodes as the top half of (a). The inset of (b) shows the recordings from two electrodes recorded by both system. The blue trace "C" was recorded by the clinical system and the red trace "R" was recorded by the research system.

prominent in the power spectrum where there is a peat at 10Hz (Figure 2-4E). Finally, the spectral properties change substantially when S1 was heavily sedated and unconscious. In this state, we observed a broad increase in signal power across frequencies and the alpha peak was eclipsed (Figure 2-4E). These results are consistent with neurophysiology, demonstrating that our system captured biologically relevant neural activity (Breshears et al., 2010; San-juan et al., 2010).

We validated ORH128 by observing epileptic activity from the recording μECoG electrodes. Methohexital (Brevital) was administrated intraoperatively with the intention of increasing epileptiform activity for seizure foci localization (Kofke et al., 1997). After administration,

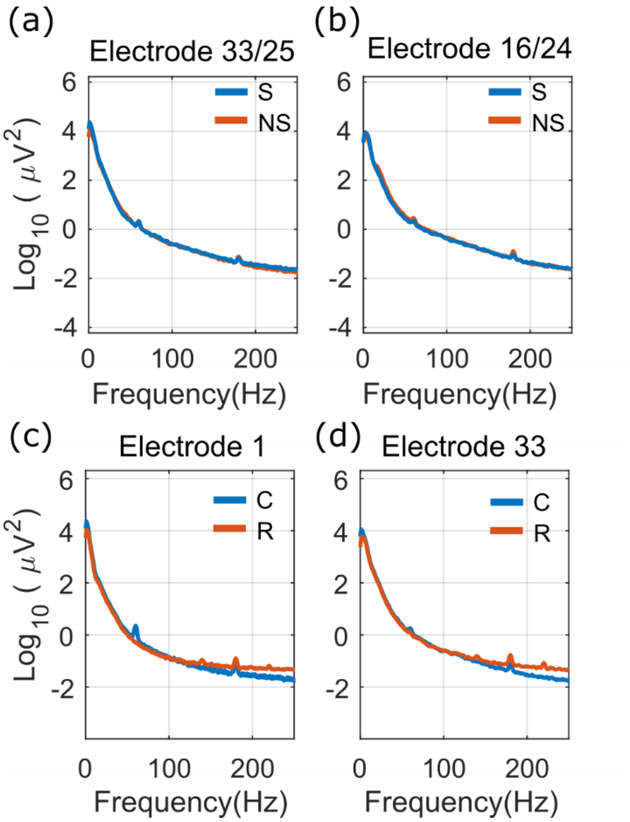

Figure 2-8: Power spectrum (PSD) of split vs not split clinical channels and clinical vs research channels. (a) Clinical channel PSDs from split (blue "S") and not split (red "NS") channels. The split signal comes from Electrode 33 and the non-split signal comes from Electrode 25. (b) Same as (a), but for Electrode 16 (split) and Electrode 24 (not split). (c) Electrode 1 PSD from clinical system (blue "C") and research system (red "R"). (d) Same as (c) but for Electrode 33.

interictal epileptic discharges were observed in the recordings (Figure 2-5D). This result demonstrates the functionality of our system by capturing clinically relevant neural activity.

To validate the Pigtail splitter, we compared signals simultaneously record by both clinical and research systems. A 5 second snippet of recordings from split and non-split electrodes show no obvious difference (Figure 2-7A). Furthermore, recordings from the same electrodes made by the research system appear to be very similar, except for one corrupted channel (Figure 2-7B). By plotting recordings from the same electrode across the two systems from two arbitrarily chosen electrodes, we see that they are in fact highly similar with only small variations in the signal. The references for both systems were within 2 cm of each other, and this slight difference may explain the minor signal variations.

The power spectrum (PSD) of 2 split and not split clinical channels were compared Figure 2-8A-B). Although PSDs of signals acquired on different electrodes are compared, we chose signals that came from neighboring electrodes to minimize the potential differences introduced by the electrodes themselves. We found that the PSDs of 2 pairs of split and not split signals were very similar (Figure 2-8A-B). This is consistent with the observation that the time series between split and not split clinical channels do not have any obvious differences and provides additional support that the splitter does not affect clinical recordings. When comparing PSDs from 2 clinical and research channels, we find that they are similar, but start to deviate at 100Hz (Figure 2-8C-D). This can be explained by the larger input-referred noise in the Intan amplifiers (2.4 μV_{rms}) than in the Quantum amplifiers (1.8 μV_{rms}). On the other hand, we see a larger line noise peak at 60Hz in

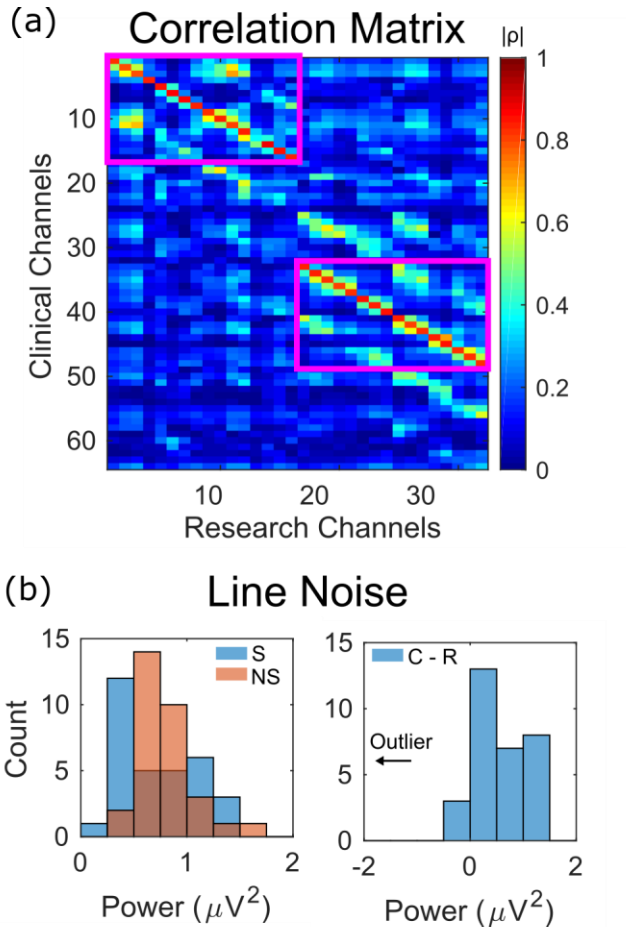

Figure 2-9: Overall signal comparison between clinical and research systems. (a) Correlation matrix between the 64 clinical (rows) and 32 research channels (columns), which shows that the split signals in pink boxes (electrodes 1-16 and 33-48) captured by both system are highly similar. Channel 13 is the exception because there was likely a poor connection at that pogo pin. The colorbar represents the absolute value of correlation. (b) 60 Hz line noise analysis. The left panel is a histogram of line noise power from each channel in the research system. The blue bars ("S") correspond to signals that were split and the red bars ("NS") were not split. The line noise from the split and non-split channels were deemed not significantly different based on statistical hypothesis testing ($p = 0.19$, $n = 32$, Wilcoxon rank sum test). The right panel show the difference in the line noise between the two systems from the split channels. Except for one outlier (channel 13), the histogram of "C-R" clincal minus research system line noise is shifted positively indicating that more line noise is consistenly picked up by the clinical system. This was confirmed by hypothesis testing ($p = 3.6e{-}5$, $n = 32$, Wilcoxon signed rank test).

the clinical recordings (Figure 2-8C-D). This likely due to the fact that the research system was run using a battery pack while the clinical system was plugged into wall power. We computed the correlation between all clinical and research channels and found that the magnitude of the correlation was greater than 0.7 for all but one channel. There was one channel that was not correlated with the clinical channel, because it appeared to be a corrupt channel as previously mentioned (Figure 2-7B). This channel was corrupt possibly because there was poor contact between the pogo pin and the plug for this site.

The 60Hz line noise power was computed for all clinical recordings and was used as measure of signal integrity. We compared the distribution of 60Hz power between the split and non-split electrodes (Figure 2-9B) and found that there was no significance difference ($p = 0.19$, $n = 32$, Wilcoxon rank sum test). This suggests that the Pigtail splitter does not impact the clinical recordings. We also compared the 60Hz power of clinical and research recordings from the same electrodes. The distribution of 60Hz power from the clinical minus the research recordings is positively shifted indicating that there is more line noise picked up on by the clinical system (Figure 2-9B), which is consistent with PSDs from the two example electrodes (Figure 2-8). Hypothesis testing confirmed that this distribution was significantly shifted away from 0 ($p = 3.6e\text{-}5$, $n = 32$, Wilcoxon signed rank test).

2.6. Discussion

We present a set of tools that we believe are useful and accessible for clinical electrophysiology research. The controller has clinically compatible features including electrical isolation, water resistance, and a small footprint. The controller's small format factor (25 x 18 x 6.5 cm) allows it to be brought into space constrained environments such as the OR with minimal impact to clinical workflows. In contrast, commercial systems such as Blackrock's Cerebus^{TM} system require large digital to analog converter units (42.5 x 32.5 x 8.8 cm), which are roughly the size of a desktop computer. The isolation and water-resistant features make it more ideal to use in the clinic than the RHD2000 USB interface board alone. Intan also provides an isolated controller in a chassis, but is roughly 2x the cost and 2x wider than the presented controller. However, the Intan controller accepts up to 8 MISO lines, which equates to 512 channels maximum, double what the presented controller can accept. The RHD2000 USB interface board can also accept 512 channels. Experimental needs and budget constraints will dictate the ideal controller to be used. In future work, it will be quite feasible to double the capacity of channels in the presented system from 256 to 512 channels by using a different digital isolator such as Si8660-63 by Silicon Labs (Austin, TX), which would allow for two MISO lines to pass thru the isolation stage.

ORH128 is a128-channel headstage designed with the clinic in mind. We improved on our first generation system reported in (Hermiz et al., 2016), which featured multiple Intan headstages and an adapter board by integrating all of these components together on a single board for ease of use in the OR. Additionally, the board features commonly used touch proof connectors for reference, ground and auxiliary channel input and output as well as a switch array to configure the appropriate reference. One limitation of the ORH128 is that the FFC connector is difficult to handle under OR constraints. The FFC connector has a small latch that must be opened and closed to secure the FFC cable, which is difficult to do over the sterile wrap and when hands are double gloved. Additionally, the FFC connector limits channel scalability since it is a linear connector. Important future work is to find a more ergonomic and scalable, high density electrode connector that is readily available and affordable.

The Pigtail splitter can augment standard clinic intracranial data acquisition pipelines so that researchers can obtain their own stream of neural recordings. This gives researchers greater control and flexibility over data acquisition. As an example, this could enable real-time experiments such as brain-machine interface or seizure prediction studies. Furthermore, our system can sample at 30kHz which is typically higher than what clinical systems can achieve or higher than what would be permitted by clinicians. Sampling at 30kHz would enable spiking sorting from microelectrode recordings. Finally, our results seem to suggest that our system with a battery pack can be more immune to line noise than a commonly used clinical data acquisition system, which is an additional benefit towards researchers. One limitation of the Pigtail splitter is its size. Although we made a concerted effort to minimize its size, it is still larger than what is desirable in the clinic. The splitter did fit in the headwrap, but it is difficult to imagine placing additional splitters in a headwrap. The challenge with reducing its size further is that we are constrained by the size of the Cabrillo^{TM} compliant connectors. Important future work might be to use newer slimmer connectors such as the inline mini-PMT by PMT Corporation (Chanhassen, MN) that are becoming more popular across epilepsy clinics.

2.7. Conclusion

We present an open source suite of research based clinical electrophysiology (ephys) tools that we claim make clinical ephys more accessible to researchers. These tools incorporate features such as power and digital isolation and standard clinical connectors that make them suitable for clinical research. The tools are orders of magnitude lower cost than commercial systems, while our tools achieve specifications (eg. 30kHz sample rate and up to 256 channels) that meet the needs of many researchers. It is our hope that these tools will benefit researchers and promote increased research in human electrophysiology.

These tools, and in particular, the neural acquisition controller was used to collect data from human subjects that was pertinent to the development of this dissertation. These data are presented in Chapter 3 and 4.

This chapter, in part, has been adapted from material as it appears in the Proceedings of the 2016 IEEE Engineering in Medicine and Biology Conference (EMBC), “A Clinic Compatible, Open Source Electrophysiology System” Hermiz J, Rogers N, Kaestner E, Ganji M, Cleary D, Snider J, Barba D, Dayeh S, Halgren E, Gilja V. This chapter, in part, also contains material that is in preparation for submission titled “An Open Source Suite of Tools for Clinical Electrophysiology Research”, Hermiz J, Ganji M, Paulk A, Rogers N, Lee SH, Hossain L, Kaestner E, Nowacki R, Yang J, Lee JW, Cleary D, Freerksen I, Barba D, Carter D, Carter B, Cosgrove GR, Shih J, Ben-Haim S, Cash S, Dayeh S, Halgren E and Gilja V.

Chapter 3.

Physiologically Relevant Features

In order to validate micro-ECoG recordings, we need some ground truth or a priori knowledge of the brain signals. Luckily, I can rely on countless research articles for this a priori knowledge and stand on the shoulders of neuroscience giants so to speak. In Chapter 3, I extract physiologically relevant features from neural recording to validate micro-ECoG. First, we demonstrate that single units, the hallmark neural signal, can be sensed from micro-ECoG in songbirds. Then we show that micro-ECoG translated to the clinic, captures relevant signals including alpha oscillations, inter-ictal discharges and high-gamma activity.

3.1. Songbird Micro-ECoG

3.1.1. Introduction

Songbird (Oscines) have sophisticated speech and auditory capabilities which is evidenced by their ability to listen and eventually learn to produce a complex repertoire of vocalizations. Therefore, it has been argued that songbirds are a relevant model for speech, auditory and language processing (Bolhuis and Gahr, 2006; Brainard and Doupe, 2002; Nottebohm, 2005). It is then natural to consider songbirds as a model for developing neural speech prosthesis, which has emerged as an exciting area in neuro-translational research (Herff et al., 2015; Jiang et al., 2016; Kellis et al., 2010; Leuthardt et al., 2011; Martin et al., 2014; Mugler et al., 2014; Pailla et al., 2016; Pasley et al., 2012; Pei et al., 2011). In fact, recent work by Arneodo et al explored this approach and demonstrated the ability to reconstruct song produced by Zebra Finch from neural activity alone (Arneodo et al., 2017). This is a significant achievement towards the realization of a functional songbird speech decoder, but this approach is limited by the degradation of signal quality, namely single unit activity, of intraparenchymal probes. Intraparenchymal probes, colloquially referred to as depth probes here, penetrate and displace brain tissue, and provoke tissue reactions, thus limiting the longevity of high fidelity signal acquisition (Biran et al., 2005; Jorfi et al., 2014; Vadim S Polikov et al., 2005; Rivnay et al., 2017; Schlenoff and Xu, 1992). Less invasive micro-electrocorticography (micro-ECoG) electrodes that lay on the surface of the brain may lessen the tissue reaction and thus facilitate longer, more robust recordings. In the seminal work by Khodagholy et al, they present Neurogrid, a micro-ECoG electrode that detects single unit activity in rats and humans (Khodagholy et al., 2014). They demonstrate that the average spike amplitude was consistent over the course of 10 days, which provides preliminary evidence that micro-ECoG permits the acquisition of stable single unit activity chronically.

We propose using micro-ECoG for neural interfacing in a songbird speech decoder. Towards this end, we investigated the ability of micro-ECoG probes to record single unit activity acutely in an anesthetized European Starling (Sturnus vulgaris). We report the ability of micro-ECoG to record single unit activity in Starling for the first time. To explore the functionality of these putative neurons, we presented the anesthetized Starling with auditory stimuli (eg. the subject's own song). We report that single unit activity (SUA) from surface channels is driven by the presentation of auditory stimuli and is akin to the SUA from depth channels. To date, this is this first time that a relationship between sensory input and surface SUA has been demonstrated and we are the second group to demonstrate surface SUA, to the best of our knowledge.

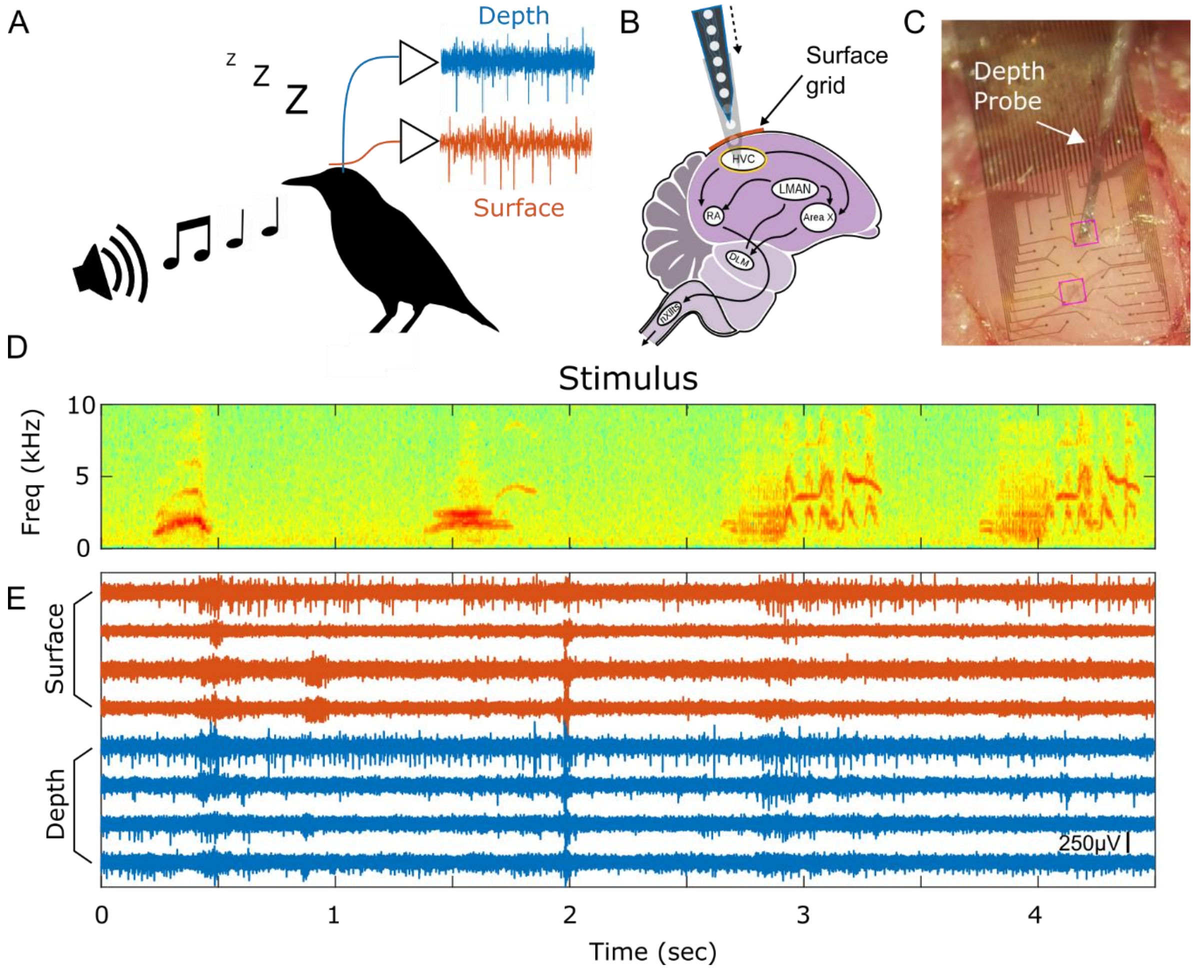

Figure 3-1: Experimental paradigm and spiking activity. A) Anesthetized European Starling hears auditory stimuli (eg. it's own song), while simultaneously recording from the surface and depth. B) The target recording site is HVC. The surface probe is placed over it while the depth probe is inserted into it. HVC is at the top of the auditory and speech hierarchy as shown in the schematic of the songbird circuit. C) Picture of surface grid placed on top of the brain and a depth probe penetrating into the brain through the surface grid. Highlighted in pink rectangles are the two holes where the depth probe can be inserted. D) Spectrogram of the stimulus, which in this case, was the bird's own song. E) Eight high-pass filtered time series from 4 surface (red) and 4 depth (blue) electrodes showing spiking activity. The amplitude scale bar is 250μV and is located in the bottom right of the figure.

3.1.2. Methods

3.1.2.1. Probes

The surface probe was manufactured in house at UC San Diego, nano3 using microfabrication techniques similar to those described in (Ganji et al., 2017b). It consists of a 2.9μm thin Parlyene C substrate, gold interconnects and electrodes coated with PEDOT:PSS. The electrodes have a diameter of 20 μm and a spacing of 200 μm and is arranged in a grid consisting of 32 electrodes as shown in Figure 3-1. Functional electrodes usually have an impedance around 75 kΩ as measured in a saline bath. The surface probe has two square holes to allow for a penetrating depth probe to be inserted in between surface electrodes (Figure 3-1). The depth probe is a commercially available silicon shank manufactured by NeuroNexus (Ann Arbor, MI). One of three versions were used throughout the experiments: 16 site probe with 50 μm spacing (A1x16-5mm-50-177-A16), 32 site probe with 3 columns of electrodes staggered with an electrode spacing of 25 μm (A1x32-Poly3-5mm-25s-177-A32) and 32 site probe with a linear array of electrodes spaced 20 μm (A1x32-Edge-5mm-20_177-A32). The contact area of the 16 and 32 site probes is 177 μm^2. Functional electrode impedance was typically 1 - 2 MΩ as measured in a saline bath.

3.1.2.2. Experiment

Acute experiments were performed on anesthetized European Starlings, which typically weigh 55 - 102 grams are 21.6 cm long. The craniotomies targeted the HVC nucleus, which is known to be important for auditory and speech processing and generation in other avian models such as the well-studied Zebra Finch (Fee et al., 2004; Hahnloser et al., 2002; Schmidt and Konishi, 1998; Vu et al., 1994; Yu and Margoliash, 1996). European Starlings were used for this study because their larger cranium made implantation of the surface probe easier compared to Zebra Finch, which weigh 12 grams and are 9.9 to 10.9 cm long. A 3 x 3 mm window is opened up, the dura is resected, and a thin 100 – 300 μm layer called the tubercle is also removed from the surface. To ensure intimate contact between the surface probe and tissue, cerebral spinal fluid is removed from the surface of the brain by using a pipet to suction the fluid. The surface probe is then placed on top of the brain and then the depth probe is slowly lowered into the brain via one of the two holes.

Pre-recorded songs that the Starling sang and other stimuli such as songs of other birds of the same species and time reversed songs were played to the Starling while anesthetized. For each recording block, two types of stimuli were played to the bird in a random order and in a random interval with a random inter-stimuli interval uniformly distributed between 7 to 12 seconds. Thirty to 60 trials of each stimuli are played to the bird for each recording block.

Electrophysiological recordings of both surface and depth probes were performed by the same data acquisition system, Intan RHD2000 from Intan Technologies (Los Angeles, CA). The Intan RHD2000 USB Controller was connected to a RHD2116 or RHD2132 headstage that was connected to the depth probe and a separate RHD2164 headstage was connected to a surface probe. The following adapter boards were used to connect the probe to the Intan headstage: Flex Adapter[5] (Hermiz et al., 2016) for the surface probe and a Plexon (Dallas, TX) N2T A32-HST/32V adapter for the depth probe. Recordings were sampled at either 20kHz or 30kHz and data was acquired using either the Open Ephys GUI (Siegle et al., 2017) or RHD2000 software provided by Intan. Default Intan filter settings were used with cutoffs set at 0.01 Hz and 7.5kHz for data acquisition.

---

[5] https://github.com/TNEL-UCSD/nacq

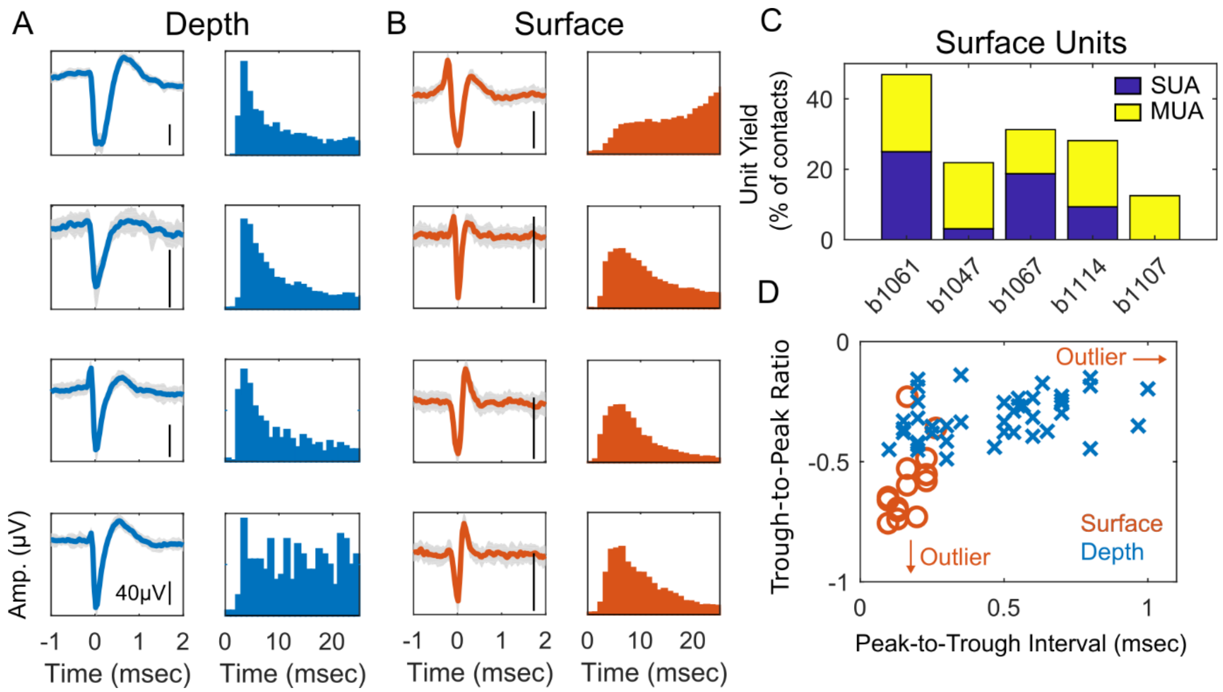

Figure 3-2: Single unit characteristics. Example of A) depth and B) surface single units waveforms and their respective inter-spike interval (ISI) histograms. These waveforms are averages of 50 uniformly sampled spike snippets. The y-scale bar indicate 40 µV in amplitude. B) Same as A) but for surface single units. C) Surface unit yield as a percentage of total number of contacts. The stacked bar plot shows the percentage of single units (SUA) and multi-units (MUA) for each subject. D) Scatter plot showing trough-to-peak ratio vs peak-to-trough interval for all putative neurons. The surface SUA and depth SUA are plotted as a red circle and blue X, respectively. The red arrows indicate an outlying sample from a surface SUA in the direction that the arrows point.

3.1.2.3. Data Analysis

All recordings were eventually converted to KWD format an HDF5 based data model. Data recorded in Intan's RHD format was converted to KWD using the following library[6]. For visualizing high frequency activity, the raw recordings were high pass filtered forward and backwards using a 3rd order Butterworth filter with a cutoff frequency of 300 Hz and stored as a separate KWD file. Spike sorting was performed using KiloSort (Pachitariu et al., 2016). The post-hoc merge algorithm included in the KiloSort software was used after the main KiloSort algorithm assigned spikes to clusters. The clusters were manually verified by inspecting spike snippets,

---

[6] https://github.com/zekearneodo/intan2kwik

correlograms and principal components space using Phy and custom Matlab scripts. Spike clusters were labeled either single unit (SUA), multi-unit (MUA), noise, or artifact – noise and artifact clusters were thrown out for all analyses. Clusters were deemed to be SUA if a sub-sampling of spike waveforms exhibited features that are stereotypic of action potential waveforms and if all the spikes in that cluster did not have a substantial number of refractory period violations (eg. little to no spikes 0 to 2 ms after spiking). Clusters were deemed to be MUA if the spike waveform resembled that of an action potential waveform but had a substantial number of refractory period violations. An example of each cluster label is provided in the supplementary materials (S-Figure 1).

For stimulus-based analysis, the number of spikes was binned using 5 ms windows (or equivalently 200 Hz). A smoothed estimate of the average spike count was computed by taking the average across all trials and then smoothing with a 5th order moving average filter. The amplitude envelope of the auditory stimulus was estimated by using the Hilbert transform, low pass filtering and then downsampling down to 200 Hz to match the sample rate of the spiking activity.

The delay between the auditory stimulus and neural response was estimated by using the autocorrelation. That is, the autocorrelation between the average smoothed spike count and the amplitude envelope of the auditory stimulus was computed for lags less than 200 ms – lags greater than 200 ms are assumed to not be physiologically plausible and thus spurious. The peak (in absolute value) lag is determined to be the delay and the auditory stimulus is shifted forward by this amount so that the neural response and auditory stimulus are coherent.

We decided to focus our analyses on the initial response to the stimulus because it appeared to yield the largest and most robust neural response. The onset of the first sound was found by manually inspecting the spectrograms of the stimuli. 200 ms prior to the onset and 300 ms after the onset were taken to be the window of interest over which the subsequent metrics were computed.

Table 3-1: Single unit characterization and statistics.

	Surface (n=18)	**Depth (n=41)**	**P-Value**	**Test**
Duration	0.167 ms	0.5 ms	8.2e-5	Rank sum
Spike Rate	2.68 Hz	1.11 Hz	0.040	Rank sum
Amplitude	56.7 μV	107.2 μV	1.8e-3	Rank sum
Trough/Peak	-0.63	-0.33	3.9e-6	Rank sum
Symmetry	-0.72	-0.15	9.6e-4	Rank sum
Bursts or Not	9/18=50%	31/41=76%	0.053	Chi-square

The Pearson correlation is computed between the average spike count and envelope of the auditory stimulus. Since there are 2 auditory stimuli played to the subject, the one that yielded the higher correlation was considered. Correlations that had a $p > 0.01$ (Bonferroni corrected) were deemed spurious and not included in the presented analyses. Similarly, only the effect size and the lag of neural responses that were significantly correlated with the auditory stimulus are considered.

In order to quantify the magnitude of the response, a metric we call the effect size was computed. The definition of effect size is: $(\mu_{peak} - \mu_{base})/\sigma_{base}$, where μ_{peak} is the average spike count in 5 ms bins in a window of +/- 50 ms about the peak response. μ_{base} is the average spike count in 5 ms bins in a baseline window lasting 1 sec prior to the stimulus presentation. Finally, σ_{base} is the standard deviation of the spike counts in the baseline window.

Unless specified otherwise, all analyses were performed using custom Matlab software (Natick, MA).

3.1.3. Results

3.1.3.1. Spike characterization

Single and multi-unit activity from the surface probe was detected across all 5 subjects studied. Specifically, in 4 out of the 5 subjects, single unit activity (SUA) was detected, whereas multi-unit activity (MUA) was detected in all subjects (see Methods and Supplementary section for definition of SUA and MUA as well as examples). The unit yield, which is defined to be the number of channel where there is SUA (or MUA) divided by the total number of physical electrodes, for the surface probes ranges from 0 to close to 40% across the subjects (Figure 3-2). In all but two cases, the surface probe SUA and MUA yield was below 20%. Similarly, for the depth unit yield, 2 out of 4 subjects had low yield (below 20%), but in the other two cases yield was greater than 50%, reaching nearly 100% in one case (S-Figure 1). Examples of SUA detected on both the depth and surface probe are shown in Figure 3-2A-B along with their respective inter-spike interval (ISI). The depth and

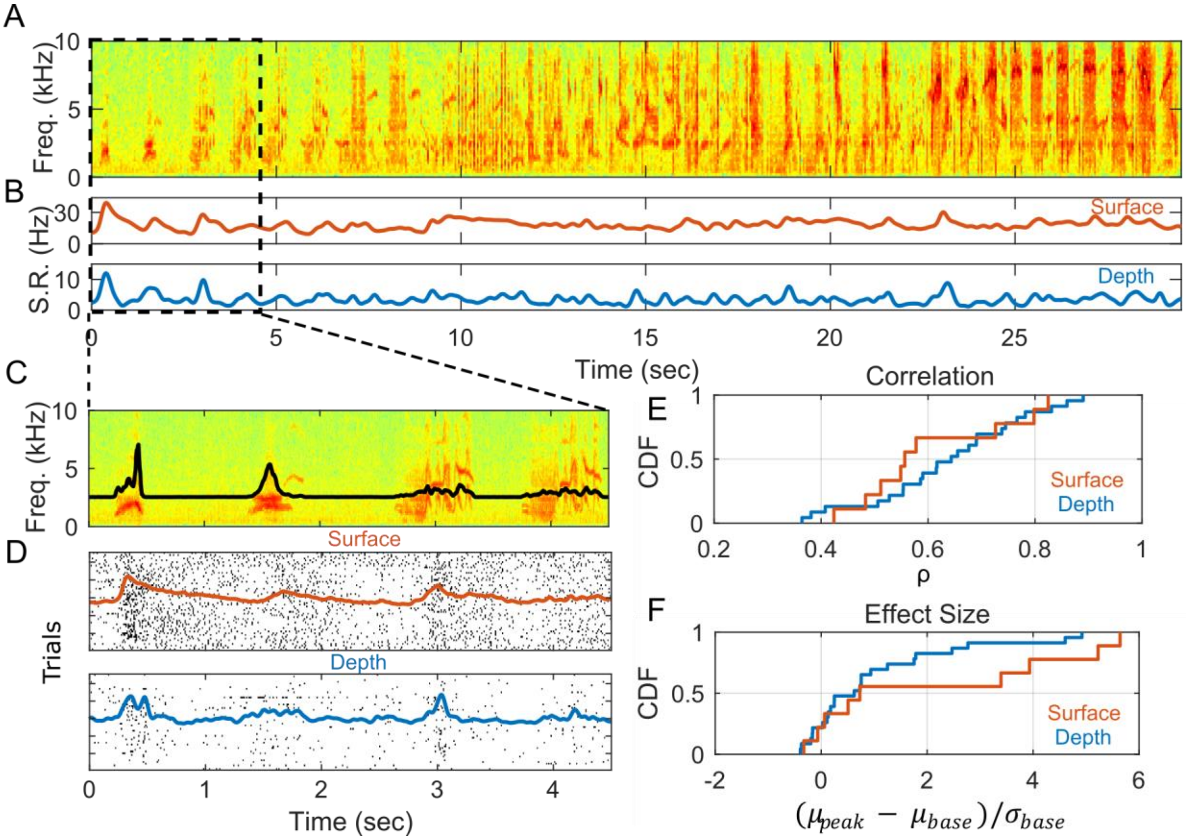

Figure 3-3: Stimulus driven responses. A) Spectrogram of a stimulus example. In this case, the stimulus was bird's own song. B) Spike rate for a surface (red) and depth (blue) single unit. C) Zoom-in of A on the first 4.5 sec. The black line is the envelope of the amplitude. D) Rasters showing single unit activity from a surface (red) and depth (blue) unit over repeated trials. The red and blue lines is the average smoothed activity across trials for the surface and depth unit, respectively. Empirical cumulative distribution function for E) correlation and F) effective for surface (red) and depth (blue) units.

surface spike waveforms appear to have different features such as the duration and relative trough and peak amplitudes. Here, the peak is defined as the minimum point in the waveform and the trough is the maximum point that occurs after the peak. Furthermore, duration is defined to be the time between the peak and trough. The depth spikes appear to have a longer duration and larger peak relative to trough than do the surface spikes. This appears to be the case over the entire dataset of depth and surface SUA (Figure 3-2D). In Figure 3-2D, the peak-to-trough latency is plotted against trough-to-peak ratio for all depth and surface SUA. There is a clear cluster of surface SUA in the lower left portion of the graph, whereas the depth SUA occupies the upper portion of the graph. Additional spike statistics are computed for depth and surface SUA (Table 3-1). The median values for depth and surface as well as the p-value comparing the distributions of surface and depth for each statistic is listed in (Table 3-2). The p-values for all these features are either close to or well below 0.05 indicating that there is systematic difference in the surface and depth SUA characteristics

Table 3-2: Stimulus evoked responses statistics

	Surface (n = 9 out of 18)	**Depth (n = 23 out of 41)**	**P-Value**	**Test**
Correlation	0.56	0.64	0.45	Rank sum
Effect Size	0.73	0.62	0.40	Rank sum
Latency	65 ms	30 ms	0.67	Rank sum

3.1.3.2. Stimulus response

The depth and surface single unit activity (SUA) was modulated by auditory stimuli. An example of the modulation can be seen in Figure 3-3A-D. In Figure 3-3A-C, the spectrogram of the auditory stimulus, which in this case was the bird's own song, is plotted alongside the average spike rate that has been smoothed using a Gaussian filter. Both the depth and surface spike rates appear to modulated by features of the stimuli, particularly in the beginning of the stimuli. Figure 3-3C-D, zooms in on the activity that happen within the first 4.5 sec of the stimuli. Figure 3-3C shows the spectrogram of the stimuli with the amplitude envelope plotted on top of the spectrogram. Figure 3-3D shows rasters with average spike rate plotted on top. There appears to be a strong response due to the initial sound and a smaller response at 3 sec due to the presentation of a particular vocalization. However, when this vocalization is presented again at around 4 sec and it does not appear to illicit a noticeable response. The responsivity to various vocalizations and contexts in HVC in anesthetized European Starling has not been well studied. To date, the authors have only identified one study in HVC of anesthetized European Starling that characterizes neuronal response to various categories of auditory stimuli (George et al., 2005). Important future work, will be to fully characterize the effect of various sounds and their context on SUA and MUA in HVC of anesthetized and awake European Starling. For this work, we focused on characterizing the response due to the initial sound presented to the subject because the neural response appeared to be strongest and most robust during this window. This large initial response is not surprising because prior to the presentation of the stimuli there is a prolonged period of silence (7- 12 seconds). The initial response was initially quantified by first computing the Pearson correlation between the average spike count and the amplitude envelope of the stimulus after correcting for neural delay (see Methods). The correlation was computed in a 500 ms window centered about the onset of the first sound. Correlations were deemed spurious if they had an associated $p < 0.01$ (Bonferroni corrected). To quantify the magnitude of the response, a metric we call the effect size was computed for neural responses that were significantly correlated with the stimulus. The effect size captures the difference in spiking activity between a peak response window and a baseline window normalized by variation in the baseline spiking activity (see Methods for precise definition). The empirical cumulative distribution function (CDF) for depth and surface correlation and effect size are shown in Figure 3-3E-F. The CDF for correlation appears to indicate that there is slightly more correlation among the depth SUA than the surface SUA, while the CDF for the effect size appear to indicate that the effect size is larger for surface SUA than depth SUA. In both cases, statistical tests return p-values well above 0.05 indicating the difference in correlation and effect size between these two populations is not significant (Wilcoxon rank-sum test). It is important to note that this analysis was limited to $n_{sur} = 9$ and $n_{dep} = 23$ for surface and depth SUA respectively, because SUA with non-significant responses were eliminated for this analysis. The small number of datapoints limits the statistical power in the hypothesis testing. The median values of correlation, effect size and latency as well as associate p-value are listed in Table 3-2.

3.1.4. Discussion

Single unit activity (SUA) from the surface of Starling brain was presented. Surface SUA waveform and spike timing characteristics appear to be distinct from depth SUA properties. In particular, peak-to-trough latency was significantly shorter for surface SUA than depth SUA (Figure 3-2). Furthermore, the ratio of trough-to-peak amplitudes was closer to unity in absolute value than depth SUA indicating the peak and trough amplitudes are closer to each other for surface SUA (Figure 3-2). This suggests at least two possibilities: surface and depth are biased to sample different 1) cell types or 2) locations on a cell. Different waveforms shapes can be explained by both hypotheses (Buzsáki et al., 2012). HVC consists of several types of neurons including projections neurons, which target other nuclei including robust nucleus of arcopallium (RA) and basal ganglia nucleus (X) as well as interneurons, which stay within HVC. These different neuron types have different morphologies (Benezra et al., 2018) but it is unclear what the superficial spatial distribution of these neurons are and if surface electrodes are biased towards sensing a particular neuron type or part. In mammalian brain, cortical neuronal organization and morphology has been well characterized. In recent work by Hill and Rios et al, they performed a modeling study using rodent anatomy to investigate which neurons theoretically contributed to micro-ECoG. Their modeling results indicate that only superficial layer I neurons no deeper than 60μm can be sensed by current micro-ECoG electrodes (Hill et al., 2018). An analogous study in songbird would help to determine the origin of surface single units in this class of animals and is important future work.

Stimulus driven surface SUA is also demonstrated. Examples of putative neuron average spike rate show a marked increase when initially presented with an auditory stimulus after a silence period of at least 7 sec. Overall, half (n_{sur} = 9 out 18) of the surface single units were considered to be significantly correlated to the amplitude envelope of the initial phase of the stimuli. Correlation values of surface SUA were slightly lower, yet comparable to depth SUA. Effect size for surface SUA was larger than depth SUA and interestingly, stimulus to neural response latency was larger for surface SUA. However, differences between correlation, effect size and latency of surface and depth SUA were not significant as determined by hypothesis testing. This could be in part to the limited number of data points (n_{sur} = 9 and n_{dep} = 24), which reduces statistical power. A larger number of stimulus driven single units would help to elucidate differences, if they exist, in the response of surface and depth SUA, which is important future work.

For this work, we focused on the initial neural response due to the first sound presented in the stimuli after a silence period. We chose this window because it appeared to produce a large and robust neural response. However, it is important to investigate the neural response of a wide spectrum of sounds and contexts. An important question that remains is whether the sensory encoding of superficial neurons is rich enough to probe the neural circuits of speech and auditory processing. Indeed, this will need to be investigated prior to realizing a speech decoder in songbird.

Another important future direction of this work is to design a chronic experiment with an awake, free behaving songbird. In a chronic experiment, it will be possible to attempt to decode produced vocalizations in a manner similar to (Arneodo et al., 2017). We hope that this work will lead towards the realization of a chronic speech decoder in songbird and the eventual translation to human speech prosthetic that will aid disabled individuals who do not have the ability to speak.

3.2. Human Micro-ECoG

Now, I describe micro-ECoG recorded from human subjects recorded in the clinic. Using the neural acquisition presented in Chapter 1 and PEDOT coated micro-ECoG arrays, we measured a collection of relevant physiological signals in the micro-ECoG recording.

3.2.1. Methods

3.2.1.1. Acquisition

Patients S1-S3 undergoing clinical mapping of eloquent cortex provided informed consent to have the microarray placed on their pial surface and to participate in a 10-minute task. The PEDOT microarray was placed on the superior temporal gyrus (STG): anterior STG for Subject 2 (S2) and posterior STG for Subject 1 & 3 (S1, S3). UC San Diego Health Institutional Review Board (IRB) reviewed and approved study protocol.

Patient S4 provided informed consent to have microarray placed on their pial while unconscious. The electrode was implanted on the lateral surface of the temporal lobe across the superior and middle temporal gyrus. The Partners Human Research Committee reviewed and approved the IRB protocol at Brigham and Women’s Hospital.

S2 read visual words, repeated auditory words, and named visual pictures. S3 saw a 3-letter string (GUH, SEE) and then heard an auditory 2-phoneme combination, making a decision whether the visual and auditory stimuli matched. Interspersed were visual control trials in which a false font was followed by a real auditory stimulus and auditory control trials in which a real letter string was followed by a 6-band noise-vocoded 2-phoneme combination.

We used our clinic compatible, open source electrophysiology (ephys) system based on Intan technology (Los Angeles, CA) to record acutely during neurosurgery. The details of the system have been published (Hermiz et al., 2016) and the design files and software are freely available on https://github.com/TNEL-UCSD/nacq and is briefly discussed below.

The system is capable of recording 256 channels at 20 kHz and features 5 kV RMS power isolation. The purpose of an isolator is to protect the patient from hardware malfunctions and/or power surges. The system consists of an adapter, amplifier & digitizer (Intan RHD2164), power isolator and USB buffering board (RHD2000). The adapter has switches, which can connect a subset of electrodes to reference (REF) or ground (GND). Typically, 2 macrodots are connected to REF while GND is connected to an external needle probe (The Electrode Store, Buckley, WA) that is inserted in the scalp near the craniotomy. The signals are then amplified and digitized by the RHD2164, passed through the power isolator, then buffered and sent via USB to a laptop.

Since ephys components are within several feet of the surgical site, these components were sterilized via standard methods at each of the participating hospitals. The adapter and RHD2164 were sterilized using an electronics friendly process called Sterrad. Sterrad is a low temperature sterilization method that uses hydrogen peroxide plasma to eliminate microbes. We found that there were no obvious effects to the hardware the first three to five sterilization runs.

The clinical recording system is an Xltek 128 channels (Natus Neurology, Pleasanton, CA). For patients S1-S3, the sampling frequency is 500 Hz (70 Hz cutoff) and for S4, it is 250 Hz (83.33 Hz cutoff). Clinical signals are referenced using a bi-polar configuration, which enhances signal differences between recording channels. On the other hand, research electrodes were measured with a uni-polar configuration which results in measuring signals with less differences.

3.2.1.2. Analysis & Statistical Methods

The following software and toolboxes were used: MATLAB, EEGLAB and the Fieldtrip, Chronux toolboxes.

In Figure 3-4, power spectral densities were estimated using Welch's method (pwelch) using a Kaiser Window of length 0.75 seconds with β=4. An entire time period of 10 seconds was used with 50% between windows. Confidence intervals (c.i.) were computed by pwelch and the expression for c.i. is equation 5.3.64 from Statistical and Adaptive Signal Processing: Spectral Estimation, Signal Modeling, Adaptive Filtering and Array Processing (Manolakis et al., 2000). The time-frequency plot was generated using short-time Fourier transform method with Slepian tapers (mtspecgramc from the Chronux toolbox) (Mitra and Bokil, 2009). The moving window is of length 400 msec and step 40 msec. A time-bandwidth product of 5 and 5 tapers were used. The power was converted to units of dB then z-scored across to highlight temporal dynamics. Figure 3-5 uses the same method to compute PSDs as Figure 3. The only difference is that a time period of 20 seconds was used.

For the analysis in Figure 5, the data was low-pass filtered at 400Hz and then downsampled to 1000 Hz. To remove noise, the average signal of the microdot electrodes was subtracted from each channel (average re-reference) and each channel was then bandstopped around line noise and its harmonics. Next, the data was epoched to the onset of stimulus presentation (visual word/picture/auditory word onset for S2, visual word onset for S3) and for each trial the baseline from -300ms-to-0ms was subtracted. Trials judged to have artifactually high amplitude or variances were removed from the dataset. To investigate differences between stimulus classes in the high-frequency band, amplitude was obtained using a 4th-order Butterworth bandpass filter from 70-170Hz and then taking the analytic amplitude from the Hilbert transform and smoothed with a moving window. ANOVAs were run between stimuli classes and corrected for multiple comparisons with false-discovery rate (Benjamini and Hochberg, 1995). S2 had 60 trials for each condition (visual word, auditory word, visual picture). S3 had 157 trials for the human voice and 80 trials for noise-vocoded stimulus. For the time-frequency plots, epochs were transformed from the time domain to the time–frequency domain using the complex Morlet wavelet transform. For the HFB frequencies, constant temporal and frequency resolution across target frequencies were obtained by adjusting the wavelet widths according to the target frequency. The wavelet widths increase linearly from 14 to 38 resulting in a constant temporal resolution of 16 ms.

3.2.2. Results

Having shown the favorable characteristics of our PEDOT:PSS electrodes compared to Pt electrodes, next we assessed our electrodes' ability to measure human electrophysiological activity. We performed intraoperative recordings in both anesthetized patients and patients undergoing clinical mapping of eloquent cortex during epilepsy and tumor resection surgery. The recordings reported consist of testing with four individuals: three at UC San Diego (UCSD) Thornton Hospital (La Jolla, CA) and one at Brigham and Women's (BW) Hospital (Boston, MA). At UCSD, we performed recordings using PEDOT:PSS from Subject 1 (S1) both while awake and while unconscious, and from Subjects 2 and 3 (S2 & S3) while performing a cognitive task. At BW, Subject 4 (S4) was unconscious during the recordings.

As an initial analysis, we demonstrate that PEDOT record comparable activity to current clinical electrodes (Figure 3-4). Here we compare electrophysiology from the macrodot Pt (clinical electrodes), versus the macrodot and microdot PEDOT:PSS electrodes during two different states

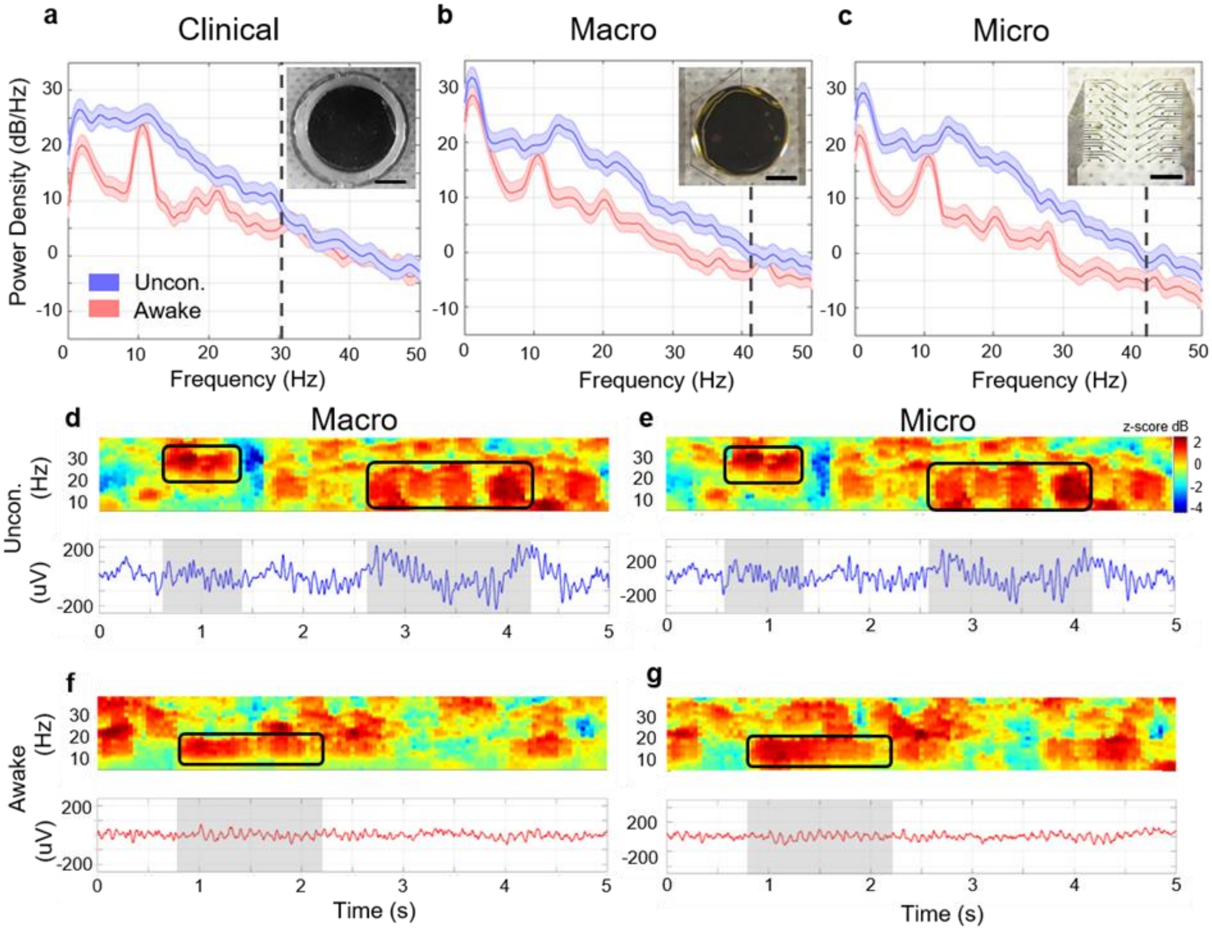

Figure 3-4: Awake vs Unconscious ECoG differences in clinical, PEDOT macro and micro electrodes. Power spectral densities (PSD) between the two conditions (awake vs unconscious) for (a) clinical electrode, (b) PEDOT macro and (c) microdot. Inset of (a) shows optical image of clinical Pt macrodot and (b), (c) show optical image of PEDOT:PSS macrodot and an array of 56 microdots (scale bars 1 mm). The dark blue and red lines are average PSD estimates from overlapping time windows and the lightly colored shaded regions are the 95% c.i. (see methods). The two conditions are deemed significantly different from each other at a particular frequency if c.i. bands do not overlap. The dashed black line at 30, 42 and 44 Hz for a-c mark the frequency at which the PSD difference between the two conditions start to become insignificant for frequencies > 15 Hz. Time-frequency and corresponding time series are shown for a sample 5 sec window for the awake (d and e) and unconscious condition (f and g). The rectangles highlight increases in beta (20 - 30 Hz) and spindling activity (12 - 17 Hz). Color axis represents standard deviations away from the mean for each frequency. The time window per condition for macro and micro are nearly identical.

for S1 when the electrodes were implanted on the anterior superior temporal gyrus. The first state is awake and is engaged in an audio-visual task (see methods for details) versus the second state of anesthesia with Propofol and Dexmedetomidine. As expected there were readily observable differences in electrophysiological recordings between the two states as illustrated in power spectral densities (PSD) (Figure 3-4a-c), time-frequency plots and time series (Figure 3-4d-g).

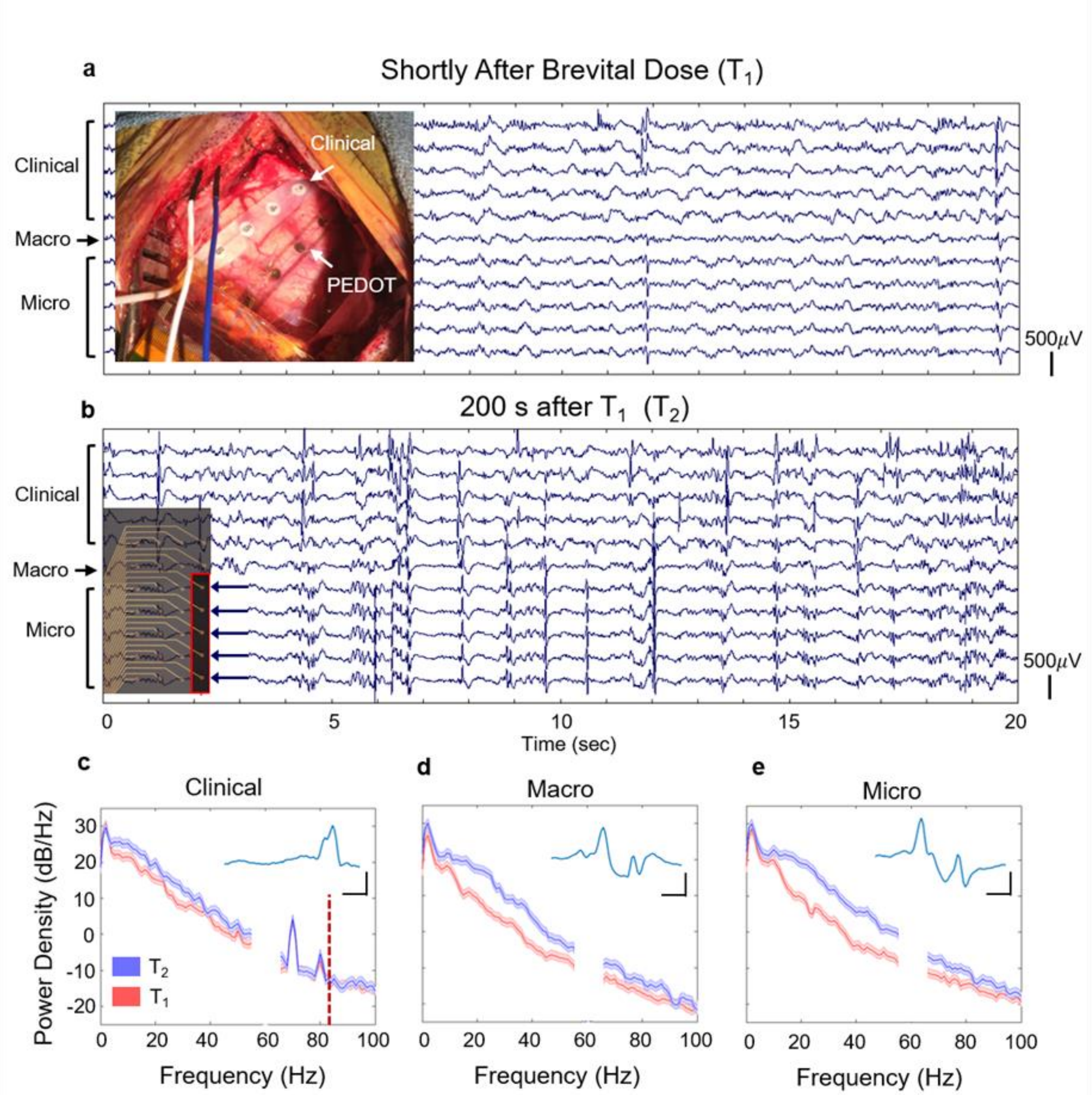

Figure 3-5: Methohexital induced differences in clinical, PEDOT macro and micro electrodes. (a) Simultaneously captured ECoG traces from clinical, PEDOT macro and micro electrodes shortly after Methohexital dose (T1) and (b) 200 seconds after T1, (T2). Inset in (a) shows the clinical and PEDOT ECoG probes implanted over the superior and middle temporal gyrus. Inset in (b) shows which micro-electrodes are plotted for a-b. Power spectral densities of a (c) clinical, (d) macro and (e) micro electrode taken from T1 (red) and T2 (blue). The dark blue and red lines are average PSD estimates from overlapping time windows and the lightly colored shaded regions are the 95% c.i. (see methods). The two conditions are deemed significantly different from each other at a particular frequency if c.i. bands do not overlap. The dashed red vertical line in (c) indicates the upper passband cutoff frequency for the clinical system. Insets from (c-e) show an interictal epileptic discharge (IED) captured concurrently across the three electrode types. Scale bars are 200 µV (vertical) and 50 ms (horizontal).

There is markedly higher power in the anesthetized condition and in particular in the 12 – 17 Hz range, indicative of spindle-like activity (Figure 3-4a-c). Spindling has been reported in deeply anesthetized patients under the drug Dexmedetomidine (Huupponen et al., 2008). Time-frequency plots also appear to show spindling and other dynamic neural activity (Figure 3-4d,e). Clinical ECoG using standard of care electrodes (3 mm Pt) were recorded alongside PEDOT ECoG. A PSD of a clinical electrode shows comparable effects to those measured by the PEDOT electrodes: (1) increased power during the anesthetized condition and (2) a prominent peak around the alpha range for the task condition. However, there are differences between the clinical and PEDOT electrodes in terms of the differential power of the two conditions. The PSDs are significantly different from each other based on their 95 % confidence interval (c.i.) up to 30 Hz and 42 and 44 Hz, for a clinical, macro and micro electrode, respectively (Figure 3a-c). This suggests that PEDOT electrodes are more sensitive at sensing neural activity which is consistent with previously reported EIS (Ganji et al., 2017b). This demonstrates that physiologically expected effects observed in the clinical ECoG are also seen in micro PEDOT electrodes and that they may be sensed with higher fidelity.

Another example of consistent physiological effects observed across electrode types is shown in Figure 4. S4 was undergoing a standard non-dominant temporal lobe resection. Prior to removal, clinical and PEDOT electrodes were placed on the lateral surface of the temporal lobe across the superior and middle temporal gyrus. After recording under usual anesthetic conditions, a dose of Methohexital (Brevital) was administrated with the intention of increasing epileptiform activity (Kofke et al., 1997; Wyler et al., 1987). As expected, this caused a significant increase in epileptiform activity after several minutes as illustrated in the time traces across the electrode types (Figure 3-5a,b). The time traces are taken over two windows: T1 which was shortly after the Methohexital (Brevital) dose and T2 which occurred 200 s after T1. PSDs for T1 and T2 are plotted

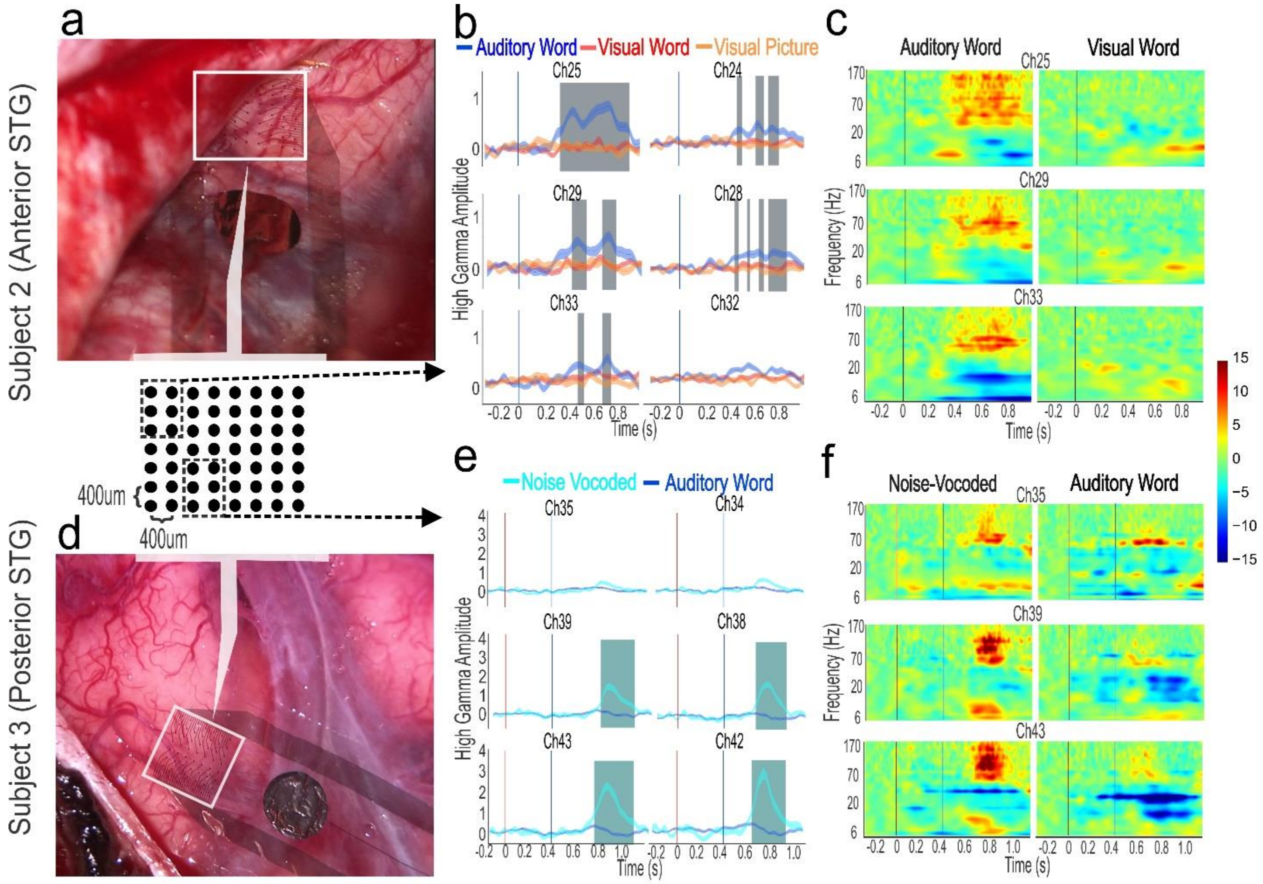

Figure 3-6: Neural activity varies across distances as small 400um (a & d) Electrode placement from the two subjects who performed cognitive tasks. Activity from six neighboring electrodes (3x2 electrodes) from the 8x7 electrode array are displayed to illustrate high-frequency amplitude variation. The white box highlights device placement (device partially obscured in subject 1 by the dural flap). (b & e) High-frequency amplitude for the 3x2 channels confirming significant differences in Hilbert analytic amplitude from 70-170Hz between stimuli classes (shaded regions are anova fdr-corrected significant differences). For subject 1, the blue line indicates stimulus onset. For subject two, the red line indicates visual stimuli onset (to which no response was found across the electrodes) and blue line indicates auditory stimulus onset. Shaded error bars are standard error of the mean for each stimulus condition. (c & f) Time-frequency plots from three of the example channels (3x1) in response to different stimuli classes demonstrating strong differences in higher frequencies. Displayed is trial-averaged power determined by wavelets.

for clinical, PEDOT macro and micro (Figure 3-5c-e, respectively) showing the same trend: more activity in T2. Additionally, there is a larger power difference measured by the PEDOT electrodes than the clinical electrodes again indicating that they are more sensitive to higher frequency (> 15 Hz) neural activity. Insets of Figure 3-5c-e show snippets of an interictal epileptic discharge (IED) that occurred concurrently across the electrodes with different waveform morphologies. PEDOT electrodes showed a larger increase from baseline power due to Methohexital (Brevital) demonstrating their potential clinical utility.

To further examine spatial specificity, we analyzed stimulus-locked cognitive activity in two patients. Recordings were made from the anterior superior temporal gyrus for S2 (Figure 3-6a) and from the posterior superior temporal gyrus for S3 (Figure 3-6d) while each was awake for the clinical mapping of eloquent cortex. While awake, each also performed a short task (see methods). S2 verbally responded on >95% of naming trials and S3 made a correct match/mismatch decision on 98% of trials.

Spectrograms demonstrated increases in high-frequency power specific to certain stimuli classes: auditory words for S2 (Figure 3-6c) and noise-vocoded stimuli for S3 (Figure 3-5f)(Souza and Rosen, 2009). The most consistent difference across electrodes was in the frequency ranges commonly referred to as 'high-gamma', here defined as 70-170Hz (Figure 3-5c,f show the responses for 3 neighboring example channels from each subject). This high-frequency band amplitude (HFB) is highly correlated with population neuronal firing rates (Supratim Ray et al., 2008). To better assess this HFB response, we looked at the response averages across electrodes.

Of the 56 micro-contacts, 42 in S2 and 34 in S3 were functional, as determined by impedance < 60,000 ohms. While reference autoclave experiments here and in (Uguz et al., 2016) showed negligible influence on the microarray impedances (Ganji et al., 2017b), some of the microarray dots displayed higher impedances after transportation and autoclave by hospital personnel as determined by impedance measurements just prior to the recordings. In S2, 16 of 42 good electrodes demonstrated a significant ($p<0.05$ false-discovery rate corrected) increase to auditory words relative to visual words and pictures (38% of electrodes). In S3, 31 of 34 electrodes demonstrated a significant increase ($p<0.05$ false-discovery rate corrected) to auditory noise-vocoded trials relative to human voice trials (91% of electrodes). S3 also saw a visual bigram prior to the auditory stimulus, but showed no significant response across electrodes to visual stimuli. Figure 3-5b,e show the HFB of the six example electrodes chosen from a 3x2 portion of the grid, demonstrating that the presence of an effect and the variability of the effect size can vary across distances as small as (400µm).

3.2.3. Discussion

Here we report the fabrication of a highly reproducible, high-yield PEDOT:PSS microarray, demonstrate PEDOT:PSS possesses superior impedance characteristics compared to Pt clinical electrodes, and show the first PEDOT:PSS recorded stimulus-locked human cognitive activity. A variety of structural studies confirm PEDOT:PSS is safe for implantation and our microarray had a high yield of functional microelectrodes (>96% functional) with a very narrow distribution of impedances. Microelectrodes measured similar electrophysiological phenomena as macrodots made of either PEDOT:PSS or Pt across anesthetized, awake, and pathological states despite the microelectrode's 4 orders of magnitude smaller area. PEDOT electrodes exhibited larger differential power among various conditions (Figure 3-4 and Figure 3-5) than clinical electrodes indicating they have more sensitivity. Finally, we demonstrated that the PEDOT:PSS microelectrode array was capable of resolving differences in cognitive responses across cortical tissue over distances as small as 400µm.

In other cases, PEDOT micro-electrodes recorded highly similar signals as compared to the clinical electrodes as shown in Figure 4a and 4b. This can partly be attributed to referencing schemes (see methods), but is undoubtedly a result of sensing signals much closer to each other (400µm – 3mm vs 1 –5 cm) (Bundy et al., 2014; Slutzky et al., 2010). Measuring highly similar signals has advantages and disadvantages, which change depending on use case. An advantage for measuring highly similar or redundant signals is that they may help denoise a collective signal or feature when combined intelligently. For example, interictal epileptic discharges, IEDs, are difficult to detect using automated algorithms and even challenging for trained electrophyiologists. IED detection might be improved if there were multiple redundant views of the signal which could increase detection confidence. This concept has been used by electrophysiologists to better detect action potentials from single units (eg. tetrode designs). This potential motivates investigation of high density or mixed density surface probe designs, even if sensed signals appear to be highly similar (Slutzky et al., 2010).

As electrode development pushes towards decreasing contact size to increase spatial specificity, PEDOT:PSS contacts facilitate high SNR recordings and have a number of favorable characteristics. The spin-casting approach used in our fabrication provides a consistent electrochemical interface and insignificant morphological changes post-sterilization (Uguz et al., 2016). This approach leads to a very high yield of functioning electrodes (>96%) with a narrow range of impedances. The EIS impedances for PEDOT:PSS are smaller than those for Pt which in turn results in lower noise power spectral density than those of Pt (Ganji et al., 2017b). This difference is significant because cognitive processes that are generally observed at low frequencies (theta, gamma, and low frequency oscillations) need to be measured with the lowest possible electrode noise. Additionally, important information about neuronal firing in the high-frequency bands has a very low amplitude, making it critical to maximize SNR.

Combining these reliably low impedances with several other favorable characteristics makes PEDOT:PSS a strong contender for leading the next generation of neural electrochemical interfaces. These additional characteristics include high charge injection capacity (safe/efficient stimulation) (Cogan, 2008; Merrill et al., 2005; Vadim S. Polikov et al., 2005), compliant mechanical properties for mimicking the curvilinear brain tissue and to compensate brain micromotion in order to reduce tissue damage (Abidian and Martin, 2009; Cogan et al., 2016; Green et al., 2012), and enhanced biocompatible electrode/tissue interfaces to minimize biofouling (Hatsopoulos and Donoghue, 2009; Vetter et al., 2004; Vodovotz et al., 2006). With higher channel counts being achievable via passive wiring or active multiplexing, PEDOT:PSS presents a great opportunity to achieve high-density, high-SNR arrays, with greatly increased spatial specificity.

Despite the promise of PEDOT:PSS for neural recording, we are only aware of one group which displayed human neural recordings from a PEDOT:PSS device (Khodagholy et al., 2016, 2014). They demonstrated that PEDOT:PSS electrodes with an area of 10 x 10 μm^2 can sense a wide variety of neurophysiological activity including low frequency oscillations (beta, delta and spindle activity) and high frequency action potentials. They validated these neurophysiological signals by showing they are modulated by other neurophysiological signals and coarse conditions such as awake or under a variety of anesthesia, similar to our results in Figure 3-4. However, they have not demonstrated how the sensed neurophysiology is modulated by sensory stimulus or cognitive processing, which is one of the main contributions of this work. Interestingly, we did not detect action potentials, which may have been caused by excessive CSF between the pial surface and probe, which acts as a spatial low pass filter. In (Khodagholy et al., 2016), they suggest adding openings homogenously throughout the probe to allow CSF to flow over the probe as well as minimizing the amount of CSF near the probe (Khodagholy et al., 2016). Additionally, the device presented in our study has a larger electrode size (50 μm diameter vs 10 μm diameter), which may have prevented the electrodes from sensing action potentials. Finally, the neurogrid device makes use of a tetrode-like design, concentrating 4 electrodes every 2000μm as opposed to our grid placing 1 electrode every 400µm. Future studies will need to determine optimal electrode design, which will undoubtedly vary for different clinical and experimental questions.

Finally, we examined the ability of PEDOT:PSS microgrid arrays to measure stimulus-locked cognitive responses to audiovisual stimuli. Neural responses to stimuli showed increases in power in high frequencies, likely related to neuronal firing (S. Ray et al., 2008). These increases proved to reliably discriminate different stimuli, both between language modalities (S2) and within a single language modality (S3). Further, the high-frequency amplitude and effects differed within a displacement of 400 µm, demonstrating the great spatial specificity possible with PEDOT:PSS micro-electrodes.

The utility of high-density, high-SNR arrays with high spatial resolution is straightforward within the context of basic science. PEDOT:PSS micro-arrays can extend the ability of intracranial research to identify precisely the borders of functional regions and tease apart the information processing micro-circuitry operations within these regions. Perhaps more important is the great potential for PEDOT:PSS clinical applications as well and the potential for higher SNR and higher spatial resolution ECoG to improve patient outcomes for surgical brain resections. The current gold standard for sparing eloquent, motor, and sensory cortex during resections is direct cortical stimulation to map brain function. In addition to this gold standard, recent work demonstrates the potential use of recorded HFB activity as a complementary method for functional mapping (Darvas et al., 2010). The surgeon often faces a very difficult tradeoff of maximizing resection extent to remove pathological tissue and thus improve the patient's health, while preserving as much function as possible. The coarse spacing, limited channel count, and non-conformability of the currently used electrode substrate constrain the resolution of the information available to make a decision about this tradeoff. PEDOT:PSS electrodes provide safe and efficient stimulation in addition to their high-SNR recording ability and conformable characteristics. Using future arrays combining the excellent stimulation and recording capabilities of PEDOT:PSS, neurosurgeons would be more confident in the functional boundaries of the exposed cortex, and thus be able to make a more informed decision of which tissue to resect. Development of these arrays is facilitated by the fact that PEDOT:PSS electrode fabrication allows quickly iterated designs. Eventually, working together, surgeons and researchers will be able to develop arrays that are effective for optimizing post-surgical outcomes (Abidian et al., 2010; Cui et al., 2001; Green et al., 2008; Heim et al., 2012; Kim et al., 2010; Park et al., 2010; Rivnay et al., 2016).

This chapter, in part, has been adapted from material as it appears in Advanced Functional Materials 2017, "Development and Translation of PEDOT:PSS Microelectrodes for Intraoperative Monitoring" Ganji M*, Kaestner E*, Hermiz J*, Rogers N, Tanaka A, Cleary D, Lee SH, Snider J, Halgren M, Cosgrove GR, Carter B, Barba D, Uguz I, Malliaras G, Cash S, Gilja V, Halgren E, Dayeh S. This chapter, in part, has been adapted from material that is in preparation for submission titled "Stimulus Drive Single Unit Activity from Micro-ECoG" Hermiz J*, Hossain L*, Arneodo Z*, Ganji M, Rogers N, Vahidi N, Halgren E, Gentner T, Gilja V, Dayeh S.

Chapter 4.

Enhanced Neural State Estimation

In the previous chapter, I relied on known neural signals to validate micro-ECoG and compared these signals to those capture on conventional electrodes. In Chapter 4, I will take another approach to validate micro-ECoG. The central question of this chapter is what is the value of high-density micro-ECoG? To answer this question several strategies, which utilized machine learning techniques are taken. First an idealized theoretical model of the spatial extent of neural signal and noise is developed. By sampling space in different ways, I investigate how the spatial parameters of the neural signal affect decoding discrete neural states. Second, I employ this sub-sampling strategy on empirical data (high-gamma activity) from human subjects to determine if 400 μm pitch grids can outperform sub-sampled virtual grids with 800 μm or 1200 μm spacing.

4.1. Introduction

A major question raised in the advancement of μECoG technology is, “How dense should surface grids be?” There is likely no universal answer to this question, since relevant parameters are application dependent and, in particular, the spatial characteristics of neural activity could vary between cortical regions and functional settings. Previous simulation and empirical studies have used spatial spectral techniques to estimate the ideal spacing to be 1.25mm (Freeman et al., 2000; Slutzky et al., 2010). Other empirical works have quantified spatial characteristics by using similarity metrics such as channel correlation vs channel distance (Chang, 2015; Insanally et al., 2016; Kellis et al., 2016; Muller et al., 2016b; Trumpis et al., 2017a) with the interpretation that steeper falloffs indicate that high density grids are advantageous. However, a well-defined functional interpretation of these falloff curves has not been established. In this work, we develop

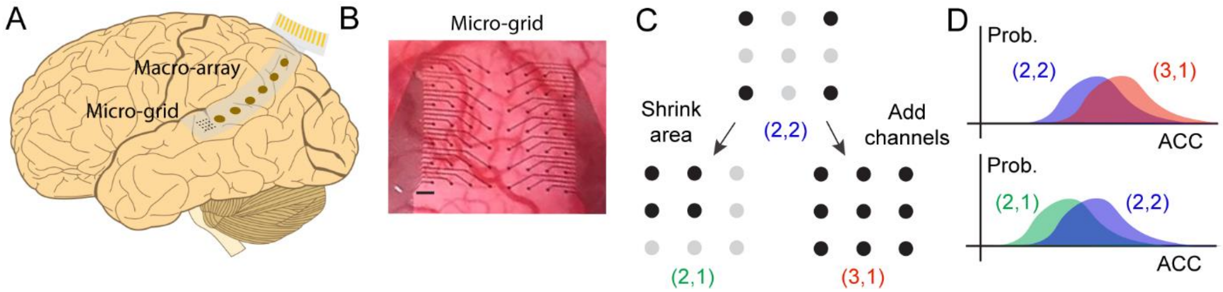

Figure 4-1: High density, µECoG assessment. (A) Sketch of the surface probe used in this work which can record both µECoG (56 electrodes) and ECoG (6 electrodes). Note the actual µECoG is smaller than depicted. The yellow strips indicate the only other exposed conductive region, in which a conductive film will be bonded for interfacing with the device. B) Picture of implanted µECoG probe used in this work, which was manufactured using micro/nano-fabrication techniques. The electrodes are arranged is a 7x8 grid with a pitch of 400µm, a diameter of 50µm, and coated with PEDOT:PSS. The scale bar is 400µm. (C) Drawing depicting two ways to increase electrode density: shrink area or add more channels for a given area. By sub-sampling electrodes from the grid, we can determine if increasing density can be beneficial. The notation (2,2), for example, means a 2x2 grid with twice the pitch spacing. The benefit is defined to be higher decoding accuracy of audio-visual stimuli presented to the subject. (D) Sketch comparing hypothetical distribution of accuracies from different probability densities with the same area (top) and different spacing with fixed channel count (bottom).

an illustrative model to gain an intuition for how spatial signal and noise properties affect the performance gap between high and low density grids from a machine learning perspective. Furthermore, we apply this perspective to examine sub-millimeter pitch grid recordings from the human cortical surface.

Typical adult clinical ECoG probes have an interelectrode spacings (“pitch”) of 1cm, and research grids with pitches as low as 30µm have been used intraoperatively (i.e. Neurogrid) (Chang, 2015; Khodagholy et al., 2016, 2014). Previous electrophysiology studies demonstrated that grids with pitches below 1cm capture richer electrophysiology, and a number of research studies employ “HD-ECoG” grids with 3-4mm pitch that are manufactured by the same companies with the same processes and materials as standard adult clinical grids (Chang, 2015; Flinker et al., 2011; Flint et al., 2017; Wang et al., 2016). However, the anatomic organization of cortex motivates the exploration of higher resolution probes. Anatomically, much of the cortex seems to be organized into mini-columns with a diameter of ~50µ, and functional columns have been identified in various sensory and motor systems with varying diameters, often ~ 400µ (Horton and

Adams, 2005; Rockland, 2010). However, there is great variability across species and areas, and in particular columns have never been demonstrated in human associative cortex (Horton and Adams, 2005; Rockland, 2010). Previous works have demonstrated sub-mm probes can capture novel electrophysiological detail on micro-meter scale (Ganji et al., 2017b; Kaiju et al., 2017; Khodagholy et al., 2016, 2014; Viventi et al., 2011). In human studies of sub-millimeter pitch ECoG grids, recorded signals are evaluated using measures of electrophysiological signal similarity (e.g. correlation, coherence) (Insanally et al., 2016; Kellis et al., 2016; Leah Muller et al., 2016b; Trumpis et al., 2017a). While these measures provide insight into potential utility of higher density recordings, they do not provide a direct connection into the potential of higher spatial resolution devices to more accurately estimate neural state. Evaluating changes in functionally relevant neural states is crucial both for basic neurophysiology studies and for the development of neural prosthetic devices. Although neural state is an abstract concept, we can consider a concrete instantiation of neural state by utilizing cognitive tasks to drive areas of interest towards different states (eg. hearing human voice vs noise). Then we apply machine learning algorithms to evaluate if the additional views of neural state provided by higher resolution recording improves our ability to classify task conditions from neural activity alone. In this work, we compare the classification accuracy of 400μm, 800μm, and 1200μm pitch grids from two subjects. Intraoperative recordings were made with a 400μm grid and has electrodes arranged in a 7x8 grid with an electrode diameter of 50μm (Figure 4-1B). The electrodes were coated with PEDOT:PSS, which facilitates higher signal to noise ratio recording from small area electrodes than conventional metal electrodes (Ganji et al., 2017b; Khodagholy et al., 2011). Subjects were engaged in audio-visual tasks, where multiple classes of time-locked stimuli were presented and classified based on neural signal features. We generated 800μm, and 1200μm pitch “virtual” grids by sub-sampling the 7x8 grid similar to Muller et al, who suggests that 2mm can outperform 4mm and 8mm grids (Leah Muller et al., 2016a). In this work, we evaluate grids with 25x the density of this previous study while also adding controls for channel count and coverage area (Figure 4-1C). Similar work was also performed in rats with 200µm pitch grid (Ledochowitsch et al., 2013) and in monkey with 700µm pitch grid (Kaiju et al., 2017), albeit with differing analyses that may not directly translate to humans. Here, we show that 400µm spaced grids can significantly outperform 800µm and 1200µm when controlling for coverage area.

4.2. Methods

4.2.1. Modeling

Table 4-1: Commonly used symbols

Symbol	**Description**	**Symbol**	**Description**
σ_S	characteristic length for signal	$\boldsymbol{s}$	signal across channels
λ	characteristic length for noise	$\boldsymbol{\Sigma}$	channel co-variance matrix
a	signal amplitude for center channel	d^2_m	squared Mahalanobis distance
$\boldsymbol{x}$	measurements across channels	Δ	difference in squared Mahal. distance

4.2.1.1. Description

To explore when higher density grids might outperform (or underperform) comparable lower density grids, a model was developed and studied under various circumstances. Let $\boldsymbol{x}$ be a d-dimensional measurement or feature vector of real numbers, where d is the channel count. In general, $\boldsymbol{x}$ is assumed to include signal and additive noise.

$$\boldsymbol{x} = \boldsymbol{s} + \boldsymbol{n} \tag{1}$$

Two conditional random variables are defined $\boldsymbol{x_p} = \boldsymbol{x}|c = p$ and $\boldsymbol{x_{np}} = \boldsymbol{x}|c = np$, where c denotes the class a particular feature vector belongs to: p (preferred stimuli) or np (non-preferred stimuli). We will assume only the preferred stimuli has signal. Previous studies have shown that correlation between raw channels measurements and features derived from various frequency bands can fit reasonably well to an exponential decay (Insanally et al., 2016; Kellis et al., 2016; Leah Muller et al., 2016b; Trumpis et al., 2017a). This motivated defining the signal to decay exponentially with respect to Euclidean distance from the peak activation site.

$$s_i = a * \exp\left(-\frac{||r_i - r_{ctr}||}{\sigma_s}\right) \tag{2}$$

Note, r_i is the position of the i^{th} channel and r_{ctr} is the position of the channel with peak (or center) activation. a scales the magnitude of signal and, as will subsequently become evident, is the signal to noise ratio (SNR) for the center channel. σ_s is the characteristic length for the signal, which is when $||r_i - r_{ctr}|| = \sigma_s$ corresponding to a $1/e \approx 0.37$ decrease in the signal. For simplicity, the noise is assumed to be Gaussian with zero mean and unit variance ($\Sigma_{ii} = 1$), $\boldsymbol{n} \sim N(\boldsymbol{0}, \boldsymbol{\Sigma})$; hence, SNR, which is defined to be the mean divided by the standard deviation for the center channel is a. Again, it is assumed that noise covariance decays exponentially as a function of distance. Here, λ is the characteristic length of noise correlation. So, two electrodes that are spaced λ units apart from each other will have a correlation of $1/e \approx 0.37$.

$$\Sigma_{ij} = \exp(-\frac{||r_i - r_j||}{\lambda}) \tag{3}$$

The overall model can be rewritten as

$$\boldsymbol{x_p} \sim N(\boldsymbol{s}, \boldsymbol{\Sigma}) \tag{4}$$

$$\boldsymbol{x_{np}} \sim N(\boldsymbol{0}, \boldsymbol{\Sigma}) \tag{5}$$

4.2.1.2. Analysis

This simple, yet plausible model allows us to explore situations in which higher density grids outperform lower density grids. We are mainly interested in two comparisons: 1) fix area and vary channel count (or equivalently pitch) and 2) fix channel count and vary pitch (or equivalently area). In order to compare grids, we need a metric. Since $\boldsymbol{x_p}$ and $\boldsymbol{x_{np}}$ are drawn from multivariate normal distributions with the same covariance matrix, the natural choice is the Mahalanobis distance, d_m between the means of the distributions.

$$d_m^2 = \boldsymbol{s}^T\boldsymbol{\Sigma}^{-1}\boldsymbol{s} \tag{6}$$

In fact, researchers in related work have used the Mahalanobis distance to score "evoked signal-to-noise ratio" in trials indicating that these assumptions are reasonable (Insanally et al., 2016; Trumpis et al., 2017a). Intuitively, $\underline{d_m}$ is the average separation between feature vectors from the preferred and non-preferred stimuli. The larger the separation, the more discriminable the two classes of data are. What we are interested in is how that separation changes as a function of grid density. That is, the difference or difference squared,

$$\Delta = d_{m,hd}^2 - d_{m,ld}^2 \tag{7}$$

To gain an intuition for when higher density grids have an advantage, we compute analytical expressions for Δ in the two-channel case: 1) the difference between two vs one channel, $\Delta_{2,1}$ and 2) the difference between two channels that are 1 unit apart vs 2 units apart, $\Delta_{2,2'}$.

$$\Delta_{2,1} = \frac{(s_2 - s_1\Sigma_{21})^2}{1 - \Sigma_{21}^2} \tag{8}$$

$$\Delta_{2,2'} = \frac{(s_2 - s_1\Sigma_{21})^2}{(1 - \Sigma_{21}^2)} - \frac{(s_{2'} - s_1\Sigma_{2'1})^2}{\left(1 - \Sigma_{2'1}^2\right)} \tag{9}$$

See supplementary materials for derivation. As is obvious from Eqn 8 and 9, there is a singularity when $\Sigma_{21} = 1$ or $\Sigma_{2'1} = 1$. This occurs because the squared Mahalanobis distance, d_{x_1,x_2}^2 or

$d^2_{x_1,x_2'}$ cannot be computed as $\det(\boldsymbol{\Sigma})$ becomes undefined and $\boldsymbol{\Sigma}$ uninvertible. This likely never occurs in practice as there is always measurement noise that is not perfectly correlated across channels.

4.2.1.3. Time Series

A simple time series extension of the spatial model is described. The measurement vector, $\boldsymbol{x}$ that has d elements for the number of channels becomes a matrix, $\boldsymbol{X}$ that is $d \times T$, where T is number of time samples. Again, we will assume in general that the signal is deterministic and that there is additive noise.

$$\boldsymbol{X} = \boldsymbol{S} + \boldsymbol{N} \tag{10}$$

In the non-preferred condition, $\boldsymbol{S} = \boldsymbol{0}$ and in the preferred condition $\boldsymbol{S} = \boldsymbol{F}$ where $\boldsymbol{F}$ are samples for a set of deterministic functions that evolve over space and time. The rows of $\boldsymbol{F}$ are denoted $\boldsymbol{f_1}, \boldsymbol{f_2}, .. \boldsymbol{f_d}$. As before, the signal on each channel decays exponentially with distance from the center channel, $\boldsymbol{x_{ctr}}$ which we will set to be $\boldsymbol{x_1}$.

$$\boldsymbol{f_j} = \boldsymbol{f_1} \exp\left(\frac{-\left\|r_1 - r_j\right\|}{\sigma_s}\right) \tag{11}$$

The time evolution of $\boldsymbol{f_1}$ is assumed to follow a Gaussian shape where the peak activation occurs at t_{pk}.

$$\boldsymbol{f_1} = a \exp\left(\frac{-\left\|t - t_{pk}\right\|}{\sigma_t}\right) \tag{12}$$

Finally, the noise matrix ***N*** are just *T* copies of the original model's random variable ***n***, so that it's entries across time are independent and identically distributed. Hence, the noise spatial relationship of Eqn 3 still holds.

4.2.2. Probe

The probe used in experiments consists of 56 μECoG and 6 ECoG electrodes. The μECoG electrodes are arranged in a 7x8 grid with a 400μm pitch and an electrode diameter of 50μm. The ECoG electrodes are arranged is a strip or line spaced 1cm apart with an electrode diameter of 3mm. The μECoG were used to record surface potentials while the most of the ECoG electrodes were tied to reference. A stainless steel needle probe was used for ground and was inserted into the scalp at the edge of the craniotomy. The electrodes are coated with an organic conducting polymer called poly(3,4-ethylenedioxythiophene) doped with polystyrene sulfonate (PEDOT:PSS). PEDOT:PSS has been shown to reduce impedance values by orders of magnitude compared to traditional metal electrodes (eg. Pt). The typical electrode impedance magnitude at 1kHz is 13kΩ. Lastly, the substrate is 4-5μm thick parylene which can conform to the surface of the brain. Additional device details can be found in (Ganji et al., 2017b; Uguz et al., 2016). The data acquisition system used is described extensively in (Hermiz et al., 2016) and briefly in Section A.1.

4.2.3. Sub-sampling

The 7x8 grid of electrodes was sub-sampled to obtain "virtual" grids. There are many ways to sub-sample and an exhaustive enumeration of all possible sub-samples is not only intractable, but would be challenging to interpret. Since we are interested in determining if certain grid densities are beneficial we chose to limit all virtual grids to be square as these virtual grids could easily be parameterized and related to electrode density.

Virtual square grids can be parameterized by 3 variables (ignoring electrode size): number of channels, pitch (or spacing), and the area that the grid encompasses. If pitch is normalized to take on integer values (1, 2, …), then we can relate the variables using the following expression: $A = \left(p(\sqrt{c} - 1)\right)^2$, where A, p and c are the area, pitch and number of channels, respectively. We explored the device parameter space by fixing each variable for a given analysis and changing the other degree of freedom: fixed pitch (Figure 4-6), fixed area (Figure 4-7), and fixed channel count (Fig S7). We are primarily interested in comparing virtual devices with fixed area (Figure 4-7).

Since our grid contained bad recording channels, we only considered virtual grids that had at least 50% of the channels they were supposed to have. For example, let's say a 5x5 grid had 13 good recording channels (52%), then the virtual grid would not be thrown out; however, it had 12 good recording channels (48%), then the virtual grid would be thrown out.

In some situations, it might be the case that a grid with 50% good electrodes is compared to a grid with 90% good electrodes, in which case the percentage of good channels confounds the comparison. To ensure there our results were not biased by the confounding variable of percentage of good channels, we performed a meta-analysis where we found the difference in percentage of good channels for all comparisons and determined if the distributions were significantly biased away from 0. We did not find a significant bias for the fixed area comparison, but did find a bias for the fixed channel comparison for SD007 (S-Figure 9). We discuss the interpretation of the fixed channel comparison results in light of this bias in the Discussion and supplementary section.

4.2.4. Machine Learning

Features were computed by summing up the HFB for each channel in non-overlapping windows of 0.25 sec. For SD007, the start and end time were 0.15 and 0.9 sec post stimulus onset and for SD008, the start and end time were 0.5 to 1 sec post stimulus. Elastic-net logistic regression

(ELR) was used to classify presented stimuli types. ELR was used because it is robust to high dimensional datasets and generally yields competitive classification accuracies (Zou and Hastie, 2005). ELR is a regularized version of logistic regression. It uses a combination of ridge (L_2-penalty) and lasso (L_1-penalty) regularization to reduce and eliminate the effect of non-discriminatory features. Ultimately, the result in a linear discriminate that should have few, high magnitude weights. The ELR implementation used was Glmnet Toolbox for Matlab (Qian et al., 2013). The mix of L_1 and L_2 penalty was fixed to be 0.75 and 0.25, while the weight of the regularization penalty was chosen by sweeping through 50 candidate values 12 times (for 12-fold cross validation) and choosing the value that maximizes the average accuracy. Aggregate accuracy statistics are computed from validation sets.

4.2.5. Experimental Task

Subjects SD007 and SD008 undergoing clinical mapping of eloquent cortex provided informed consent to have the probe placed on their pial surface and to participate in a 10-minute task. The μECoG grid was placed on the left superior temporal gyrus (STG): anterior STG for SD007 and posterior STG for SD008. UC San Diego Health Institutional Review Board (IRB) reviewed and approved study protocol.

The preferred and non-preferred categories were assigned by visually inspecting the trial averages of the high frequency band envelope. The category that yielded the largest response was labeled preferred while the category that yielded the smallest or no response was labeled non-preferred.

SD007 read visual words (e.g text of the word ‘lion’), repeated auditory words (eg. audio of the word ‘lion’), and named visual pictures (eg. picture of a ‘lion’). The stimuli that elicited the largest response was the auditory word, therefore it was labeled preferred. Both visual pictures and words yielded little if any response. Visual words were chosen to be in the analysis and were labeled non-preferred. It is expected that the auditory word elicits the largest response since the probe was implanted on STG, which is responsible for auditory processing. There were 60 auditory word trials and 59 visual word trials analyzed in this study.

SD008 saw a 3-letter string (GUH, SEE) and then heard an auditory 2-phoneme combination, making a decision whether the visual and auditory stimuli matched. Interspersed were visual control trials in which a false font was followed by a real auditory stimulus and auditory control trials in which a real letter string was followed by a 6-band noise-vocoded 2-phoneme combination. For SD008, binary classification was performed between noise-vocoded stimuli and human voice. In these recordings, the noise-vocoded stimuli produce a larger response than human voice and therefore the noise-vocoded was labeled preferred while human voice was labeled non-preferred. This is consistent with previous work examining cognitive processing and evoked responses to noise-vocoded and human voice in posterior STG (Travis et al., 2013). There were 68 noise-vocoded trials and 63 human voice trials analyzed in this study.

4.3. Results

Modeling and experimental analyses were performed to determine if and when higher density grids outperform lower density grids. An illustrative model with properties motivated from previous studies (Insanally et al., 2016; Kellis et al., 2016; Leah Muller et al., 2016b; Trumpis et al., 2017a) was developed to determine under what conditions a higher density grid might outperform a lower density grid. Analytical results for the simple 2-channel case and numerical results for higher dimensional cases are presented (Figure 4-2 and Figure 4-3). We then analyze real μECoG recordings acquired from two subjects, SD007 and SD008 engaged in audio-visual tasks in the operating room. Two types of stimuli were classified and classification accuracy served as the performance metric when comparing grids. Sub-sampling the 7x8 grid allowed us to explore the device design space and, in particular, electrode density.

4.3.1. Modeling

We developed a simple model that assumes measurements belong two types of stimuli, preferred, $\boldsymbol{x_p}$ and non-preferred, $\boldsymbol{x_{np}}$ and are generated from multivariate normal (MVN) distributions: $\boldsymbol{x_p} \sim N(\boldsymbol{s}, \boldsymbol{\Sigma})$ and $\boldsymbol{x_{np}} \sim N(\boldsymbol{0}, \boldsymbol{\Sigma})$. The signal of interest, $\boldsymbol{s}$ is assumed to peak at a specific electrode, x_{ctr} and fall off exponentially with a characteristic length, $\sigma_{s.}$ In all analyses, the electrode x_{ctr} is a member of all grids and is the center most electrode. When there is an even number of electrodes, then x_{ctr} is the left center most electrode. Please note that in these simulations, the peak location of the signal is not modeled as randomly related to electrode location, as would be the case in actual recordings. Had our model permitted response peaks between electrodes, then tight electrode spacing would be highly advantageous, inasmuch as it would make it more likely that the response peak would be directly measured. However, for the current work, we only focus on the case where the peak activation is on the grid and is centered. The results from this condition can be viewed as a highly conservative estimate of how advantageous high-density grids are.

Noise correlation is also modeled as a decaying exponential with characteristic length, λ. That is, electrodes closer together will have more correlations whereas channels farther apart will have less. Here, noise can be interpreted as baseline neural activity that is independent of the stimulus.

The assumption that signal and noise decay exponentially across space is supported by existing studies that fit similarity measures of raw and band-limited signals to exponential decay functions with little error (Leah Muller et al., 2016b; Trumpis et al., 2017a). The squared

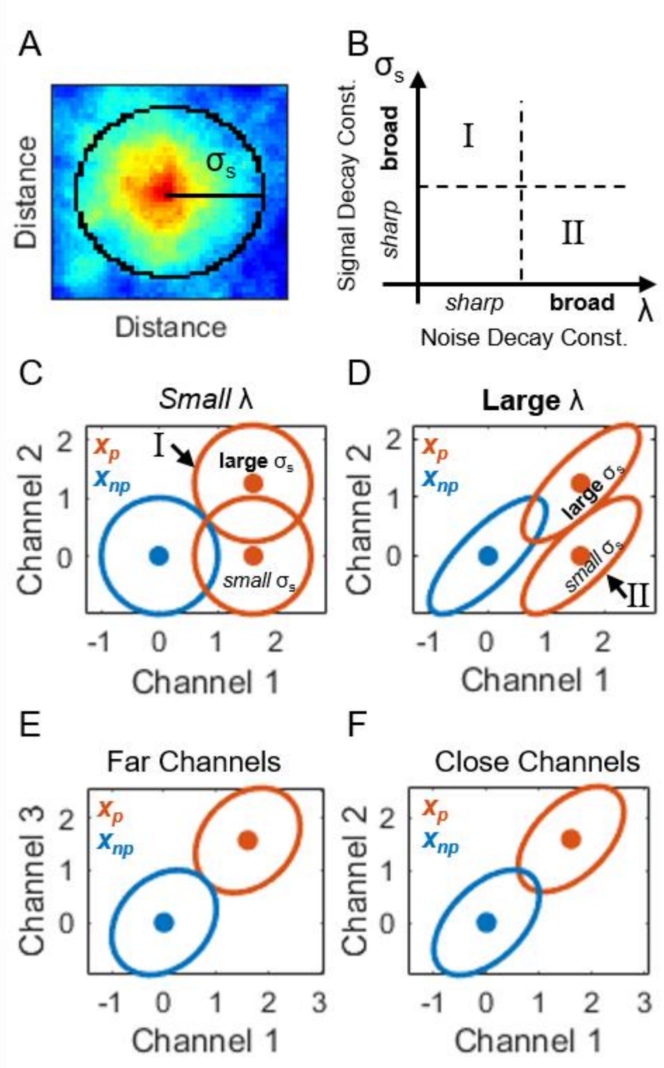

Figure 4-2: Multivariate normal (MVN) model parametrized by decaying exponentials. (A) Spatial representation of signal fall-off length σ_s (arbitrary units) using generated data from the model. Note, that dark red maps to the maximum value and dark blue maps to the minimum value. For more visualizations of signal and noise fall-off length, λ see S-Figure 3(B) Illustration of which regions in the parameter space σ_s - λ where higher density grids outperform lower density grids. There are two regions: I, $\sigma_{s,}$ is large and λ is small or II, σ_s is small and λ is large. (C-F) 2-channel feature space where the MVN for various random variables are plotted – dots are means and the ellipses are 1 standard deviation. The distribution of channel measurements from the non-preferred stimulus, $\boldsymbol{x}_{np}$ are blue and the distribution from the preferred stimulus, $\boldsymbol{x}_p$ are red. (C) Illustrates effect I: given a small λ, a larger σ_s will increase separation between $\boldsymbol{x}_{np}$ and $\boldsymbol{x}_p$. Note small λ corresponds to little correlation and thus a circular distribution. (D) Illustrates effect II: given a large λ, a smaller σ_s will increase separation. Note large λ corresponds to large correlation and thus a skewed distribution along the $y = x$ axis. (E-F) Illustrates when 2 channels spaced far apart (low density) can be better than when spaced close together (high density). In this case, σ_s must be large and λ must be relatively small.

Mahalanobis distance is used to measure the separation between the mean value of $\boldsymbol{x_p}$ and $\boldsymbol{x_{np}}$, $d_m^2 = \boldsymbol{s}\boldsymbol{\Sigma}^{-1}\boldsymbol{s}$ and the difference in the squared Mahalanobis distances of two grid configurations is denoted Δ. Larger absolute Δ values indicates that one grid configuration enables the acquisition of neural signals that better distinguish the preferred and non-preferred stimulus. The sign of Δ indicates which of the two grids is advantageous – by convention, $\Delta>0$ means that higher density is more advantageous.

4.3.1.1. Analytical

To gain intuition for when higher density grids might enhance state estimation, we find analytical expressions for the difference of squared Mahalanobis distances, generally denoted as Δ, in the two-channel case. $\Delta_{2,1}$ is defined as the difference between two vs one channels and $\Delta_{2,2'}$ is the difference between two channels spaced two vs one units apart. The analytical expressions for $\Delta_{2,1}$ and $\Delta_{2,2'}$ are given in Eqn 8 and Eqn 9, respectively. $\Delta_{2,1}$ is never negative since, as expected, there is never an advantage of using only 1 channel vs 2 channels. Another intuitive finding is that the minimum of $\Delta_{2,1}$, which is 0, is reached when the signal is the same on both channels, $s_1 = s_2$ and the noise correlation, Σ_{12} approaches 1 (see supplementary). That is, when the measurements on both channels becomes equal, the value of recording from both channels vs just one vanishes. On the other hand, $\Delta_{2,1}$ and $\Delta_{2,2'}$, are large when either: I) σ_s is large and λ is small II) σ_s is small and λ is large (Figure 4-2B). These effects are illustrated in Figure 4-2C-D. In Figure 4-2C, a sharp fall-off of the characteristic noise length (small λ) results in noise that is almost uncorrelated and isotropic, or equivalently the iso-probability density contour is circular. Depicted in blue and red are the non-preferred, $\boldsymbol{x_{np}}$ and preferred measurements, $\boldsymbol{x_p}$, respectively. In Figure 4-2C, there are two cases in which the preferred measurements are plotted: small (sharp fall-off) and large (broad fall-off) σ_s. When σ_s is small, the preferred measurements will fall close to the x-axis, but when σ_s is large, they will fall towards the $x = y$ line. Larger σ_s results in more separation between non-preferred and preferred points by up to a factor of $\sqrt{2}$. Intuitively, effect I) can be thought of as enhancing SNR by averaging measurements with the same signal, but uncorrelated noise. Effect II is illustrated in Fig 2D. Here, λ is large resulting in high correlation among the channels and thus an oblong iso-probability density contour. Again, measurements where σ_s is small and large are considered. When σ_s is large, the iso-contours representing 1 standard deviation have some overlap; however, when σ_s is small, that overlap is eliminated as the Mahalanobis distance between the non-preferred and preferred points increases (Figure 4-2D). Unlike $\Delta_{2,1}$, $\Delta_{2,2'}$, the difference of the squared Mahalanobis distance between two channels spaced 1 and 2 units apart, can be negative meaning that in some cases there is a disadvantage to having electrodes spaced close together when comparing grids with the same number of electrodes. This can occur if the signal on both channels is almost the same (σ_s is large) and when correlation between channel 1 and 2' decays significantly compared to channel 1 and 2 (λ is about equal to the pitch) (Figure 4-2E-F).

Lastly, SNR scales the advantage or disadvantage of high density electrodes. So, if there is an advantage to higher density as is likely to be the case for $\Delta_{2,1}$, then increasing SNR will enhance that advantage. However, it would also enhance the disadvantage of higher density when $\Delta_{2,2'} < 0$. This can be seen by factoring out a from $\boldsymbol{s}$ in Eqn 6, which shows that $d_m^2 \propto a^2$ and thus $\Delta \propto a^2$. This SNR scaling effect is true for the general d-channel case.

4.3.1.2. Numerical

To determine whether the effects found in the analytical expressions of the 2-channel case generalized to higher dimensional cases, the 25-channel results were numerically computed from Eqn 6. Again, two comparisons were made: 1) fixed area, comparing a 5x5 grid with unit pitch vs a 3x3 grid with twice unit pitch and 2) fixed channel count, comparing a 3x3 grid with unit pitch vs a 3x3 grid with twice unit pitch. The difference in squared Mahalanobis distances for 1) and 2) will be denoted as $\Delta_{5,3'}$ and $\Delta_{3,3'}$, respectively.

As expected, SNR scales the difference in performance $\Delta_{5,3'}$ and $\Delta_{3,3'}$. In Figure 4-3A, both $\Delta_{5,3'}$ and $\Delta_{3,3'} > 0$ for $\sigma_s = 0.5$ and $\lambda = 1$, so increasing SNR increases the difference in squared Mahalanobis distance quadratically. Interestingly, Figure 4-3B shows for $\sigma_s = 10$ and $\lambda = 1$ high density provides an advantage or disadvantage depending the comparison: $\Delta_{5,3'} > 0$ and $\Delta_{3,3'} < 0$. Hence, SNR quadratically increases $\Delta_{5,3'}$ and decreases $\Delta_{3,3'}$. These results follow directly from our analytical findings described in 4.8.1.1.

Consistent with the effects found in the analytical expressions of the 2-channel case, there are two regions in σ_s-λ space where higher density outperforms: I) $\sigma_s < 1$ and $\lambda > 1$ or II) $\sigma_s > 1$ and $\lambda < 1$ for $\Delta_{5,3'}$ and $\lambda < 1/3$ for $\Delta_{3,3'}$ (Figure 4-3C-D). As anticipated from our 2-channel analytical results, there is a region where higher density underperforms when comparing grids with the same channel count, which is roughly $\sigma_s \gg 1$ and $1/2 < \lambda < 2$. Finally, as expected, $\Delta_{5,3'} > 0$ for all computed values in the domain $0.1 \leq \sigma_s, \lambda \leq 10$, or, simply put, the 3x3 grid with twice unit spacing never outperforms the 5x5 grid with 1 unit spacing for all the parameters we used.

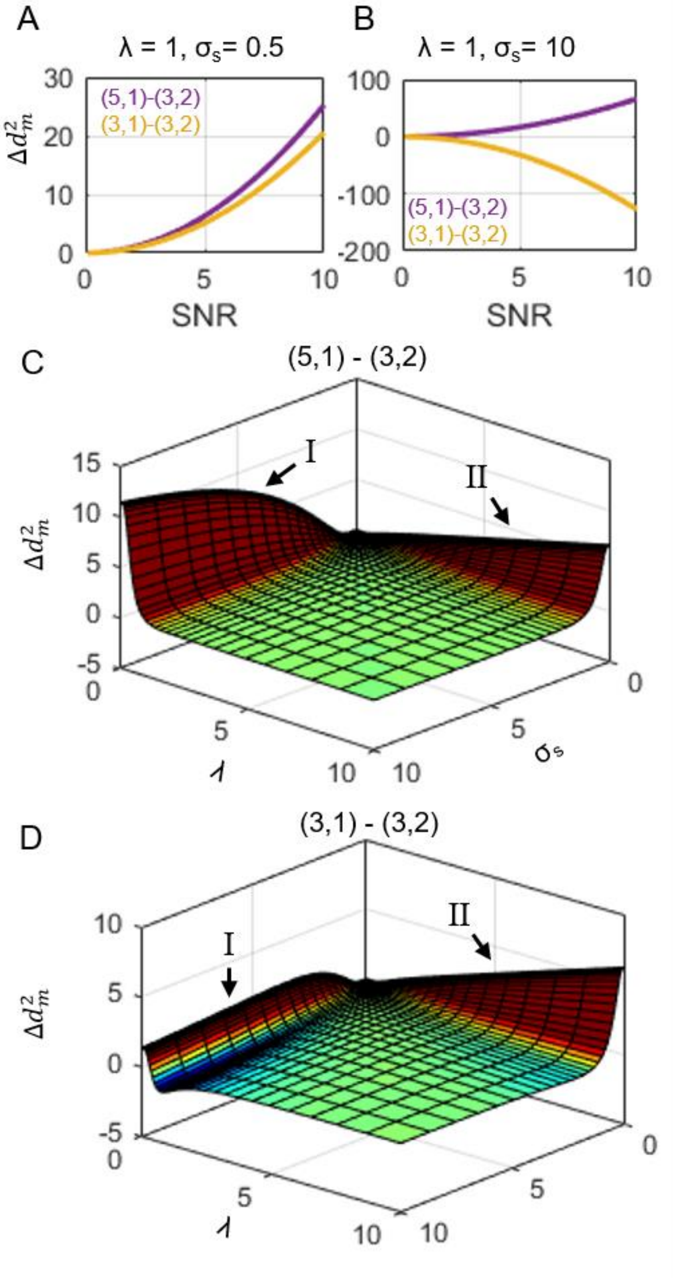

Figure 4-3: (A-D) Numerical results from (5,1) vs (3,2) and (3,1) vs (3,2). The notation (*a*,*b*) refers to a grid that has *a* by *a* channels and has a pitch of *b*. (A-B) As SNR increases, the difference of squared Mahalanobis distance (Δd^2_m) increases or decreases, depending on σ_s, λ and which grids are compared. (C-D) 3d plots showing Δd^2_m for a grid of σ_s and λ values. (C) For (5,1) – (3,2), there are no values for which $\Delta d^2_m < 0$, given the domain; and as expected, $\Delta d^2_m >> 0$, when σ_s, is large and λ is small or vice versa. (D) For (3,1) - (3,2), $\Delta d^2_m < 0$, when roughly, $\sigma_s > 5$ and $1 < \lambda < 2$, which is expected. Again, $\Delta d^2_m >> 0$ when σ_s, is large and λ is small or vice versa. The color axis ranges from -1 (dark blue) to 1 (dark red) and is used to represent sign.

4.3.1.3. Time Series

It is important to note that the presented model has no notion of time, but simple extensions can be made to model time. One extension is to have the signal evolve according to a Gaussian function and assume the noise is independent and identically distributed across time (see Section 4.3.3 for explicit definition). An important statistic often computed from high density recordings is the correlation between two channels vs the distance between those channels. The correlation between the center channel, $\boldsymbol{x_1}$ and any other channel $\boldsymbol{x_j}$ is (see supplementary for derivation)

$$\rho_{x_1 x_j} = \frac{(\Sigma_{1j} + \alpha_j p - \mu_1 \mu_j)}{\sqrt{\Sigma_{11} + p - \mu_1^2}\sqrt{\Sigma_{jj} + \alpha_j^2 p - \mu_j^2}} \tag{13}$$

where $\alpha_j = \exp(\frac{-\|r_1 - r_j\|}{\sigma_s})$, $\Sigma_{1j} = \exp(-\frac{\|r_1 - r_j\|}{\lambda})$, $p = E[\boldsymbol{f_1^2}]$, $\mu_1 = E[\boldsymbol{x_1}]$ and $E[\boldsymbol{x_j}] = \mu_j$. Numerical calculations suggested out that $\rho_{x_1 x_j} \approx \Sigma_{1j}$ when SNR in $\boldsymbol{x_1}$ is not too large (S-Figure 4). That is, if the SNR is not too large, then the channel correlation computed from the time series of this model, will be approximately equal to the entries of the noise covariance matrix. Under these circumstances, we can extend the results of the spatial model to this time series model. This is important because we can interpret commonly computed correlation vs distance plots using our framework.

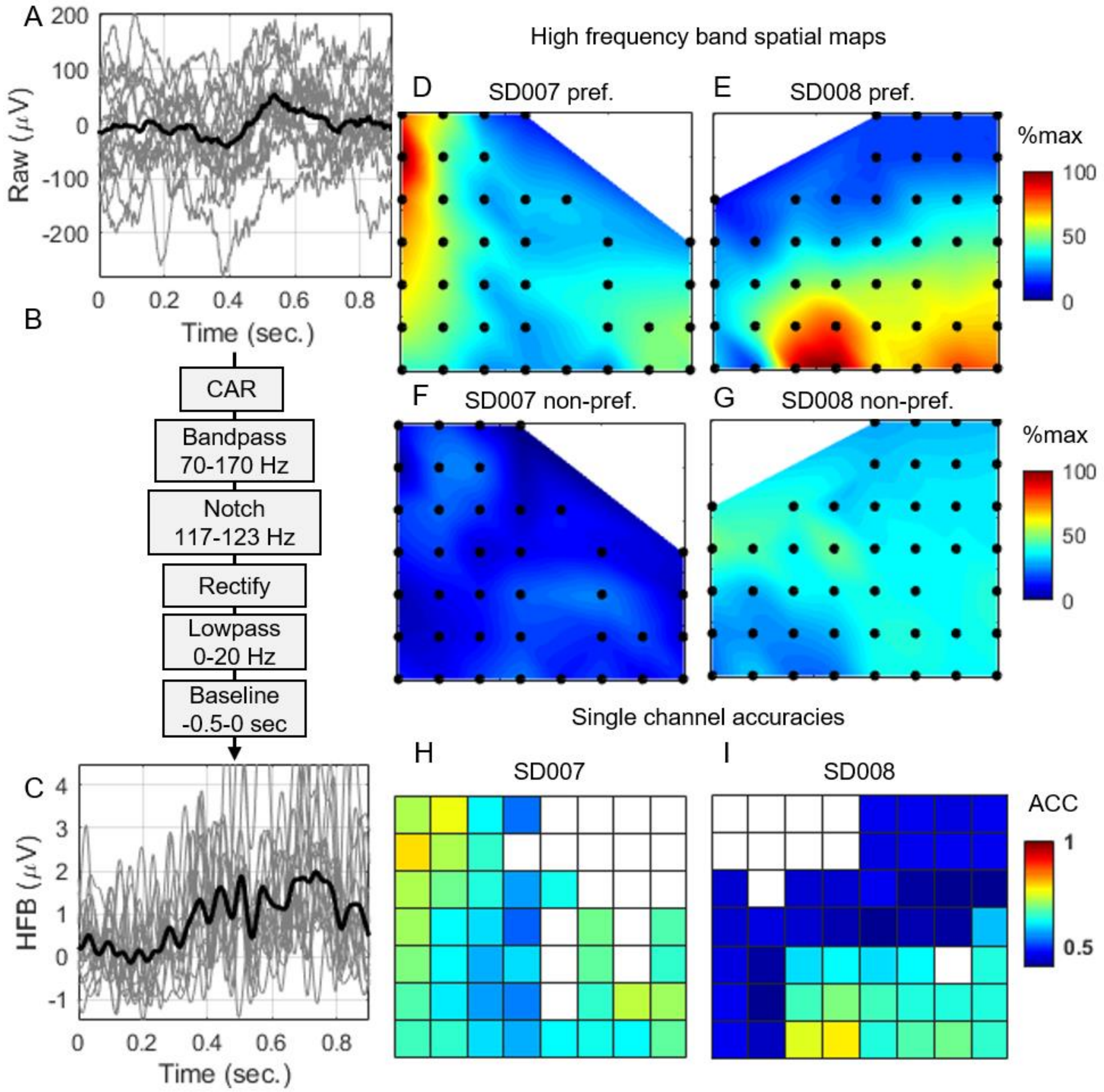

Figure 4-4: Signal processing pipeline. (A) Trials of raw measurements (no post processing) shown in gray and the trial average is shown as black (B) Block diagram of signal processing (C) Trials of high frequency band (HFB) activity shown in gray and the trial average is shown as black. Cubic interpolation across space of peak HFB due to preferred stimuli (D) SD007 and (E) SD008 vs non-preferred stimuli (F) SD007 and (G) SD008. Units are percent of maximum response across stimuli type for each subject. White space could not be interpolated due to lack of channels. Single channel ACC for (H) SD007 and (I) SD008. White squares indicate thrown out channels.

4.3.2. Empirical

Next, we explore the advantages of higher density grids by analyzing real μECoG recordings from two subjects intraoperatively at UC San Diego, Thornton Hospital. The grid has

7x8 micro-electrodes spaced 400μm apart and a diameter of 50μm. These subjects were engaged in an audio-visual task (see Section 4.2). Various types of time locked stimuli were presented to the subjects and stimuli class served as ground truth for offline neural state decoding experiments. For each subject, there were 2 stimulus classes classified: one that produced a marked neural response and one that did not. Rectified high frequency band (70 -170 Hz) amplitude (HFB) was used to measure the neural response because it has been shown to have high spatial specificity and correlation with sensory and cognitive processing (N E Crone et al., 1998; Miller et al., 2007). Figure 4-4 shows how the raw trials were processed to yield HFB (supplementary materials). The trials were then parsed into 0.25 sec windows and summed to compute the features (Section 2.4).

The spatial spread of HFB activation was qualitatively assessed by taking the peak HFB in time and using cubic interpolation across space (Figure 4-4D-G). The plots for each subject are normalized to indicated the percentage of the peak response. For both subjects, there is a clear region where the activation is markedly larger. For SD007, the highly-activated region appears to be confined to a smaller area and the dynamic range is larger than SD008. The preferred and non-preferred stimuli were classified by applying the HFB features to Elastic Net Logistic Regression (ELR) – a classification algorithm robust to high dimensional datasets with a limited number of examples (Qian et al., 2013; Zou and Hastie, 2005) (Section 4.2). The single channel classification accuracy (ACC) results are consistent with the heatmaps of the HFB activation (Figure 4-4H-I). Maximum single channel ACC for SD007 and SD008 is 78% and 77%, respectively. Note, chance performance is 50% since classification is between two labels.

A common technique for removing interference (eg. movement artifact, electromagnetic interference) in EEG/ECoG is common average referencing (CAR), where the average of the raw measurements across all channels is subtracted for each channel (Crone et al., 2001; Ludwig et al., 2009). After applying CAR, the trial averaged HFB for each channel was more prominent and smoother for SD008, while SD007 did not change much suggesting that there was substantial interference for SD008 (S-Figure 5 and S-Figure 6). Re-doing the HFB heatmaps with CAR changed the spatial activation to be more focal and increased the dynamic range for both subjects (Figure 4-5A-D). While the classification results did not change very much for SD007, SD008 saw a dramatic increase in single channel ACC across all channels (Figure 4-5E-F). Maximum single channel decoding after CAR is 77% and 89% for SD007 and SD008, respectively. Interestingly, in SD008 a block of channels in the upper-right portion of the grid jumped from among the worst to best classifying electrodes. Since in this work we sub-sample the grid, we defined CAR_{ss}, which uses only the sub-sampled channels to compute the average. On the other hand, it is important to identify whether using all the channels in the average, denoted CAR_{tot}, would improve interference removal, since the additional parallel recordings may result in a more accurate estimate of common noise. Note CAR_{ss} is the same as CAR_{tot} when all channels are sampled. ACC across square virtual grids with unit pitch, but varying number of channels (or coverage area) for all possible placements were computed. As channel count (or coverage area) increases, the general trend, irrespective of which CAR method was used, is that the median ACC increases (Figure 4-5G-H), which will be highlighted shortly. When fitting a linear mixed effects model where CAR methods and channel count were fixed effects and fold-location-channel count was the random effect, an increase in ACC was observed when applying CAR_{tot} or CAR_{ss} vs No CAR. When comparing CAR_{tot} vs No CAR, there was a 3.0% and 5.8% difference in ACC for SD007 and SD008, respectively. When comparing CAR_{ss} vs No CAR, there was no significant difference for SD007, but there was a significant difference for SD008 at 6.2%. Note, the linear mixed effects model was fit for data points that ranged from 9 to 56 channels.

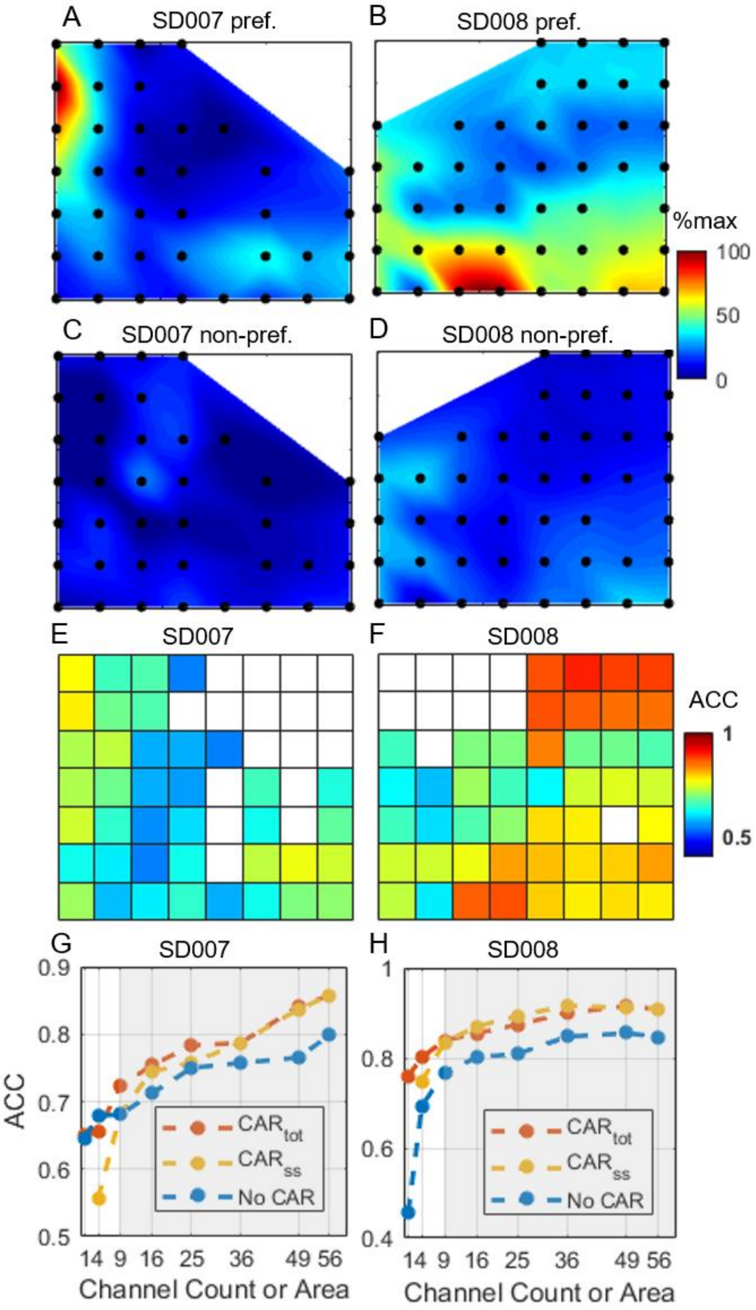

Figure 4-5: Common average referencing (CAR) can improve ACC. HFB spatial maps after doing CAR using all kept channels. Preferred stimuli for (A) SD007 and (B) SD008 vs non-preferred stimuli (C) SD007 and (D) SD008. Single channel accuracy after CAR (E) SD007 and (F) SD008. Median of the mean accuracy vs channel count (or coverage area) using minimum pitch sub-sampled grids. The mean is taken over 12 cross validation folds and the median is taken over different virtual grid placements in that order. The 3 sets are: using all channels to do CAR (CAR_{tot}), only channels that were sub-sampled (CAR_{ss}), and no CAR. A linear mixed effects model was fit for data points that have 9 to 56 channels as indicated by the shaded gray region in (G-H). The fixed effects were CAR type and channel count while the random effect was fold-location-channel count. (G) For SD007, there was a 3.0% ($p < 1e-3$, $n = 1980$) increase when applying CAR_{tot} compared to No CAR, but an insignificant increase when applying CAR_{ss} compared to No CAR. (H) For SD008, there was a 5.8% ($p < 1e-3$) difference when applying CAR_{tot} compared to No CAR, and a 6.2% ($p < 1e-3$) difference for CAR_{ss} compared to No CAR ($n = 2448$).

The effect on CAR_{tot} can also be seen on the HFB trial averages S-Figure 5and S-Figure 6. As expected, CAR_{tot} appears to greatly reduce interference in the trial averages for SD008, while in SD007 there is no obvious difference. To be consistent with the sub-sampling paradigm, we use CAR_{ss} for all subsequent analyses unless stated otherwise.

Do larger virtual grids with fixed density do better? To address this question, we sub-sampled square grids with unit pitch as depicted in Figure 4-6a. We summarized the performance of each class of virtual grids by taking the mean ACC across cross validation folds and then either the median or maximum across all virtual grid placements. Figure 4-6B-C shows these summary statistics plotted against channel count. When considering the median (red dots) performing grid across placements, there is a significant positive correlation of 1 and 0.86 for subjects SD007 and SD008, respectively. When considering the best placed grid (blue), there was significant correlation with channel count of 0.88 for SD007; however, the difference in ACC is only 10% (max) compared to 30% (median). There was no correlation for the max case in SD008. These results indicate that larger virtual grids with fixed density improves performance in general. Grids placed in the ideal location outperform the median performing grid, but less so as the grid size grows.

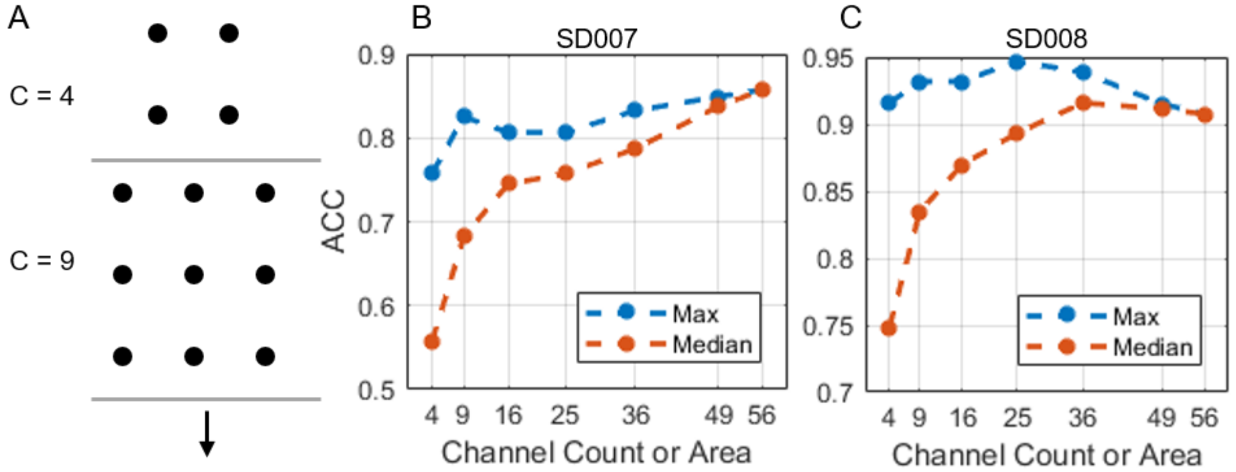

Figure 4-6: Do larger virtual grids with fixed density do better? (A) Sketch showing the grids used in this analysis are square minimum pitch grids. (B) SD007 and (C) SD008 accuracy vs channel count (or coverage area) with two sets: max of mean (blue) and median of mean (red) across all possible sub-samplings of square grids. Note, chance is 50%. The mean is taken across 12 cross validation folds and the max or median is taken across different virtual grid placements. There is a significant Spearman correlation in (B) of 1 ($p < 1e\text{-}3$) and (C) of 0.86 ($p = 0.028$) for the median of mean data points with a difference of 30% and 15% in ACC from 4 to 56 channels. For the max of mean data points only SD007 showed a significant correlation (B) of 0.88 ($p = 0.015$) with a smaller difference in ACC of 10% from 4 to 56 channels.

Does adding more electrodes within a given area improve performance? This is one way to determine if higher density is beneficial. To determine this, higher density grids were sub-sampled and ACC statistics were compared (Figure 4-7a). The notation (3,1) refers to a 3x3 grid with unit pitch and (3,1) – (2,2) means that (3,1) has it's ACC statistics subtracted from (2,2), a 2x2 grid with twice unit pitch. The top two performing high density placements were only used for each comparison in Figure 4-7B-C. The mean ACC difference across 12 cross-validation folds and two placements (n =24) was computed between the high and low density grids (Table 4-2**Error! Reference source not found.**). Histograms of the pairwise ACC differences are shown in Figure 4-7B-C. For SD007, higher density appeared more advantageous with 400μm pitch grid significantly outperforming 800μm or 1200μm pitch grids by more than 10% 3 out 4 comparisons, whereas in SD008, 400μm pitch grids significantly outperformed by 5-10% 2 out 4 comparisons ($p < 0.01$ Wilcoxon signed rank test). It is important to note that SD008 is closer to the ceiling of maximum performance, which may explain why there is smaller improvement (Table 4-2). Across both subjects, all mean differences between grids of different densities but the same area were positive suggesting that it's never detrimental to use a higher density grid with the same footprint. This result is consistent with intuition and our modeling results.

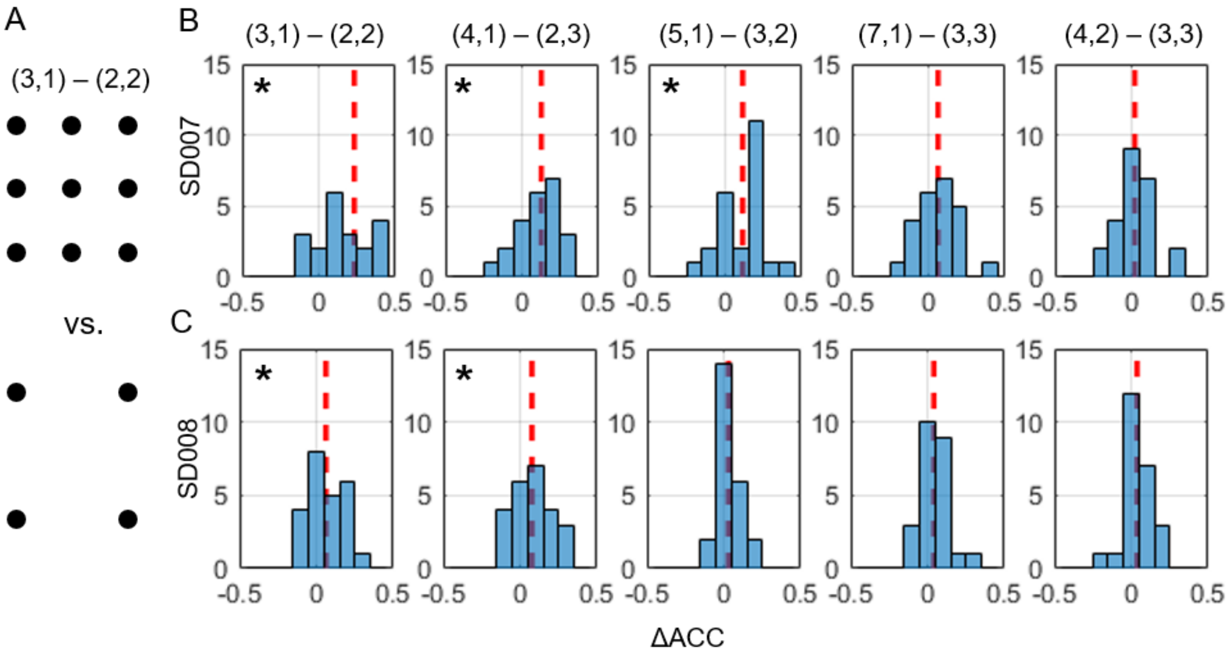

Figure 4-7: Is adding more channels to a grid with fixed area coverage beneficial? (A) Sketch comparing two sub-sampled grid types with the same coverage area: 3x3 with minimum pitch (3,1) and 2x2 with double min. pitch (2,2). (B) SD007 and (C) SD008 histograms comparing various device types of the same coverage area. The x-axis of the histogram is pairwise difference (same location) of accuracy (ΔACC) between two devices types (eg. (3,1) and (2,2)). The two best high density grid locations were used and other locations were excluded. The notation (3,1) – (2,2) means accuracies of 3x3 min. pitch devices minus 2x2 double min. pitch devices. Distribution statistics are provided in Table 2. ACC sample vectors with significantly different mean ranks are denoted with a black asterisk ($P < 0.01$). The dashed red line indicates the mean of the pairwise differences.

Table 4-2: Is adding more channels to a grid with fixed area coverage beneficial? Overall (fold + location) mean difference between paired accuracies, p-values from Wilcoxon signed-rank sum test (n = 24), and mean accuracy of the high-density grid. The mean difference of sample vectors which are significantly different from each other are denoted by **bold** ($P < 0.01$).

	SD007			SD008		
Comparison	Mean Δ	p-value	Mean HD	Mean Δ	p-value	Mean HD
(3,1) – (2,2)	**23.1%**	<1e-3	82.0%	**6.2%**	8.5e-3	92.8%
(4,1) – (2,3)	**12.5%**	1.4e-3	79.5%	**7.7%**	4.7e-3	92.4%
(5,1) – (3,2)	**11.3%**	1.6e-3	79.9%	3.1%	0.059	93.5%
(7,1) – (3,3)	6.3%	0.043	83.7%	4.1%	0.080	91.1%
(4,2) – (3,3)	2.0%	0.45	79.5%	3.9%	0.063	90.8%

4.3.3. Discussion

The central question we explored in this work is “do higher density grids convey a benefit for neural state decoding?” We demonstrated empirically from intraoperative human electrophysiology data, obtained from cortical surface μECoG while two subjects were awake and engaged in an audio-visual task, that neural state estimation is improved with increased spatial resolution. Furthermore, we formulated a model with simple, yet informed assumptions to explore when higher density might outperform lower density.

In the model, we explored how signal spread (σ_S) and noise spread (λ) among channels affect the difference in performance between high and low density grids? Using the model, we derive expressions for the difference in performance (squared Mahalanobis distance) in the 2-channel case and numerically compute it in the 25-channel case. Taken together, we find that there are two regimes where high density grids strongly outperform: I) σ_S small and λ is large or II) σ_S is large and λ is small. In words, this occurs when there I) is a focal spatial activation or II) when there is less correlated noise among neighboring channels, but not both. There is never a disadvantage in high density when the grid is directly sub-sampled within a given area, but there can be a disadvantage when channel count is fixed and electrodes are brought closer. It is counterproductive to bring channels closer together if the signal across space is broad and correlation among channels falls off considerably across space. To our knowledge, this is the first time a model has been demonstrated which relates basic channel statistics such as correlation among channels to a functionally relevant metric, classification performance. This is important because many studies primarily report empirical results such as channel correlation computed from time series as function of distance (Insanally et al., 2016; Kellis et al., 2016; Leah Muller et al., 2016b; Trumpis et al., 2017a), which alone can have limited and possibly misleading interpretations. A frequent assumption is that sharper falloff in channel correlation or other similarity metrics across distance indicates value in high density while a broad falloff indicates lack of value (Kellis et al., 2016; Leah Muller et al., 2016b). This intuition is contradicted by the modeling results, which shows that a classifier using features from a high density grid can substantially outperform a low density grid even when there is high channel correlation (effect II). Insights made from modeling efforts, like those presented here, will likely be important for informing µECoG device design for scientific research, clinical mapping and brain-machine interface applications.

A limitation of the presented analyses is that placement was fixed and assumed to be ideal in all cases. That is, the peak activation occurred at the center of the grids. In real datasets, this need not be the case as illustrated from our own datasets (Figure 4-4 and Figure 4-5). This placement constraint can lead to counterintuitive results such as there is little performance gain from low to high density grids when both noise and signal decay rapidly. There is no performance gain because, the center channel picks up the same signal, while the surrounding electrodes pick up uncorrelated noise. In actual recordings the peak activation could be located off center or between electrodes where finer sampling would be advantageous to reduce the expected distance between peak activation and a nearest neighbor electrode. Since in the modeling work, we only focused on the case where the peak activation was centered, these results can be viewed as conservative or an underestimate of the advantages of high density grids. Analysis and simulations that look at various peak locations is important future work.

Another limitation of the model is that structure of the signal and noise is assumed to fall-off exponentially across space. Although studies have found that a decaying exponential models the fall-off of channels statistics across space well, the structure of the neural spatial response is likely to vary between cortical regions and with neural state. The neural response may take on multifaceted patterns with multiple sources organized sparsely in space, which motivates the use of high-density grids to finely sample the cortical surface. High-density grids may enable the development of more accurate models to capture the structure of neural response across space.

We found empirically that μECoG grids with 400μm outperformed 800μm and 1200μm when controlling for area. Mean pairwise ACC differences were as large as 23.1% and appeared to be larger for SD007 compared to SD008 suggesting that higher density grids with the same footprint were more advantageous in SD007 vs SD008. Mean differences were consistently positive suggesting that, within this range of inter-contact densities, adding more channels within a given footprint does not reduce state estimation performance which is intuitive and consistent with modeling results. This is the first time that 400μm grids have been shown to significantly outperform larger pitch grids placed on human cortex; 400μm pitch is 5x smaller than previous work (Leah Muller et al., 2016a). Note, that (Leah Muller et al., 2016a) only directly sub-sampled the original grid roughly similar to fixing area, but did not show results for fixing channel count.

In many practical situations though, the number of channels is a limiting factor, and so an important density comparison is to vary pitch while controlling for number of channels. Due to the number of bad channels within our microgrid, particularly for SD007, we were not able to perform this analysis in an unbiased fashion as there tended to be a larger percentage of good channels for the denser virtual grids for this particular comparison (S-Figure 10). Although the results of this analysis will likely overestimate the performance of denser, the results may still be informative. When controlling for channels in both subjects, μECoG grids with a smaller pitch did not significantly differ from their larger pitch counterparts except once. In fact, we observed negative means suggesting that higher density grids may underperform their lower density counterparts when controlling for channel count (S-Figure 9). Taken together with the bias, we can conclude that high density grids certainly have not outperformed lower density grids while controlling for channel count.

The empirical results of two subjects provide an existence proof that 400µm grids can outperform lower density grids with respect to neural state estimation. However, the extent to which these results generalize to a wider range of neural state estimation problems, cortical areas, and subjects, will require a substantially expanded clinical research trial with high-density/low-impedance electrode technologies that are currently not available commercially. Thus, these empirical findings are not intended to validate the presented modeling framework. The purpose of the model is to provide insight into potential circumstances under which high density grids might outperform low density grids and to utilize these insights towards aiding in the interpretation of these and future empirical findings. More sophisticated models will need to be developed to precisely model real data.

In evaluating the empirical results, it is important to note that common average reference (CAR), although intended to improve single channel signal fidelity, can have deleterious effects on signal quality. Ideally, CAR is applied to a set of signals contaminated with identical artifact such as 60 Hz artifacts, in which case CAR will eliminate it. But, if only few channels contain artifacts, the artifacts will be introduced to all other signals. This is likely not the case for either subject as applying CAR does not reduce decoding performance (Figure 4-5) or visibly contaminate channels in the HFB trial averages (S-Figure 5 and S-Figure 6). On the other hand, if half of signals recorded from a grid are similar to each other, and the other half are also similar to each other, but different from the first half, then CAR will introduce many interdependencies/correlations. This is likely not the case for the analyses conducted for SD007 and SD008 since the HFB spatial response remains focal after CAR (Figure 4-3, S-Figure 5 and S-Figure 6). Nevertheless, it is important to understand the implications of CAR, especially for µECoG since it can drastically alter the signals and their interpretation.

The choice of learning algorithm used to assess grid performance is important. A poor choice that is not robust to high dimensional datasets will likely underperform, due to overfitting. We chose ELR, because it performs feature selection while optimizing parameters, making it robust to high dimensional datasets. Furthermore, ELR manages highly correlated variables well by promoting a group of correlated variables to be either all in or out (Zou and Hastie, 2005).

One limitation of these experiments was the small coverage area of the µECoG probe, which was approximately 3mm by 3mm. The small coverage area makes it difficult to align the recording region to the brain regions of interest. This is illustrated in SD007, where the HFB response only starts to become apparent on the left edge of the grid. If a larger grid was used, we may have been able to measure the full extent of the spatial response and be able to center the virtual grids over regions of peak activation for better grid comparison. A major challenge to increasing the area for such small pitch grids is scaling connectors and amplification circuits. However, we anticipate that advances in technology will make higher channel count systems cheaper and easier to access (Hermiz et al., 2016; Insanally et al., 2016; Trumpis et al., 2017a), thus making higher density probes more attractive to use.

4.3.4. Conclusion

Here we report the first instance of 400µm pitch grids outperforming lower density grids in estimating cognitive neural states from humans. We also explored how signal and noise spatial properties affect the performance gap between low and high-density grids by developing an illustrative model, which we found to be consistent with our empirical results. In the future, we plan to add more channels to increase the coverage area, extend the presented model and explore other signal features. Increasing channel count and footprint of the µECoG will be important for fully exploring possible advantages over ECoG. The presented model could evolve to become an important piece in a design method for µECoG probes. The design method could take as input specifications such as desired classification accuracy, channel count and expected characteristic lengths and output the optimal pitch for specific applications. Finally, finer spatial scales may allow us to measure novel neural dynamics such as wave propagation or spiking activity. We plan to explore other signal features to potentially uncover novel neural dynamics only visible at the micrometer scale.

This chapter is a reprint of material as it appears in NeuroImage 2018, “Sub-millimeter ECoG pitch in human enables higher fidelity cognitive neural state estimation” Hermiz J, Rogers N, Kaestner E, Ganji M, Cleary D, Carter B, Barba D, Dayeh S, Halgren E, Gilja V.

Chapter 5.

Conclusion

Micro-ECoG is a promising neural interfacing technology that has several advantages over other electrophysiological sensing methods. It has the combined benefits of large coverage and high resolution and is arguably less invasive than intracortical probes. In this dissertation, I demonstrated the value of micro-ECoG by showing that it can lead to enhanced discrete neural state estimation. Additionally, I reproduce important work by Khodagoly et al, showing that micro-ECoG can record single units. Moreover, I found that single unit activity from the surface electrodes was driven by auditory stimulus, the first demonstrated relationship between sensory input and single unit activity from the surface of the brain. Finally, I developed an open source suite of data acquisition tools for clinical electrophysical research that permitted data collection of the presented human electrophysiology and that may enable other researchers to conduct human electrophysiology.

In Chapter 2, I presented a clinic compatible data acquisition system. This system consists of a controller box that can accept up to 256 channels, sampled 30 kHZ from Intan amplifiers. The controller box consists of the RHD2000 USB from Intan and power and digital isolator for patient safety. The controller is housed in plastic case with bulkhead connectors making the unit water resistant. The system also features several custom headstages designed for several applications. The ORH128 has 4 Intan amplifier integrated into one board for acquisition of up to 124 channels, which was used to record from micro-ECoG intraoperatively. The pigtail splitter allows researchers to tap into existing clinical electrophysiology pipelines without altering clinical flow. It incorporates so called Cabrillo © style connectors, which plug into a custom board. This headstage is housed in a compact 3D printed case that be placed in a headwrap and can be plugged into the aforementioned isolated controller for data acquisition. Overall, these tools are an affordable alternative to costly commercial research systems and is more tailored for clinic research use than existing open source systems.

In Chapter 3, I present physiologically relevant signals measured by micro-ECoG compared to control probes. The first work I present, demonstrates the ability of micro-ECoG to sense single units in songbirds. These single units measured from the surface are compared to single units measured from traditional penetrating silicon shanks. Interestingly, the surface and depth single units appear to have different characteristics, including, the spike duration and amplitude. Single units from the surface have significantly shorter (one-third) durations and smaller amplitudes (one-half) than depth single units. These and other characteristics may indicate sampling biases of cell types or cell location from surface and depth electrodes. Further investigation of songbird neural anatomy is needed to help elucidate the reasons for different single unit characteristics. I also showed that a population of the surface single units increased their firing rate upon the presentation of an auditory stimuli in a similar fashion to depth single units. This is the first time that single units from the surface have shown to be related to sensory input providing new line of evidence that these signals are in fact action potential generated from superficial neurons.

In the second part of Chapter 3, I present micro-ECoG from human subjects. Low frequency activity below 50 Hz was similar between micro-ECoG electrodes and standard clinic electrodes as determined by spectro-tempral analyses. Furthermore, transient alpha oscillations and inter-ictal discharges were observed by both micro-ECoG and ECoG in physiologically plausible conditions. Sensory stimuli evoked high gamma responses as seen by micro-ECoG electrodes. Importantly, trial averaged high gamma responses were observed to vary substantially by distances as short as 400µm, the electrode spacing. These results motivate the use of micro-ECoG for human brain mapping for research and clinical applications.

In Chapter 4, I explored when higher density grids outperform sub-sampled lower density grids in a discrete neural estimation task. First, I developed a modeling framework that assumed features belong to two classes, preferred and non-preferred, are drawn from multivariate normal distributions. The parameters of this distribution are determined by spatial properties, namely the signal and correlation decay constants. Under these assumptions, I find that higher density grids have a greater capacity to discriminate between preferred and non-preferred when either the signal decay constant is small and the correlation decay constant is large or vice versa. Interesting, this means that a high-density grid with highly correlated channels can improve decoding performance relative to low density grids. However, high density can result in detrimental decoding performance, when the number of channels in the grids is constrained to be some fix number. That is, lower density grids can outperform high density grids with the same number of channels if the correlation decay constant is roughly equal to the inter-electrode spacing. This modeling framework relates spatial properties of neural activity to functional decoding metrics that can help guide design of micro-ECoG arrays.

In the second part of Chapter 4, I empirically tested the hypothesis of whether 400µm spaced grid of electrodes outperform sub-sampled “virtual” electrode girds with 800µm and 1200µm spacing. When coverage area is fixed, I show that 400µm grids can outperform lower density grids by as much as 23% decoding accuracy in binary classification. However, when number of channels is fixed, no consistent improvement was observed. These results show that a significant boost in information can be obtained from sub-millimeter ECoG arrays, which can lead to high resolution brain mapping and high-performance brain machine interfaces.

There are several limitations and at least one notable null results from this body of work. Single units were not detected from micro-ECoG in the human experiments. This may be attributed to the lack of experimental control that could lead to increased levels of noise and sub-optimal neural interface conditions. For example, one key step performed in the songbird electrode placement is that the surface of the brain is dehydrated by suctioning fluids using a pipet to ensure intimate contact between the surface electrodes and brain tissue. If there is an excess of fluids, then this will shunt local signals making it difficult to detect single units. In a clinical setting, clinicians need to need to ensure that the brain is hydrated and thus regularly spurt saline to the brain. In a follow up to the Neurogrid study, Khodagholy et al show a sponge is used to soak up excessive fluid in the craniotomy. Furthermore, they used regularly spaced perforations which helps fluid circulate above the substrate so that there is close contact between electrode and tissue (Khodagholy et al., 2016). It is unclear if this is a clinically viable approach; however, it seems that minimizing fluids between the tissue and electrode is an important aspect of sensing highly localized signals such as putative action potentials. This may be a moot point for chronic implantations, in which the micro-ECoG may have time to closely adhere to tissue. In the Neurogrid work, they demonstrate robust, chronic recording of single units in rats for up to 10 days. Important future work will be to determine if this will translate to chronic human implants.

Scaling the number of channels in these devices is another important future direction. The devices presented in this dissertation where limited to 32 or 56 microelectrodes that span several no more than 3 x 3 mm^2 in area. However, since these devices are fabricated using planar processes, the number of microelectrodes can readily scale to the 1000s, if not 10,000s. The

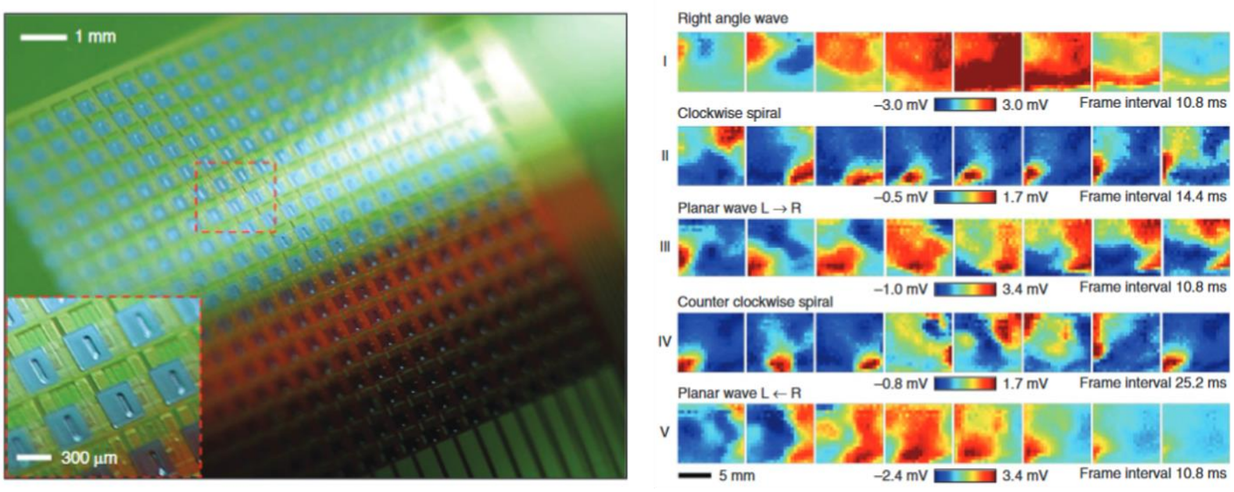

Figure 5-1: To the left is the flexible, foldable multiplexed grid of electrodes. To the right, various waves observed in feline cortex while seizing. (source: Nature Neuroscience Viventi et al 2011).

challenge towards realizing these high channel count systems is developing a scalable architecture that can connect to all these electrodes. The presented devices do mate to scalable connectors.

Each electrode is passively wired toward a bond site with pads arranged linearly. Anisotropic conductive film is bonded to the substrate and on the other end it is bonded to flat flexible cable (FFC), a linear array of wires that is compactly and somewhat rigidly held together. The FFC then connects to a PCB for amplification and analog-to-digital conversion. Since, connectors and cables that scale linearly are used as intermediaries, this architecture is not easily scalable. Using interconnects such as ball point arrays from chip packaging technology scale as a function of area not length is more readily scalable. Another approach is to integrate active electronics on the electrode substrate to avoid this wiring issue altogether. A notable example of this approach was presented by Viventi et al in 2011, where he and colleagues fabricated transistors on a flexible substrate enabling the acquisition of 360 channels (Figure 5-1). One challenge with this approach will be to fabricate reliable, homogenous and robust transistors on thin-film substrates. In spite of these challenges, I am optimistic that academic and commercial ventures will be able to scale the number of microelectrodes on these thin-film substrates by order of magnitudes in the near future.

As grid dimensions scale from on the order of 10 x 10 to 100 x 100 channels, neural data analysis methods should evolve. Data representation, computational scalability, and methods of extracting meaning from data are aspects that should be reconsidered. Often times neurophysiological records are represented as montage, where the data matrix is channels by samples. As the number of electrodes grow, the grids of electrodes can be likened to a high-density screen displaying the evolution of neural dynamics over time. This analogy motivates representing neural data using a tensor, where the dimensions are x-axis electrodes by y-axis electrodes by samples. This representation was used to show the propagation of recurrent spiral waves, which was induced by administering seizure causing drugs in cat (Viventi et al., 2011). In general, cortical waves is a topic of growing interest in the neuroscience (Lyle Muller et al., 2016; Muller et al., 2018) and given the high spatiotemporal resolution of micro-ECoG, it is an excellent tool to study this phenomenon.

High-density micro-ECoG can be likened to an HD window into the brain. This motivates the application of several classes of algorithms that have been shown to extract meaning from frames of images like computer vision and deep learning techniques. These techniques can be used to discover novel , yet subtle cortical patterns subtle in the face of noise (Song et al., 2017b, 2017a) . Other potential approaches could be to use array processing techniques like beamforming to localize cortical and sub-cortical activity such as seizure foci. Finally, compression and compressive sampling approaches will become increasingly relevant as the amount of data processed and stored grows exponentially (Craven et al., 2015; Ganguli and Sompolinsky, 2012).

Micro-ECoG is posited to lead to new neuroscience discoveries and towards new clinical applications. Furthermore, it may also lead towards a high-performance brain-machine interfaces that surpasses the bandwidth of current BMIs or even the bandwidth of communication between the brain and body potentially enhancing human capability. This possibility as well as other BMIs technologies raises important ethical questions such as those described in Yuste and Goering et al including privacy and consent, agency and identity, augmentation and bias (Yuste et al., 2017). It is incumbent upon neurotechnologist and scientist to educate the public on the potential hazards of this technology. Furthermore, hasty deployment of this technology without adequate time for proper dialogue and regulations to be established may lead to negative outcomes that harm people and prohibit the development of neurotechnology. As with any technology, it is our responsibility as a society to use neurotechnology wisely and for the benefit of humankind.

Appendix A: Song-bird micro-ECoG Supplementary

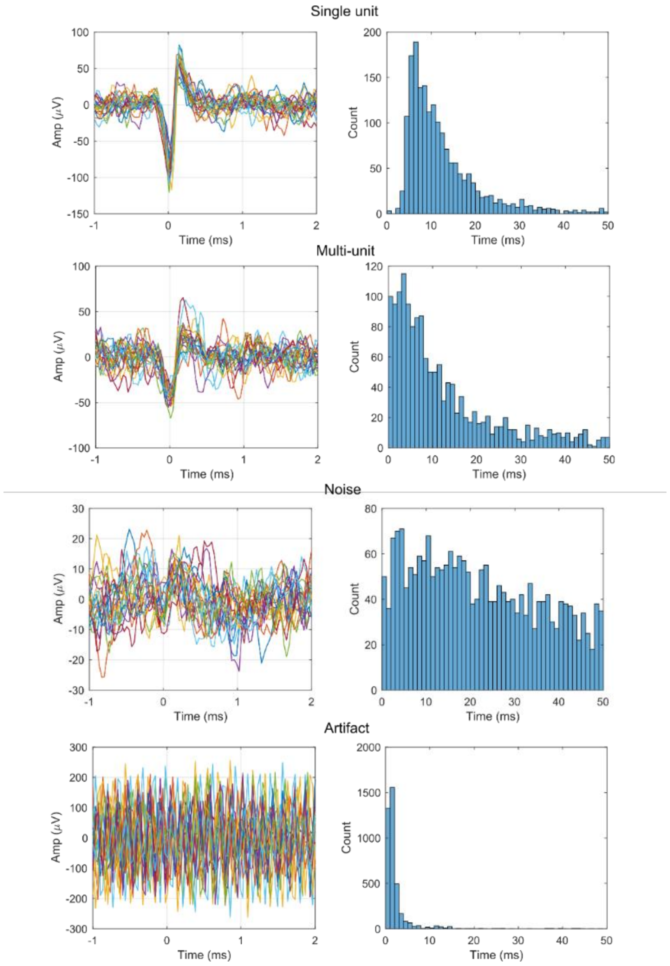

S-Figure 1: Examples of unit labeling. The four possible labels are shown from top to bottom: single unit, multi-unit, noise and artifact. On the left are 50 snippets from that cluster sampled uniformly over the recordings. On the right are inter-spike-interval histograms showing the number of spikes that occur within a certain period ranging from 0 to 50 ms after all spikes occurred.

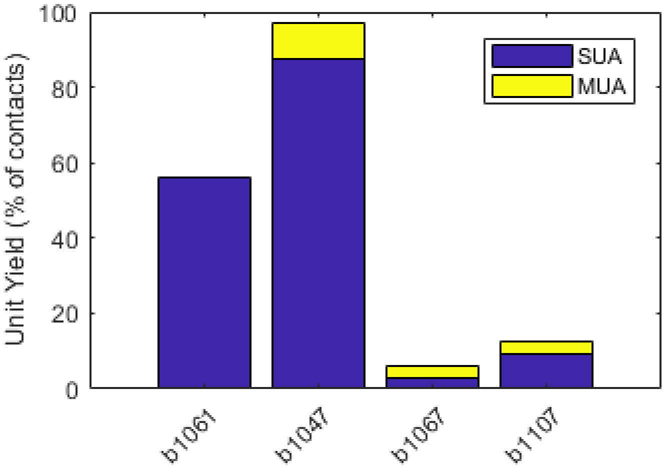

S-Figure 2: Depth unit yield. The unit yield for depth units as percentage of the number of channels. The stacked bar plot shows the percentage of single units (SUA) and multi-units (MUA) for each subject.

Appendix B: Enhanced Neural State Estimation Supplementary

Data Acquisition

Data was acquired using a custom built system described in (Hermiz et al., 2016). Briefly, the system uses a 64-channel amplifier/digitizer boards (RHD2164) from Intan Technologies (Los Angeles, CA). The digitized signals are then sent through a power isolation stage for patient safety. Finally, the signals are buffered using the RHD2000 USB board and then sent to a host laptop for visualization and storage. Data was acquired at 20kHz and hardware filters were set to 0.1 and 7500 Hz for high and low pass cutoffs, respectively.

Signal Processing

For the real recordings, the signal processing pipeline extracts high frequency band (HFB) rectified amplitude (Fig 4B). HFB is also commonly referred to as high-gamma. In addition to processing steps shown in Fig 3B, decimation down to 2kHz as an initial step using a 30th order Hamming window FIR filter. All other filters were 3rd Butterworth IIR. To eliminate phase distortions, signals were filtered in the forward and reverse direction. Channels with excessive and obvious noise (eg. line noise) as determined by manually inspecting the raw time series were removed. Trials with excessive artefactual fluctuations as determined by a hard threshold were eliminated. Custom Matlab software (Natick, MA) was used to perform signal processing.

Statistics

Unless specified otherwise, the Wilcoxon signed-rank test was performed to determine if the distribution of two pairwise samples differ significantly The Wilcoxon signed-rank test was chosen because it is a robust test that makes little assumptions on the data. For correlation, Spearman's rho was used and a two-tail t-test was used to determine if correlation was significant. Spearman's correlation coefficient was used because were interested in determining if there was a monotonically increasing or decreasing relationship that was not necessarily linear between data samples. Statistical tests were executed by standard Matlab functions.

A linear mixed effects model was used to determine if a variable significantly altered a target variable. In Fig. 5, the following linear mixed effects model was fit: *ACC~CarType+ChanCnt+*(*1*|*FLC*). The target variable is classification accuracy (ACC). The fixed effects are CAR method (eg. No CAR, CAR_{tot}, and CAR_{ss}) and channel count. And the random effect is a categorical variable that uniquely specifies the cross-validation fold, location and channel count (FLC) of the data point that generated a particular ACC. Ignoring cross-validation fold, the variable location and channel count (LC) can be thought of as uniquely specifying a particular virtual grid. Hence, this linear mixed effect model is accounting for the random effect from every virtual grid. In fact, since we use FLC, it is accounting for the random effect from every virtual grid and cross-validation fold. The cardinality of the categorical variable FLC is: (# of folds) x (# of virtual grids generated).

"The metric plotted in Fig 5-6, "median of mean accuracy" or "max of mean accuracy" was computed over two variables: cross validation fold and location. Location refers to the spot the virtual grid was placed within the full grid. For example, a 2x2 grid with unit pitch can be placed in the upper left hand corner, the lower right hand corner, and so on and so forth. We compute the accuracy for all possible locations for a particular grid configuration. So, there is a list of arrays, $[L_1, \ldots, L_i, \ldots L_N]$, where L_i is a 12x1 array of accuracy values computed over each fold for the i_{th} location of the virtual grid. This list of arrays is summarized by computing statistics over them. In Fig 5G-H, each point is the median ($[L_{avg,1}, \ldots, L_{avg,i}, \ldots L_{avg,N}]$), where $L_{avg,i} =$ mean (L_i). In Figure 6B-C, the red points are median ($[L_{avg,1}, \ldots, L_{avg,i}, \ldots L_{avg,N}]$), and the blue points are max ($[L_{avg,1}, \ldots, L_{avg,i}, \ldots L_{avg,N}]$)."

Modeling

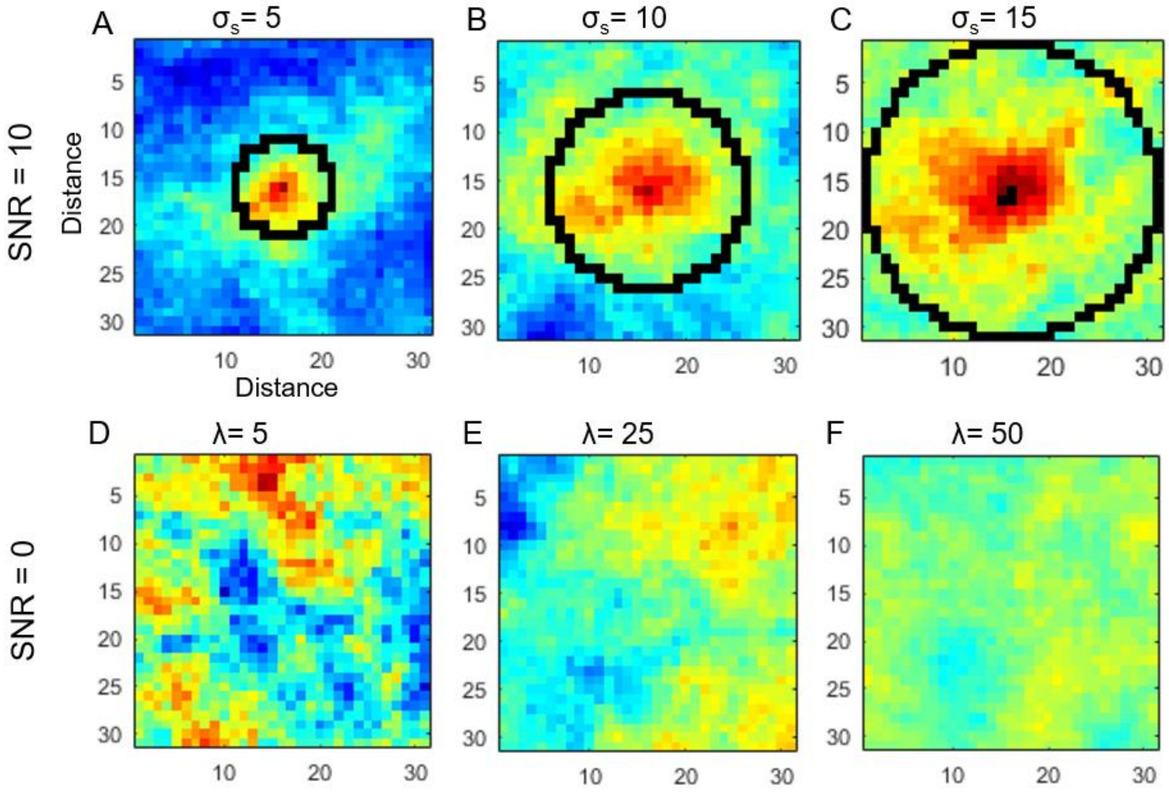

S-Figure 3: Visualizing signal and noise decay constants. Each panel (A-E) is a plot of simulated 31 x 31 electrode grid, where each pixel represents an electrode. Pixel color is the measurement simulated on each electrode. (A-C) Illustrates the effect of the signal decay constant, σ_s by fixing SNR = 10 and varying the value of σ_s from (A) 5 to (B) 10 to (C) 15. As σ_s increases, which is depicted by the black circle, the area that the signal encompasses increases. The color ranges from -3 (dark blue) to 10 (dark red). (D-F) Illustrates the effect of the noise decay constant, λ, by fixing SNR = 0 and varying the value λ from (D) 5 to (E) 10 to (F) 15. As λ increases the noise correlation between electrodes increases, which can be seen by the increased smoothness across the grid. The color ranges from -3 (dark blue) to 3 (dark red) for panel D-E.

Derivation of Eqn 8

$$\Delta_{2,1} = d^2_{x_1,x_2} - d^2_{x_1},$$

where $d^2_{x_1,x_2}$ is the squared Mahalanobis distance when using channels x_1 and x_2 and $d^2_{x_1}$ is for just x_1. From the definition of the Mahalanobis distance,

$$d^2_{x_1,x_2} = \boldsymbol{s}\boldsymbol{\Sigma}^{-1}\boldsymbol{s}$$

$$= [s_1 \; s_2] \begin{bmatrix} \Sigma_{11} & \Sigma_{21} \\ \Sigma_{21} & \Sigma_{22} \end{bmatrix}^{-1} \begin{bmatrix} s_1 \\ s_2 \end{bmatrix}$$

Substituting $\Sigma_{11} = \Sigma_{22} = 1$ and inverting the 2x2 matrix,

$$= \frac{1}{1 - \Sigma_{21}^2} [s_1 \; s_2] \begin{bmatrix} 1 & -\Sigma_{21} \\ -\Sigma_{21} & 1 \end{bmatrix} \begin{bmatrix} s_1 \\ s_2 \end{bmatrix}$$

Matrix multiply and collect terms,

$$d_{x_1,x_2}^2 = 1/(1 - \Sigma_{21}^2)(s_1^2 + s_2^2 - 2s_1 s_2 \Sigma_{21})$$

Again, from the definition of the Mahalanobis distance (in the scalar case),

$$d_{x_1}^2 = s_1^2$$

Substitute d_{x_1,x_2}^2 and $d_{x_1}^2$ in $\Delta_{2,1}$,

$$\Delta_{2,1} = \frac{1}{(1 - \Sigma_{21}^2)}(s_1^2 + s_2^2 - 2s_1 s_2 \Sigma_{21}) - s_1^2$$

Put terms under a common denominator,

$$\Delta_{2,1} = \frac{s_1^2 + s_2^2 - 2s_1 s_2 \Sigma_{21} - (1 - \Sigma_{21}^2)s_1^2}{(1 - \Sigma_{21}^2)}$$

Simplify,

$$\Delta_{2,1} = \frac{s_2^2 - 2s_1 s_2 \Sigma_{21} + (s_1 \Sigma_{21})^2}{(1 - \Sigma_{21}^2)}$$

Factor the numerator as a square,

$$\Delta_{2,1} = \frac{(s_2 - s_1 \Sigma_{21})^2}{(1 - \Sigma_{21}^2)}$$

Derivation of Eqn 9

$$\Delta_{2,2'} = d_{x_1,x_2}^2 - d_{x_1,x_2'}^2$$

Note that,

$$d_{x_1,x_2}^2 = \Delta_{21} + s_1^2$$

$$d_{x_1,x_2'}^2 = \Delta_{2'1} + s_1^2$$

Substituting these expressions into $\Delta_{2,2'}$ and canceling s_1^2,

$$\Delta_{2,2'} = \frac{(s_2 - s_1 \Sigma_{21})^2}{(1 - \Sigma_{21}^2)} - \frac{(s_{2'} - s_1 \Sigma_{2'1})^2}{\left(1 - \Sigma_{2'1}^2\right)}$$

Identical measurements

$\Delta_{2,1}$ has a minimum of 0 and it is obtained when $s_2 = \Sigma_{12}$. One situation in which this minimum is realized is when channel 1 and 2 approach being identical, which is intuitive, although not necessarily obvious from Eqn **8** because of the singularity. We confirm this analytically by using L'Hospital's rule to evaluate the limit of Eqn **8** as Σ_{21} approaches 1 and where s_1=s_2.

Assume, $s_1 = s_2 = a$, simplify notation by setting $\Sigma_{21} = z$ and taking the limit as z approaches 1

$$\lim_{z\to 1} \Delta_{2,1} = \lim_{z\to 1} \frac{a^2(1-z)^2}{(1-z^2)}$$

Since, the limit is equal to 0/0 which is undefined, L'Hospital's Rule is used,

$$\lim_{z\to 1} \frac{a^2(1-z)^2}{(1-z^2)} = \lim_{z\to 1} \frac{\frac{d}{dz} a^2(1-z)^2}{\frac{d}{dz}(1-z^2)}$$

Taking the derivative of the numerator and denominator and simplifying

$$\lim_{z\to 1} \frac{-2a^2(1-z)}{-2z} = \lim_{z\to 1} a^2(\frac{1}{z} - 1)$$

Evaluating the limit,

$$\lim_{z\to 1} \Delta_{2,1} = 0$$

Derivation of Eqn 13

From the definition of correlation,

$$\rho_{x_1,x_j} = \frac{E[(\boldsymbol{x_1} - \mu_1)(\boldsymbol{x_j} - \mu_j)]}{\sqrt{E[(\boldsymbol{x_1} - \mu_1)^2]}\sqrt{E\left[(\boldsymbol{x_j} - \mu_j)^2\right]}}$$

where $E[\boldsymbol{x_i}] = \mu_i$. Start with the square of the first term in the denominator. Substitute $\boldsymbol{x_1} = \boldsymbol{f_1} + \boldsymbol{n_1}$ (first row of matrix Eqn. 10).

$$E[(\boldsymbol{x_1} - \mu_1)^2] = E[(\boldsymbol{f_1} + \boldsymbol{n_1} - \mu_1)(\boldsymbol{f_1} + \boldsymbol{n_1} - \mu_1)]$$

Expand and collect terms,

$$E[(\boldsymbol{x_1}-\mu_1)^2] = E[\boldsymbol{f_1}^2+\boldsymbol{n_1}^2+\mu_1^2+2\boldsymbol{f_1}\boldsymbol{n_1}-2\boldsymbol{f_1}\mu_1-2\boldsymbol{n_1}\mu_1]$$

Note that $E[\boldsymbol{n_1}]=0$, $E[\boldsymbol{n_1}^2]=\Sigma_{11}$, and $E[\boldsymbol{f_1}]=\mu_1$, and call $E[\boldsymbol{f_1^2}]=p$.

$$E[(\boldsymbol{x_1}-\mu_1)^2]=p+\Sigma_{11}+\mu_1-2\mu_1$$

Simplify, re-arrange terms and take the square-root,

$$\sqrt{E[(\boldsymbol{x_1}-\mu_1)^2]}=\sqrt{\Sigma_{11}+p-\mu_1}$$

Similarly, the square of the second term in the denominator is,

$$E\left[\left(\boldsymbol{x_j}-\mu_j\right)^2\right] = E[\boldsymbol{f_j}^2+\boldsymbol{n_j}^2+\mu_j^2+2\boldsymbol{f_j}\boldsymbol{n_j}-2\boldsymbol{f_j}\mu_j-2\boldsymbol{n_j}\mu_j]$$

Note that $E[\boldsymbol{n_j}]=0, E[\boldsymbol{n_j}^2]=\Sigma_{jj}$, and $E[\boldsymbol{f_j}]=\mu_j$. Furthermore, from Eqn. 11 $\boldsymbol{f_j}=\alpha_j\boldsymbol{f_1}$. Therefore,

$$E\left[\left(\boldsymbol{x_j}-\mu_j\right)^2\right]=\alpha_j^2E[\boldsymbol{f_1}^2]+\Sigma_{jj}+\mu_j^2-2\mu_j^2$$

Recall, $E[\boldsymbol{f_1}^2]=p$, simplify, re-arrange terms, and take the square-root,

$$\sqrt{E\left[\left(\boldsymbol{x_j}-\mu_j\right)^2\right]}=\sqrt{\Sigma_{jj}+\alpha_j^2p-\mu_j^2}$$

Finally, the numerator can be written as,

$$E[(\boldsymbol{x_1}-\mu_1)(\boldsymbol{x_j}-\mu_j)]=E[(\boldsymbol{f_1}+\boldsymbol{n_1}-\mu_1)(\boldsymbol{f_j}+\boldsymbol{n_j}-\mu_j)]$$

Multiply out terms and simplify all terms with n_1 or n_j,

$$E[(\boldsymbol{x_1}-\mu_1)(\boldsymbol{x_j}-\mu_j)]=E[\boldsymbol{f_1}\boldsymbol{f_j}-\boldsymbol{f_1}\mu_j+\Sigma_{1j}-\boldsymbol{f_j}\mu_1+\mu_1\mu_j]$$

Simplify further and re-arrange terms,

$$E[(\boldsymbol{x_1}-\mu_1)(\boldsymbol{x_j}-\mu_j)] = \Sigma_{1j} + \alpha_j p - \mu_1\mu_j$$

Finally collect all terms from the correlation equation, which yields,

$$\rho_{x_1x_j} = \frac{(\Sigma_{1j}+\alpha_j p - \mu_1\mu_j)}{\sqrt{\Sigma_{11}+p-\mu_1^2}\sqrt{\Sigma_{jj}+\alpha_j^2 p-\mu_j^2}}$$

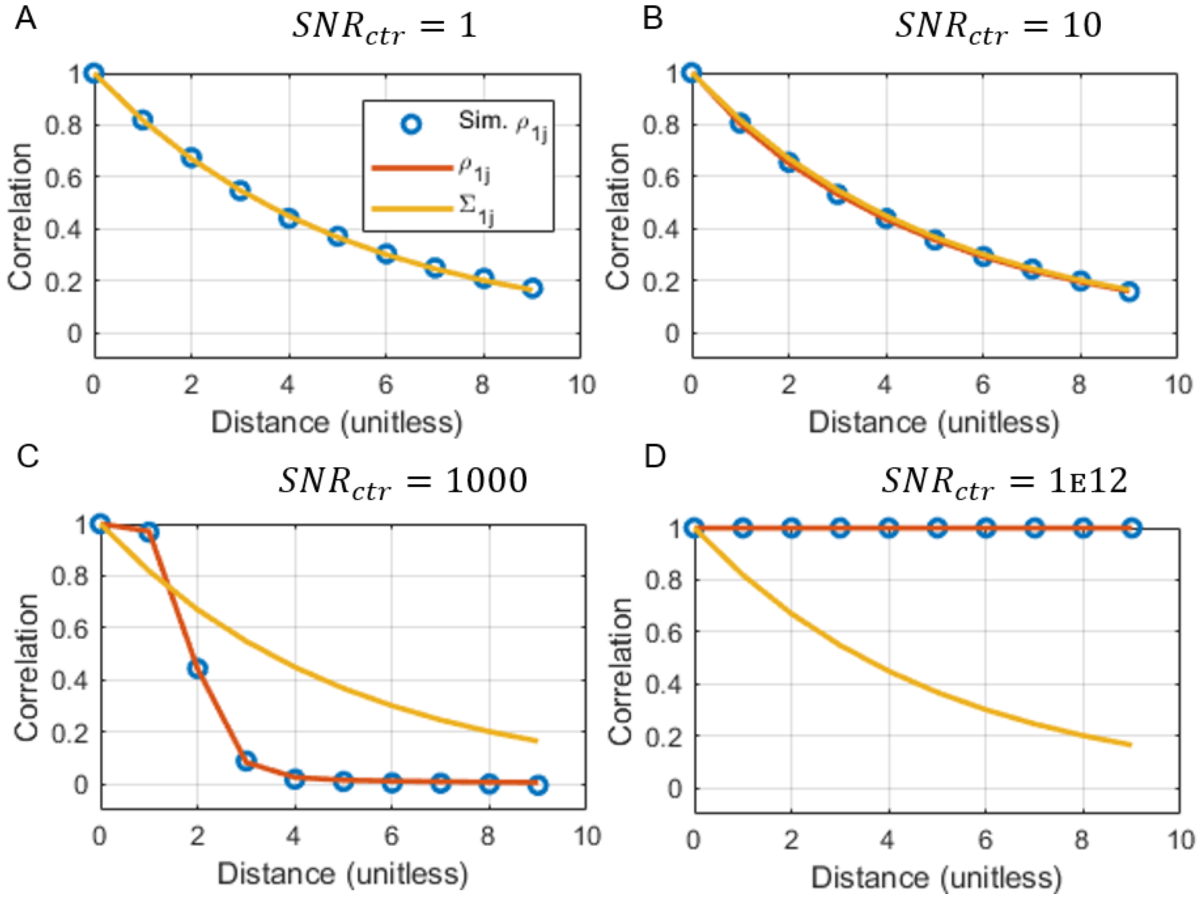

S-Figure 4: Correlation vs distance computed by 1) simulated average $\rho_{x_1x_j}$ given by Eqn **10** (blue dots) 2) the analytical expression of $\rho_{x_1x_j}$ given by Eqn **13** (red line) and 3) the noise correlation model given by Eqn **3** (orange line). The different panels (A), (B) and (C) and (D) correspond to center channel SNR of 1, 10, 1000, and 1e12, respectively. The remaining model parameters were fixed to be: $\sigma_s = 0.5$, $\sigma_t = 25$, and $\lambda = 5$.

HFB Trial Averages

S-Figure 5: SD007 trial averages of HFB activity for (A) no CAR and (B) CAR. The red and blue line are HFB activity due to the preferred (auditory words) and non-preferred (visual pictures) stimuli, respectively. The shaded area around the lines indicate standard error 95% c.i. Areas with white spaces indicate channels that were deemed “bad” and removed from the analysis. The x and y-axis grid spacing is 400ms and 1 μV

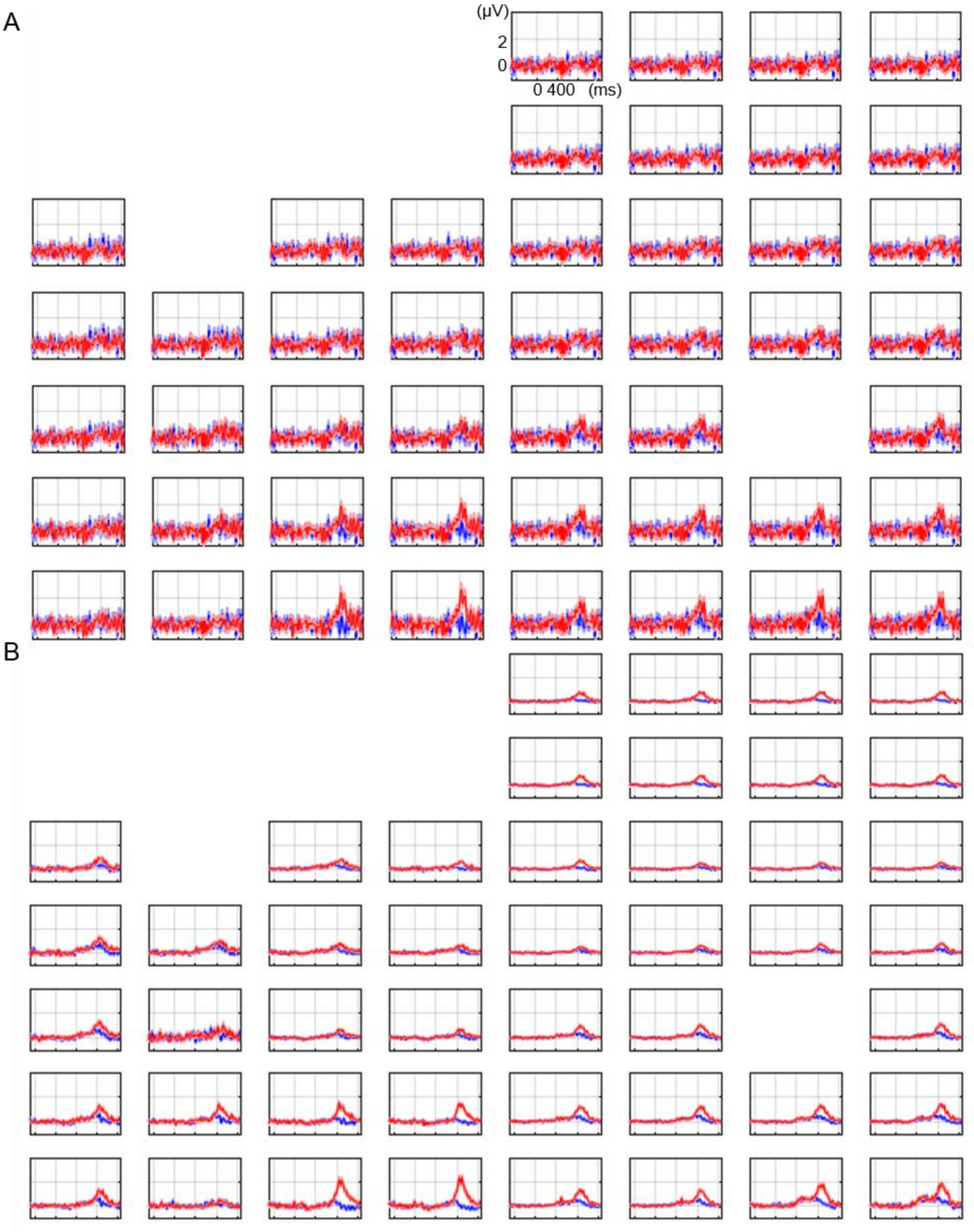

S-Figure 6: SD008 trial averages of HFB activity for (A) no CAR and (B) CAR. The red and blue line are HFB activity due to the preferred (noise-vocoded) and non-preferred (human voice) stimuli, respectively. The shaded area around the lines indicate standard error 95% c.i. Areas with whites spaces indicate channels that were deemed “bad” and removed from the analysis. The x and y-axis grid spacing is 400ms and 2μV

HFB Correlation vs Distance

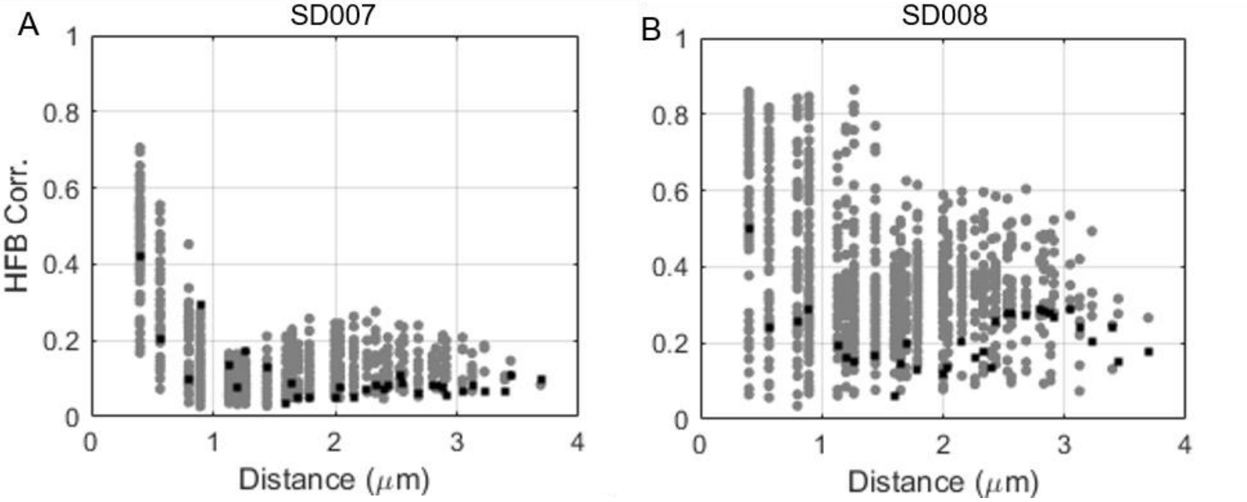

S-Figure 7: High Frequency Band (HFB) rectified channel correlation vs channel distance (µm) for (A) SD007 and (B) SD008. The gray dots represent each pairwise correlation vs distance value and the black dots is the mean for all data points for a given distance.

Averaging Channels

Averaging channels from a unit pitch grid is one way to enhance the signal over noise of the channel by eliminating uncorrelated noise. We explored if averaging outperforms not averaging by inserting a channel averaging step in the signal processing pipeline after CAR (Fig 4B). CAR_{tot} was used because CAR_{ss} could not be applied to the averaged signals as that would zero out the signal. Alternatively, we could have not applied CAR, but that would have limited performance particularly for SD008. Averaging across electrodes results in lower performance than not averaging in both subjects and there is a significant difference for each channel count except for 4 and 9 in SD007 ($p < 0.01$, Wilcoxon signed rank test see Table S1). There is a larger performance gap between “Not Avg” vs “Avg” in SD008 compared to SD007 (Fig S6B-C). For example, the mean difference in ACC at 49 channels is 16.8% (SD008) compared to 9.8% (SD007) – note positive values indicate that “Not Avg” outperforms “Avg”. While there is positive Spearman correlation between ACC and channel count of 1 for SD007, there is no correlation for

SD008. These results indicate that averaging channels is sub-optimal and that the performance relative to not averaging varies. It appears that averaging was more detrimental to SD008 than SD007.

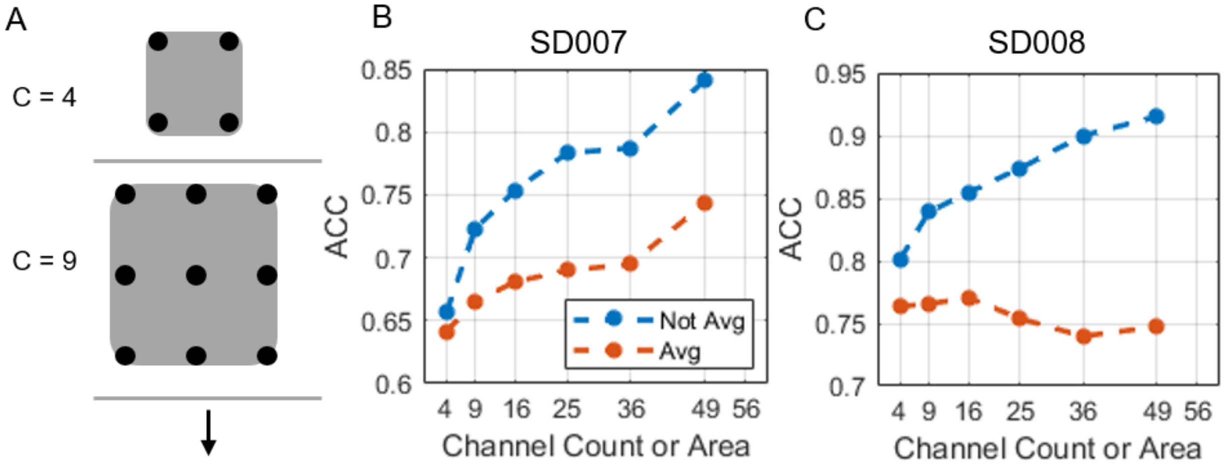

S-Figure 8: Averaging vs not averaging electrodes. (A) Sketch showing averaging across the sub-sampled grids. Averaging occurs after CAR but before 70 – 170 Hz bandpass filtering in Fig 1B. (B) SD007 and (C) SD008 median of mean accuracy vs channel count (or coverage area) for two sets: not averaged (blue) and averaged (red). Note, chance is 50% The mean is taken across 12 cross validation folds and the median is taken across different virtual grid placements. There is a significant Spearman correlation of 1 (p = 0.0028) between "Avg" ACC vs channel count for SD007, but not for SD008. Note correlation for the "Not Avg" data points was not computed here as they were computed in Fig 5. For SD007, there is a significant difference between "Not Avg" vs "Avg" ACC for each channel count except for 4 and 9 (p < 0.01, Wilcoxon signed rank test). For SD008, there is a significant difference between "Not Avg" vs "Avg" ACC for each channel count.

	SD007			SD008		
Channel Cnt.	Mean Δ	p-value	n	Mean Δ	p-value	n
4	0%	0.71	396	**2.1%**	< 1e-3	444
9	*2.3%*	0.016	252	**4.8%**	< 1e-3	336
16	**5.6%**	< 1e-3	192	**8.3%**	< 1e-3	228
25	**8.8%**	< 1e-3	108	**11.3%**	< 1e-3	144
36	**8.2%**	< 1e-3	72	**14.4%**	< 1e-3	72
49	**9.8%**	8.1e-3	24	**16.8%**	< 1e-3	24

S-Table 1: Mean pairwise difference of ACC between not averaged channels "Not Avg" and averaged channels "Avg". Positive mean Δ indicate that "Not Avg" outperformed "Avg". P-values are computed from the Wilcoxon signed rank test and the number of data points for each test is shown in the *n* column.

Fixed Channel Comparison

Given a fixed number of electrodes, is shrinking the distance between them beneficial? This is another way to compare grids of different densities. Again, we sub-sampled to create a set of virtual grids with 4, 9 and 16 channels and compared 400 vs 800µm, 400 vs 1200µm, and 800 vs 1200µm pitch (Fig 8). Each device type (eg. (2,1)) was ranked according to ACC for all placements and only the top two were used in this analysis. The top two ranked placements for the high-density device type (eg. (2.1)) are compared to the top two placements for the low-density device type (eg. (2,2)) in a pairwise fashion. Histograms of pairwise ACC differences are shown in Fig 8. In both subjects, we did not observe a significant difference for any comparison except once (Table 3). Unlike when controlling for area, negative mean differences were observed suggesting that higher density grids maybe disadvantageous when controlling for channel count. Negative mean differences were observed 1 out of 7 comparisons for SD007 and 4 out of 7 comparisons for SD008. These empirical results are consistent with our modeling results, which also found situations in which higher density grids underperformed when controlling for channel count.

It is important to note that for SD007, the fixed channel comparison were confounded by the percentage of good channels since high density grids tended to have more good channels in this analysis (Fig S8). Therefore, the fixed channel results can be interpreted as an overestimate of the high-density performance. Since high density did not significantly outperform lower density grids anyway, we reach the same conclusion even with the bias, which is that high density grids did not out perform lower density grids when controlling for channels.

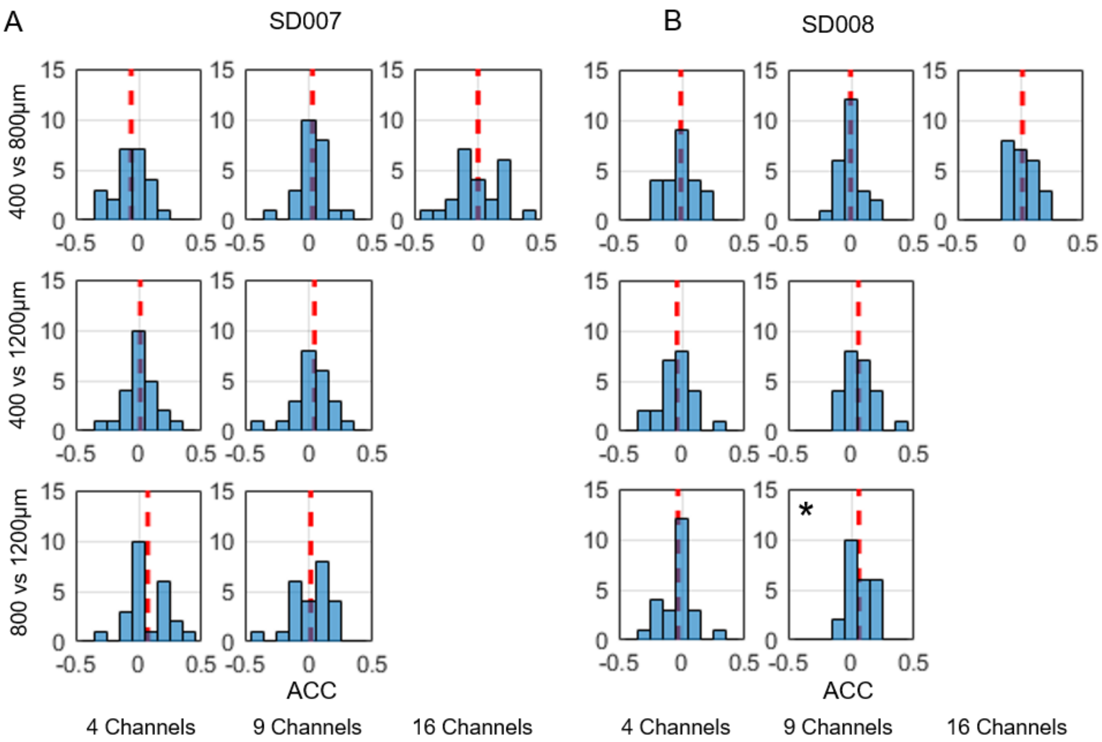

S-Figure 9: Is shrinking the distance between channels beneficial? (A) SD007 and (B) SD008 histograms comparing various device types of the same number of channels. The x-axis of the histogram is pairwise difference of accuracy between two devices types (eg. (2,1) and (2,2)). Each device type is ranked by ACC across possible placements and the top 2 were included in the analysis. The top 1 and 2 from each device type are then compared against each other. Distribution statistics are provided in Table 3. ACC sample vectors with significantly different mean ranks are denoted with a black asterisk (P < 0.01). The dashed red line indicates the mean of the pairwise differences.

S-Table 2: Is spreading out channels beneficial? Overall (fold + location) mean difference between paired accuracies, p-values from Wilcoxon signed-rank sum test (n = 24), and mean accuracy of the high-density grid. The mean difference of sample vectors which are significantly different from each other are denoted by **bold** (P < 0.01).

	SD007			SD008		
Comparison	Mean Δ	p-value	Mean HD	Mean HD	p-value	Mean HD
(2,1) – (2,2)	-5.9%	0.044	75.7%	-0.80%	0.73	89.7%
(3,1) – (3,2)	3.0%	0.17	82.0%	-0.38%	1.0	92.8%
(4,1) – (4,2)	0%	0.89	79.5%	1.6%	0.31	92.4%
(2,1) – (2,3)	1.3%	0.75	75.7%	-3.8%	0.099	89.7%
(3,1) – (3,3)	4.5%	0.22	82.0%	5.8%	0.011	92.8%
(2,2) – (2,3)	7.2%	0.039	81.6%	-3.0%	0.18	90.5%
(3,2) – (3,3)	1.6%	0.56	79.0%	**6.1%**	2.3e-3	93.1%

Percentage of Good Channels

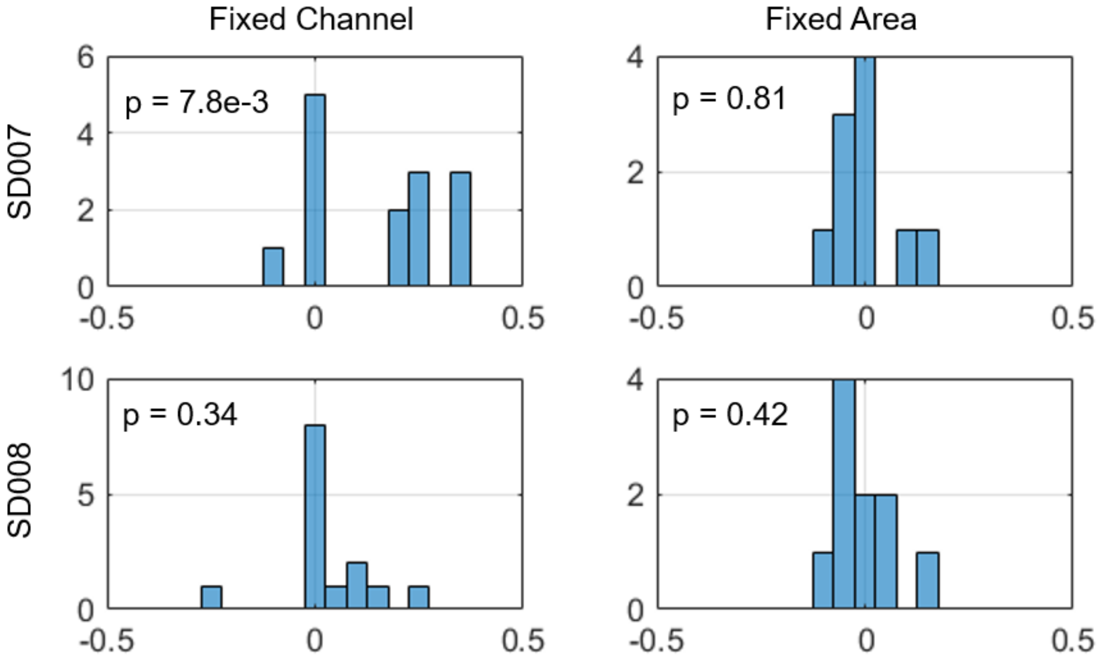

S-Figure 10: Histograms of difference in the fraction of good channels difference between high and low-density grids across 2 subjects (rows) and 2 comparison types (columns). If there a consistent bias of for particular subject and comparison type, the distribution while be shifted away from 0. To determine if, there was a significant shift from 0, the Wilcoxon signed rank test was performed and the p-values from the test are reported in the upper left-hand corner of each histogram. Only SD007, fixed channel comparison (upper left histogram) was significantly biased, which was noted in the Sub-sampling section of the Methods as well as Discussion.

References

Abidian, M.R., Corey, J.M., Kipke, D.R., Martin, D.C., 2010. Conducting-polymer nanotubes improve electrical properties, mechanical adhesion, neural attachment and neurite outgrowth of neural electrodes. Small 6, 421–429. doi:10.1002/smll.200901868

Abidian, M.R., Martin, D.C., 2009. Multifunctional nanobiomaterials for neural interfaces. Adv. Funct. Mater. 19, 573–585. doi:10.1002/adfm.200801473

Arneodo, E.M., Chen, S., Gilja, V., Gentner, T.Q., 2017. A neural decoder for learned vocal behavior. bioRxiv 193987. doi:10.1101/193987

Benezra, S.E., Narayanan, R.T., Egger, R., Oberlaender, M., Long, M.A., 2018. Morphological characterization of HVC projection neurons in the zebra finch (Taeniopygia guttata). J. Comp. Neurol. doi:10.1002/cne.24437

Benjamini, Y., Hochberg, Y., 1995. Controlling the false discovery rate: a practical and powerful approach to multiple testing. J. R. Stat. Soc. Ser. B 57, 289–300. doi:10.2307/2346101

Biran, R., Martin, D.C., Tresco, P.A., 2005. Neuronal cell loss accompanies the brain tissue response to chronically implanted silicon microelectrode arrays. Exp. Neurol. 195, 115–126.

Black, C., Voigts, J., Agrawal, U., Ladow, M., Santoyo, J., Moore, C., Jones, S., 2017. Open Ephys electroencephalography (Open Ephys + EEG): A modular, low-cost, open-source solution to human neural recording. J. Neural Eng. 14. doi:10.1088/1741-2552/aa651f

Bolhuis, J.J., Gahr, M., 2006. Neural mechanisms of birdsong memory. Nat. Rev. Neurosci. doi:10.1038/nrn1904

Brainard, M.S., Doupe, A.J., 2002. What songbirds teach us about learning. Nature. doi:10.1038/417351a

Breshears, J.D., Roland, J.L., Sharma, M., Gaona, C.M., Freudenburg, Z. V, Tempelhoff, R., Avidan, M.S., Leuthardt, E.C., 2010. Stable and dynamic cortical electrophysiology of induction and emergence with propofol anesthesia. Proc. Natl. Acad. Sci. U. S. A. 107, 21170–5. doi:10.1073/pnas.1011949107

Bundy, D.T., Zellmer, E., Gaona, C.M., Sharma, M., Szrama, N., Hacker, C., Freudenburg, Z. V, Daitch, A., Moran, D.W., Leuthardt, E.C., 2014. Characterization of the effects of the human dura on macro- and micro-electrocorticographic recordings. J. Neural Eng. 11, 016006. doi:10.1088/1741-2560/11/1/016006

Buzsáki, G., Anastassiou, C. a., Koch, C., 2012. The origin of extracellular fields and currents — EEG, ECoG, LFP and spikes. Nat. Rev. Neurosci. 13, 407–420. doi:10.1038/nrn3241

Chang, E.F., 2015. Towards Large-Scale, Human-Based, Mesoscopic Neurotechnologies. Neuron 86, 68–78. doi:10.1016/j.neuron.2015.03.037

Cogan, S.F., 2008. Neural stimulation and recording electrodes. Annu Rev Biomed Eng 10, 275–309. doi:10.1146/annurev.bioeng.10.061807.160518

Cogan, S.F., Ludwig, K.A., Welle, C.G., Takmakov, P., 2016. Tissue damage thresholds during therapeutic electrical stimulation. J. Neural Eng. 13. doi:10.1088/1741-2560/13/2/021001

Craven, D., McGinley, B., Kilmartin, L., Glavin, M., Jones, E., 2015. Compressed Sensing for Bioelectric Signals: A Review. IEEE J. Biomed. Heal. Informatics 19, 529–540. doi:10.1109/JBHI.2014.2327194

Crone, N.E., Boatman, D., Gordon, B., Hao, L., 2001. Induced electrocorticographic gamma activity during auditory perception. Clin. Neurophysiol. 112, 565–582. doi:10.1016/S1388-2457(00)00545-9

Crone, N.E., Miglioretti, D.L., Gordon, B., Lesser, R.P., Crone, N., 1998. Functional mapping of human sensorimotor cortex with electrocorticographic spectral analysis II. Event-related synchronization in the gamma band. Brain 121, 2301–2315. doi:10.1093/brain/121.12.2301

Crone, N.E., Miglioretti, D.L., Gordon, B., Sieracki, J.M., Wilson, M.T., Uematsu, S., Lesser, R.P., 1998. Functional mapping of human sensorimotor cortex with electrocorticographic spectral analysis. I. Alpha and beta event-related desynchronization. Brain 121 (Pt 1, 2271–99. doi:10.1093/brain/121.12.2271

Cui, X., Lee, V.A., Raphael, Y., Wiler, J.A., Hetke, J.F., Anderson, D.J., Martin, D.C., 2001. Surface modification of neural recording electrodes with conducting polymer/biomolecule blends. J. Biomed. Mater. Res. 56, 261–272. doi:10.1002/1097-4636(200108)56:2<261::AID-JBM1094>3.0.CO;2-I

Cunningham, J.M., 2017. An Investigation into Neural Tissue-Electrode Contact as a Performance Impairing Factor in Flexible, Micro-Electrocorticographic Probes Meant for Brain-Computer Interfacing. University of Alberta.

Darvas, F., Scherer, R., Ojemann, J.G., Rao, R.P., Miller, K.J., Sorensen, L.B., 2010. High gamma mapping using EEG. Neuroimage 49, 930–938. doi:10.1016/j.neuroimage.2009.08.041

Fee, M.S., Kozhevnikov, A.A., Hahnloser, R.H.R., 2004. Neural mechanisms of vocal sequence: Generation in the songbird. Ann. N. Y. Acad. Sci. 1016, 153–170. doi:10.1196/annals.1298.022

Flinker, A., Chang, E.F., Barbaro, N.M., Berger, M.S., Knight, R.T., 2011. Sub-centimeter language organization in the human temporal lobe. Brain Lang. 117, 103–109. doi:10.1016/j.bandl.2010.09.009

Flint, R.D., Rosenow, J.M., Tate, M.C., Slutzky, M.W., 2017. Continuous decoding of human grasp kinematics using epidural and subdural signals. J. Neural Eng. 14, 016005. doi:10.1088/1741-2560/14/1/016005

Freeman, W.J., Rogers, L.J., Holmes, M.D., Silbergeld, D.L., 2000. Spatial spectral analysis of human electrocorticograms including the alpha and gamma bands. J. Neurosci. Methods 95, 111–21. doi:10.1016/S0165-0270(99)00160-0

Ganguli, S., Sompolinsky, H., 2012. Compressed Sensing, Sparsity, and Dimensionality in Neuronal Information Processing and Data Analysis. Rev. Adv. 35, 485–508. doi:10.1146/annurev-neuro-062111

Ganji, M., Elthakeb, A.T., Tanaka, A., Gilja, V., Halgren, E., Dayeh, S.A., 2017a. Scaling Effects on the Electrochemical Performance of poly(3,4-ethylenedioxythiophene (PEDOT), Au, and Pt for Electrocorticography Recording. Adv. Funct. Mater. 27, 1703018. doi:10.1002/adfm.201703018

Ganji, M., Kaestner, E., Hermiz, J., Rogers, N., Tanaka, A., Cleary, D., Lee, S.H., Snider, J., Halgren, M., Cosgrove, G.R., Carter, B.S., Barba, D., Uguz, I., Malliaras, G.G., Cash, S.S., Gilja, V., Halgren, E., Dayeh, S.A., 2017b. Development and Translation of PEDOT:PSS Microelectrodes for Intraoperative Monitoring. Adv. Funct. Mater. 1700232. doi:10.1002/adfm.201700232

George, I., Cousillas, H., Richard, J.P., Hausberger, M., 2005. Auditory responses in the HVC of anesthetized starlings. Brain Res. 1047, 245–260. doi:10.1016/j.brainres.2005.04.047

Ghomashchi, A., Zheng, Z., Majaj, N., Trumpis, M., Kiorpes, L., Viventi, J., 2014. A low-cost, open-source, wireless electrophysiology system, in: 2014 36th Annual International Conference of the IEEE Engineering in Medicine and Biology Society, EMBC 2014. pp. 3138–41. doi:10.1109/EMBC.2014.6944288

Gilja, V., Nuyujukian, P., Chestek, C.A., Cunningham, J.P., Yu, B.M., Fan, J.M., Churchland, M.M., Kaufman, M.T., Kao, J.C., Ryu, S.I., Shenoy, K. V., 2012. A high-performance neural prosthesis enabled by control algorithm design. Nat. Neurosci. 15, 1752–1757. doi:10.1038/nn.3265

Gilja, V., Pandarinath, C., Blabe, C.H., Nuyujukian, P., Simeral, J.D., Sarma, A.A., Sorice, B.L., Perge, J.A., Jarosiewicz, B., Hochberg, L.R., Shenoy, K. V., Henderson, J.M., 2015. Clinical translation of a high-performance neural prosthesis. Nat. Med. 21, 1142–1145. doi:10.1038/nm.3953

Green, R.A., Hassarati, R.T., Goding, J.A., Baek, S., Lovell, N.H., Martens, P.J., Poole-Warren, L.A., 2012. Conductive Hydrogels: Mechanically Robust Hybrids for Use as Biomaterials. Macromol. Biosci. 12, 494–501. doi:10.1002/mabi.201100490

Green, R.A., Lovell, N.H., Wallace, G.G., Poole-Warren, L.A., 2008. Conducting polymers for neural interfaces: Challenges in developing an effective long-term implant. Biomaterials 29, 3393–3399. doi:10.1016/j.biomaterials.2008.04.047

Hahnloser, R.H.R., Kozhevnikov, A.A., Fee, M.S., 2002. An ultra-sparse code underlies the generation of neural sequences in a songbird. Nature 419, 65–70. doi:10.1038/nature00974

Hatsopoulos, N.G., Donoghue, J.P., 2009. The Science of Neural Interface Systems. Annu. Rev. Neurosci. 32, 249–266. doi:10.1146/annurev.neuro.051508.135241

Heim, M., Yvert, B., Kuhn, A., 2012. Nanostructuration strategies to enhance microelectrode array (MEA) performance for neuronal recording and stimulation. J. Physiol. Paris 106, 137–145. doi:10.1016/j.jphysparis.2011.10.001

Herculano-Houzel, S., 2009. The human brain in numbers: a linearly scaled-up primate brain. Front. Hum. Neurosci. 3. doi:10.3389/neuro.09.031.2009

Herff, C., Heger, D., de Pesters, A., Telaar, D., Brunner, P., Schalk, G., Schultz, T., 2015. Brain-to-text: Decoding spoken phrases from phone representations in the brain. Front. Neurosci. doi:10.3389/fnins.2015.00217

Hermiz, J., Rogers, N., Kaestner, E., Ganji, M., Cleary, D., Snider, J., Barba, D., Dayeh, S., Halgren, E., Gilja, V., 2016. A clinic compatible , open source electrophysiology system. Eng. Med. Biol. Soc. (EMBC), 2016 IEEE 38th Annu. Int. Conf. 2016–Octob, 4511–4514. doi:10.1109/EMBC.2016.7591730

Hill, M., Rios, E., Sudhakar, S.K., Roossien, D.H., Caldwell, C., Cai, D., Ahmed, O.J., Viventi, J., Lempka, S.F., Chestek, C.A., 2018. Quantitative simulation of extracellular single unit recording from the surface of cortex, in: Neural Interface Conference.

Hoggan, E., Brewster, S.A., Johnston, J., 2008. Investigating the effectiveness of tactile feedback for mobile touchscreens, in: Proceeding of the Twenty-Sixth Annual CHI Conference on Human Factors in Computing Systems - CHI '08. ACM Press, New York, New York, USA, p. 1573. doi:10.1145/1357054.1357300

Horton, J.C., Adams, D.L., 2005. The cortical column: a structure without a function. Philos. Trans. R. Soc. B Biol. Sci. 360, 837–862. doi:10.1098/rstb.2005.1623

Huupponen, E., Maksimow, A., Lapinlampi, P., Särkelä, M., Saastamoinen, A., Snapir, A., Scheinin, H., Scheinin, M., Meriläinen, P., Himanen, S.L., Jääskeläinen, S., 2008. Electroencephalogram spindle activity during dexmedetomidine sedation and physiological sleep. Acta Anaesthesiol. Scand. 52, 289–294. doi:10.1111/j.1399-6576.2007.01537.x

Insanally, M., Trumpis, M., Wang, C., Chiang, C.-H., Woods, V., Palopoli-Trojani, K., Bossi, S., Froemke, R.C., Viventi, J., 2016. A low-cost, multiplexed μECoG system for high-density recordings in freely moving rodents. J. Neural Eng. 13, 026030. doi:10.1088/1741-2560/13/2/026030

Jiang, W., Pailla, T., Dichter, B., Chang, E.F., Gilja, V., 2016. Decoding speech using the timing of neural signal modulation, in: Engineering in Medicine and Biology Society (EMBC), 2016 IEEE 38th Annual International Conference of The. pp. 1532–1535.

Jorfi, M., Skousen, J.L., Weder, C., Capadona, J.R., 2014. Progress towards biocompatible intracortical microelectrodes for neural interfacing applications. J. Neural Eng. 12, 11001.

Jun, J.J., Steinmetz, N.A., Siegle, J.H., Denman, D.J., Bauza, M., Barbarits, B., Lee, A.K., Anastassiou, C.A., Andrei, A., Aydin, Ç., Barbic, M., Blanche, T.J., Bonin, V., Couto, J., Dutta, B., Gratiy, S.L., Gutnisky, D.A., Häusser, M., Karsh, B., Ledochowitsch, P., Lopez, C.M., Mitelut, C., Musa, S., Okun, M., Pachitariu, M., Putzeys, J., Rich, P.D., Rossant, C., Sun, W.L., Svoboda, K., Carandini, M., Harris, K.D., Koch, C., O'Keefe, J., Harris, T.D., 2017. Fully integrated silicon probes for high-density recording of neural activity. Nature 551, 232–236. doi:10.1038/nature24636

Kaiju, T., Doi, K., Yokota, M., Watanabe, K., Inoue, M., Ando, H., Takahashi, K., Yoshida, F., Hirata, M., Suzuki, T., 2017. High Spatiotemporal Resolution ECoG Recording of Somatosensory Evoked Potentials with Flexible Micro-Electrode Arrays. Front. Neural Circuits 11, 20. doi:10.3389/fncir.2017.00020

Kao, J.C., Nuyujukian, P., Ryu, S.I., Shenoy, K. V., 2017. A High-Performance Neural Prosthesis Incorporating Discrete State Selection with Hidden Markov Models. IEEE Trans. Biomed. Eng. 64, 935–945. doi:10.1109/TBME.2016.2582691

Kellis, S., Miller, K., Thomson, K., Brown, R., House, P., Greger, B., 2010. Decoding spoken words using local field potentials recorded from the cortical surface. J. Neural Eng. 7, 56007.

Kellis, S., Sorensen, L., Darvas, F., Sayres, C., Neill, K.O., Brown, R.B., House, P., Ojemann, J., Greger, B., 2016. Clinical Neurophysiology Multi-scale analysis of neural activity in humans : Implications for micro-scale electrocorticography. Clin. Neurophysiol. 127, 591–601. doi:10.1016/j.clinph.2015.06.002

Khodagholy, D., Doublet, T., Gurfinkel, M., Quilichini, P., Ismailova, E., Leleux, P., Herve, T., Sanaur, S., Bernard, C., Malliaras, G.G., 2011. Highly conformable conducting polymer electrodes for in vivo recordings. Adv. Healthc. Mater. 23, 268–272. doi:10.1002/adma.201102378

Khodagholy, D., Gelinas, J.N., Thesen, T., Doyle, W., Devinsky, O., Malliaras, G.G., Buzsáki, G., 2014. NeuroGrid : recording action potentials from the surface of the brain. Nat. Neurosci. doi:10.1038/nn.3905

Khodagholy, D., Gelinas, J.N., Zhao, Z., Yeh, M., Long, M., Greenlee, J.D., Doyle, W., Devinsky, O., Buzsáki, G., 2016. Organic electronics for high-resolution electrocorticography of the human brain. Sci. Adv. 1–9.

Kim, J.H., Kang, G., Nam, Y., Choi, Y.K., 2010. Surface-modified microelectrode array with flake nanostructure for neural recording and stimulation. Nanotechnology 21. doi:10.1088/0957-4484/21/8/085303

Kinney, J.P., Bernstein, J.G., Meyer, A.J., Barber, J.B., Bolivar, M., Newbold, B., Scholvin, J., Moore-Kochlacs, C., Wentz, C.T., Kopell, N.J., Boyden, E.S., 2015. A direct-to-drive neural data acquisition system. Front. Neural Circuits 9, 1–8. doi:10.3389/fncir.2015.00046

Kofke, W.A., Tempelhoff, R., Dasheiff, R.M., 1997. Anesthetic implications of epilepsy, status epilepticus, and epilepsy surgery. J. Neurosurg. Anesthesiol. 9, 349–372. doi:10.1097/00008506-199710000-00011

Ledochowitsch, P., Koralek, A.C., Moses, D., Carmena, J.M., Maharbiz, M.M., 2013. Sub-mm functional decoupling of electrocortical signals through closed-loop BMI learning. Conf. Proc. ... Annu. Int. Conf. IEEE Eng. Med. Biol. Soc. IEEE Eng. Med. Biol. Soc. Annu. Conf. 2013, 5622–5. doi:10.1109/EMBC.2013.6610825

Leuthardt, E.C., Gaona, C., Sharma, M., Szrama, N., Roland, J., Freudenberg, Z., Solis, J., Breshears, J., Schalk, G., 2011. Using the electrocorticographic speech network to control a brain--computer interface in humans. J. Neural Eng. 8, 36004.

Ludwig, K.A., Miriani, R.M., Langhals, N.B., Joseph, M.D., Anderson, D.J., Kipke, D.R., 2009. Using a Common Average Reference to Improve Cortical Neuron Recordings From Microelectrode Arrays. J. Neurophysiol. 101, 1679–1689. doi:10.1152/jn.90989.2008

MacKenzie, I.S., Lopez, M.H., Castelluci, S., 2009. Text entry with the Apple iPhone and the Nintendo Wii. Proc. CHI2009.

Manolakis, D.G., Ingle, V.K., Kogon, S.M., 2000. Statistical and adaptive signal processing: spectral estimation, signal modeling, adaptive filtering, and array processing. McGraw-Hill Boston.

Martin, S., Brunner, P., Holdgraf, C., Heinze, H.-J., Crone, N.E., Rieger, J., Schalk, G., Knight, R.T., Pasley, B.N., 2014. Decoding spectrotemporal features of overt and covert speech from the human cortex. Front. Neuroeng. 7, 14.

Merrill, D.R., Bikson, M., Jefferys, J.G.R., 2005. Electrical stimulation of excitable tissue: Design of efficacious and safe protocols. J. Neurosci. Methods. doi:10.1016/j.jneumeth.2004.10.020

Miller, K.J., Leuthardt, E.C., Schalk, G., Rao, R.P.N., Anderson, N.R., Moran, D.W., Miller, J.W., Ojemann, J.G., 2007. Spectral Changes in Cortical Surface Potentials during Motor Movement. J. Neurosci. 27, 2424–2432. doi:10.1523/JNEUROSCI.3886-06.2007

Mitra, P., Bokil, H., 2009. Observed Brain Dynamics, Observed Brain Dynamics. doi:10.1093/acprof:oso/9780195178081.001.0001

Mugler, E.M., Patton, J.L., Flint, R.D., Wright, Z.A., Schuele, S.U., Rosenow, J., Shih, J.J., Krusienski, D.J., Slutzky, M.W., 2014. Direct classification of all American English phonemes using signals from functional speech motor cortex. J. Neural Eng. 11. doi:10.1088/1741-2560/11/3/035015

Muller, L., Chavane, F., Reynolds, J., Sejnowski, T.J., 2018. Cortical travelling waves: mechanisms and computational principles. Nat. Rev. Neurosci.

Muller, L., Felix, S., Shah, K.G., Lee, K., Pannu, S., Chang, E.F., 2016a. Thin-film , high-density micro-electrocorticographic decoding of a human cortical gyrus. Eng. Med. Biol. Soc. (EMBC), 2016 IEEE 38th Annu. Int. Conf. 1528–1531. doi:10.1109/EMBC.2016.7591001

Muller, L., Hamilton, L.S., Edwards, E., Bouchard, K.E., Chang, E.F., 2016b. Spatial resolution dependence on spectral frequency in human speech cortex electrocorticography. J. Neural Eng. 13, 056013. doi:10.1088/1741-2560/13/5/056013

Muller, L., Piantoni, G., Koller, D., Cash, S.S., Halgren, E., Sejnowski, T.J., 2016. Rotating waves during human sleep spindles organize global patterns of activity that repeat precisely through the night. Elife 5.

Newman, J.P., Zeller-Townson, R., Fong, M.-F., Arcot Desai, S., Gross, R.E., Potter, S.M., 2012. Closed-Loop, Multichannel Experimentation Using the Open-Source NeuroRighter Electrophysiology Platform. Front. Neural Circuits 6, 98. doi:10.3389/fncir.2012.00098

Nottebohm, F., 2005. The neural basis of birdsong. PLoS Biol. doi:10.1371/journal.pbio.0030164

OpenBCI, 2013. OpenBCI [WWW Document]. OpenBCI. URL http://openbci.com/

Pachitariu, M., Steinmetz, N., Kadir, S., Carandini, M., Harris, K., 2016. Fast and accurate spike sorting of high-channel count probes with KiloSort 1–9.

Pailla, T., Jiang, W., Dichter, B., Chang, E.F., Gilja, V., 2016. ECoG data analyses to inform closed-loop BCI experiments for speech-based prosthetic applications, in: Engineering in Medicine and Biology Society (EMBC), 2016 IEEE 38th Annual International Conference of The. pp. 5713–5716.

Pandarinath, C., Nuyujukian, P., Blabe, C.H., Sorice, B.L., Saab, J., Willett, F.R., Hochberg, L.R.L., Shenoy, K.V.K., Henderson, J.J.M., Ashmore, R., Kelly, J., Boninger, M., Ramsey, N., Henderson, J.J.M., Shenoy, K.V.K., Donoghue, J., Hochberg, L.R.L., 2017. High performance communication by people with paralysis using an intracortical brain-computer interface. Elife 6, 326–333. doi:10.7554/eLife.18554

Park, S., Song, Y.J., Han, J.H., Boo, H., Chung, T.D., 2010. Structural and electrochemical features of 3D nanoporous platinum electrodes. Electrochim. Acta 55, 2029–2035. doi:10.1016/j.electacta.2009.11.026

Pasley, B.N., David, S. V, Mesgarani, N., Flinker, A., Shamma, S.A., Crone, N.E., Knight, R.T., Chang, E.F., 2012. Reconstructing speech from human auditory cortex. PLoS Biol. 10, e1001251.

Pei, X., Barbour, D.L., Leuthardt, E.C., Schalk, G., 2011. Decoding vowels and consonants in spoken and imagined words using electrocorticographic signals in humans. J. Neural Eng. 8, 46028.

Polikov, V.S., Tresco, P.A., Reichert, W.M., 2005. Response of brain tissue to chronically implanted neural electrodes. J. Neurosci. Methods 148, 1–18.

Polikov, V.S., Tresco, P.A., Reichert, W.M., 2005. Response of brain tissue to chronically implanted neural electrodes. J. Neurosci. Methods. doi:10.1016/j.jneumeth.2005.08.015

Qian, J., Hastie, T., Friedman, J., Tibshirani, R., Simon, N., 2013. Glmnet for Matlab, 2013. URL http//www. stanford. edu/~ Hast.

Ray, S., Crone, N.E., Niebur, E., Franaszczuk, P.J., Hsiao, S.S., 2008. Neural correlates of high-gamma oscillations (60-200 Hz) in macaque local field potentials and their potential implications in electrocorticography. J. Neurosci. 28, 11526–36. doi:10.1523/JNEUROSCI.2848-08.2008

Ray, S., Crone, N.E., Niebur, E., Franaszczuk, P.J., Hsiao, S.S., 2008. Neural Correlates of High-Gamma Oscillations (60-200 Hz) in Macaque Local Field Potentials and Their Potential Implications in Electrocorticography. J. Neurosci. 28, 11526–11536. doi:10.1523/JNEUROSCI.2848-08.2008

Rivnay, J., Inal, S., Collins, B.A., Sessolo, M., Stavrinidou, E., Strakosas, X., Tassone, C., Delongchamp, D.M., Malliaras, G.G., 2016. Structural control of mixed ionic and electronic transport in conducting polymers. Nat. Commun. 7. doi:10.1038/ncomms11287

Rivnay, J., Wang, H., Fenno, L., Deisseroth, K., Malliaras, G.G., 2017. Next-generation probes, particles, and proteins for neural interfacing. Sci. Adv. 3, e1601649.

Rockland, 2010. Five points on columns. Front. Neuroanat. doi:10.3389/fnana.2010.00022

Rousche, P.J., Normann, R.A., 1992. A method for pneumatically inserting an array of penetrating electrodes into cortical tissue. Ann. Biomed. Eng. 20, 413–422. doi:10.1007/BF02368133

San-juan, D., Chiappa, K.H., Cole, A.J., 2010. Propofol and the electroencephalogram. Clin. Neurophysiol. 121, 998–1006. doi:10.1016/j.clinph.2009.12.016

Schlenoff, J.B., Xu, H., 1992. Evolution of physical and electrochemical properties of polypyrrole during extended oxidation. J. Electrochem. Soc. 139, 2397–2401.

Schmidt, M.F., Konishi, M., 1998. Gating of auditory responses in the vocal control system of awake songbirds. Nat. Neurosci. 1, 513–518. doi:10.1038/2232

Siegle, J.H., Hale, G.J., Newman, J.P., Voigts, J., 2015. Neural ensemble communities: Open-source approaches to hardware for large-scale electrophysiology, Current Opinion in Neurobiology. Elsevier Current Trends. doi:10.1016/j.conb.2014.11.004

Siegle, J.H., López, A.C., Patel, Y.A., Abramov, K., Ohayon, S., Voigts, J., 2017. Open Ephys: An open-source, plugin-based platform for multichannel electrophysiology. J. Neural Eng. 14. doi:10.1088/1741-2552/aa5eea

Slutzky, M.W., Jordan, L.R., Krieg, T., Chen, M., Mogul, D.J., Miller, L.E., 2010. Optimal spacing of surface electrode arrays for brain-machine interface applications. J. Neural Eng. 7, 26004. doi:10.1088/1741-2560/7/2/026004

Song, Y., Viventi, J., Wang, Y., 2017a. Multi Resolution LSTM For Long Term Prediction In Neural Activity Video. arXiv Prepr. arXiv1705.02893.

Song, Y., Wang, Y., Viventi, J., 2017b. Unsupervised Learning of Spike Patterns for Seizure Detection and Wavefront Estimation of High Resolution Micro Electrocorticographic ($$\$mu $ ECoG) Data. IEEE Trans. Nanobioscience 16, 418–427.

Souza, P., Rosen, S., 2009. Effects of envelope bandwidth on the intelligibility of sine- and noise-vocoded speech. J. Acoust. Soc. Am. 126, 792–805. doi:10.1121/1.3158835

Stevenson, I.H., Kording, K.P., 2011. How advances in neural recording affect data analysis, in: Nature Neuroscience. pp. 139–142. doi:10.1038/nn.2731

Stringer, C., Pachitariu, M., Steinmetz, N., Reddy, C.B., Carandini, M., Harris, K.D., 2018. Spontaneous behaviors drive multidimensional, brain-wide population activity. bioRxiv 306019. doi:10.1101/306019

Travis, K.E., Leonard, M.K., Chan, A.M., Torres, C., Sizemore, M.L., Qu, Z., Eskandar, E., Dale, A.M., Elman, J.L., Cash, S.S., Halgren, E., 2013. Independence of early speech processing from word meaning. Cereb. Cortex 23, 2370–2379. doi:10.1093/cercor/bhs228

Trumpis, M., Insanally, M., Zou, J., ElSharif, A., Ghomashchi, A., Artan, N.S., Froemke, R., Viventi, J., 2017a. A low-cost, scalable, current-sensing digital headstage for high channel count µECoG. J. Neural Eng. doi:10.1088/1741-2552/aa5a82

Trumpis, M., Insanally, M., Zou, J., Elsharif, A., Ghomashchi, A., Sertac Artan, N., Froemke, R.C., Viventi, J., 2017b. A low-cost, scalable, current-sensing digital headstage for high channel count μeCoG. J. Neural Eng. 14. doi:10.1088/1741-2552/aa5a82

Uguz, I., Ganji, M., Hama, A., Tanaka, A., Inal, S., Youssef, A., Owens, R.M., Quilichini, P.P., Ghestem, A., Bernard, C., Dayeh, S.A., Malliaras, G.G., 2016. Autoclave Sterilization of PEDOT:PSS Electrophysiology Devices. Adv. Healthc. Mater. 1–5. doi:10.1002/adhm.201600870

Vetter, R.J., Williams, J.C., Hetke, J.F., Nunamaker, E.A., Kipke, D.R., 2004. Chronic neural recording using silicon-substrate microelectrode arrays implanted in cerebral cortex. IEEE Trans. Biomed. Eng. 51, 896–904. doi:10.1109/TBME.2004.826680

Viventi, J., Kim, D.-H., Vigeland, L., Frechette, E.S., Blanco, J.A., Kim, Y.-S., Avrin, A.E., Tiruvadi, V.R., Hwang, S.-W., Vanleer, A.C., Wulsin, D.F., Davis, K., Gelber, C.E., Palmer, L., Van der Spiegel, J., Wu, J., Xiao, J., Huang, Y., Contreras, D., Rogers, J.A., Litt, B., 2011. Flexible, foldable, actively multiplexed, high-density electrode array for mapping brain activity in vivo. Nat. Neurosci. 14, 1599–605. doi:10.1038/nn.2973

Vodovotz, Y., Chow, C.C., Bartels, J., Lagoa, C., Prince, J.M., Levy, R.M., Kumar, R., Day, J., Rubin, J., Constantine, G., Billiar, T.R., Fink, M.P., Clermont, G., 2006. In silico models of acute inflammation in animals. Shock. doi:10.1097/01.shk.0000225413.13866.fo

Vu, E.T., Mazurek, M.E., Kuo, Y.C., 1994. Identification of a forebrain motor programming network for the learned song of zebra finches. J. Neurosci. 14, 6924–34. doi:10.1523/JNEUROSCI.14-11-06924.1994

Wang, P.T., King, C.E., McCrimmon, C.M., Lin, J.J., Sazgar, M., Hsu, F.P.K., Shaw, S.J., Millet, D.E., Chui, L.A., Liu, C.Y., Do, A.H., Nenadic, Z., 2016. Comparison of decoding resolution of standard and high-density electrocorticogram electrodes. J. Neural Eng. 13, 026016. doi:10.1088/1741-2560/13/2/026016

Woods, V., Wang, C., Bossi, S., Insanally, M., Trumpis, M., Froemke, R., Viventi, J., 2015. A low-cost, 61-channel uECoG array for use in rodents. Int. IEEE/EMBS Conf. Neural Eng. NER 2015–July, 573–576. doi:10.1109/NER.2015.7146687

Wyler, A.R., Richey, E.T., Atkinson, R.A., Hermann, B.P., 1987. Methohexital Activation of Epileptogenic Foci During Acute Electrocorticography. Epilepsia 28, 490–494. doi:10.1111/j.1528-1157.1987.tb03677.x

Yu, A.C., Margoliash, D., 1996. Temporal hierarchical control of singing in birds. Science. doi:10.1126/science.273.5283.1871

Yuste, R., Goering, S., Agüeray Arcas, B., Bi, G., Carmena, J.M., Carter, A., Fins, J.J., Friesen, P., Gallant, J., Huggins, J.E., Illes, J., Kellmeyer, P., Klein, E., Marblestone, A., Mitchell, C., Parens, E., Pham, M., Rubel, A., Sadato, N., Sullivan, L.S., Teicher, M., Wasserman, D., Wexler, A., Whittaker, M., Wolpaw, J., 2017. Four ethical priorities for neurotechnologies and AI. Nature. doi:10.1038/551159a

Zou, H., Hastie, T., 2005. Regularization and variable selection via the elastic net. J. R. Stat. Soc. Ser. B Stat. Methodol. 67, 301–320. doi:10.1111/j.1467-9868.2005.00503.x